For obtaining the degree of Master of Science in:
Engineering Wind Energy at Technical University of Denmark
Aerospace Engineering at Delft University of Technology

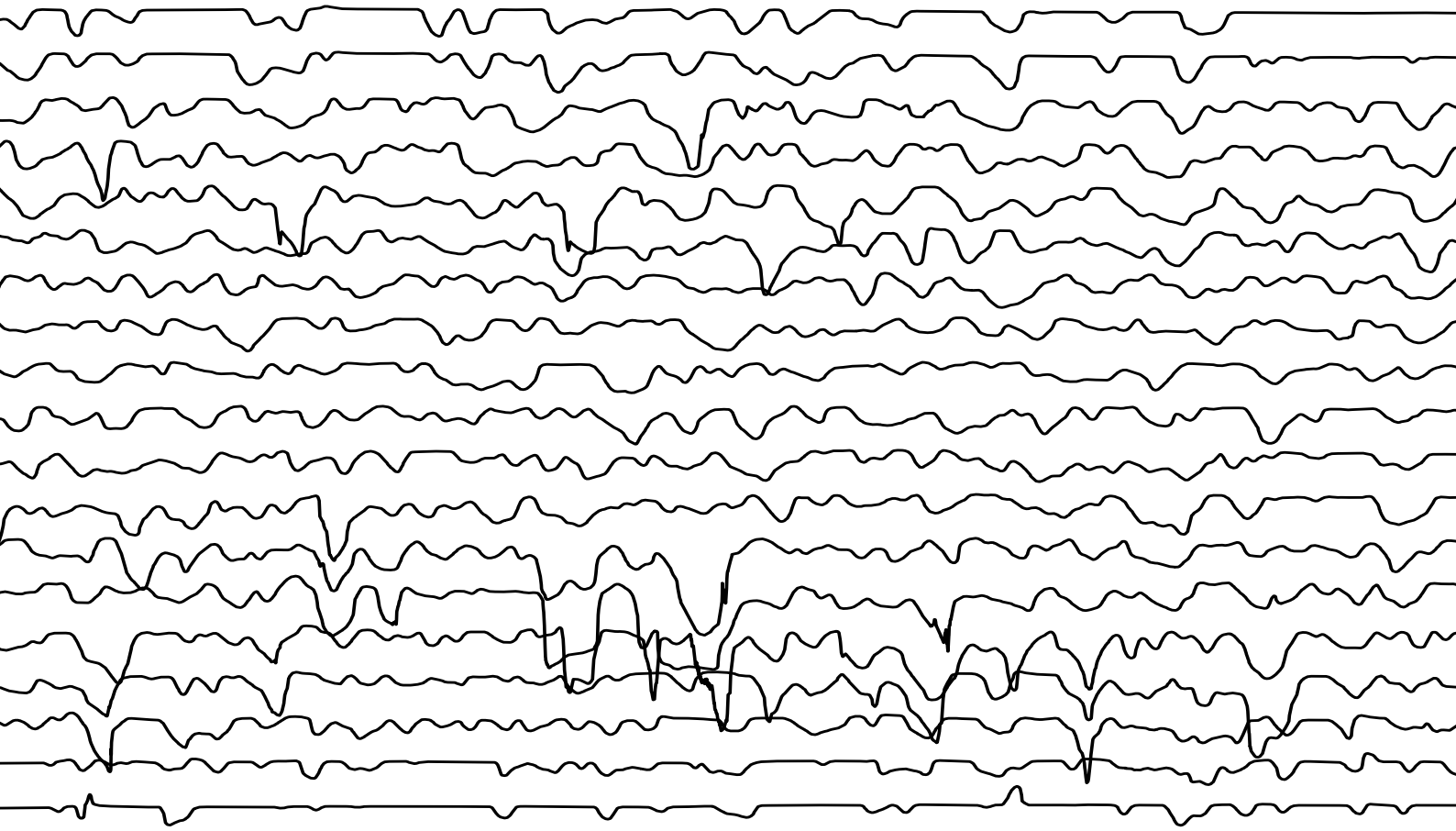

DTU Wind Energy
Department of Wind Energy

Deterioration in aerodynamic performance due to leading edge rain erosion

Marijn Leendert Willy Veraart

Lunderskov 2017

TU Delft DTU LM WIND POWER
a GE Renewable Energy business

LM Wind Power
Aero Group

Vingen 1
6640 Lunderskov, Denmark
Phone +45 7984 0000
info@lmwindpower.com
www.lmwindpower.com

Wind Energy Research Group
Faculty of Aerospace Engineering
Delft University of Technology

Kluyverweg 1
2629HS Delft, The Netherlands
Phone +31 1527 85170
windenergy-ae@tudelft.nl
www.windenergy.lr.tudelft.nl

DTU Wind Energy
Department of Wind Energy
Technical University of Denmark

Frederiksborgvej 399
Building
4000 Roskilde, Denmark
Phone +45 4677 5085
www.vindenergi.dtu.dk

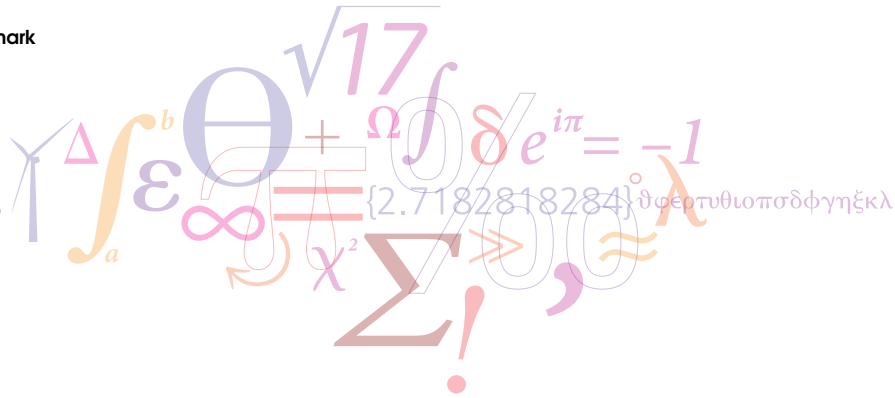

Summary

The purpose of this thesis is to determine the aerodynamic performance loss in terms of lift and drag due to leading edge rain erosion. This research is extremely relevant given the increased importance of erosion effects when considering the current trend of up-scaling (offshore) wind turbines and the lack of a scientific erosion modelling method to experimentally test these erosion effects. For this study, Rain Erosion Test specimens, which resemble realistic erosion patterns, were used. The modelling of erosion patterns was based upon these Rain Erosion Test specimens, as well as a validation between the modelled patterns and the RET specimens. Three different models were investigated, namely a standardized roughness model with zigzag tapes, a quick erosion model with hand tooled erosion patterns and a detachable leading edge erosion model with three dimensional printed leading edges incorporating different erosion patterns. This report is composed of seven chapters, each of them dealing with different aspects of measuring aerodynamic performance, characterizing erosion patterns and modelling the erosion surfaces.

Chapter 1 is introductory and is subdivided into three main sections. At first, a review is provided on previous erosion studies, noting that in these previous studies erosion was modelled inaccurately and was mostly focused on heavy erosion levels. This lead to the purpose and objectives of this study, which are to; charactere erosion at an early stage using Rain Erosion Test specimens, model characterized erosion levels and apply these to the leading edge of an airfoil, investigate the aerodynamic performance loss and compare the performance of different models to standardized roughness configuration (zigzag tapes). A selection of the erosion models is included, leading to the following models: standardized roughness (zigzag model), quick erosion model (hand tooling of surface) and finally the detachable leading edge model (three dimensional printed leading edges).

Chapter 2 describes how aerodynamic performance was measured, in terms of lift, drag and transition location. At first the infrared thermography method is described, which established the transition location. Secondly when using pressure taps, the lift coefficient can be computed. By means of the wake rake, the drag coefficient is computed. Also lift and drag measurement are possible by using the load cells, in case no pressure taps can be used in the airfoil model. An investigation of a boundary layer rake is included, showing that there was no possibility for boundary layer measurements using current measurement tools, due to a low resolution of pressure tubes of the boundary layer rake close to the surface.

In Chapter 3, different erosion patterns are identified and characterized, based upon three-dimensional scans of Rain Erosion Test specimens. At first the establishment of erosion patterns is clarified, by means of the Rain Erosion Test facility. Secondly three erosion phases were identified, as based upon the mass loss curve. When observing material mass loss versus the amount of rain droplets impacting the surface, initially only coating material is removed from the surface leading to a linear mass loss curve. As soon as the erosion perturbs into the glass lay-up, both coating, resin and glass materials chip off from the surface. The removal of different materials leads to a random mass loss. Rain Erosion Test specimens were selected at early erosion phases, where the erosion is still located within the linear mass loss curve. These patterns were three dimensionally scanned, enabling a thorough statistical analysis to be performed for each of the selected erosion phases. This statistical analysis considers two dimension roughness curves (extracted from three dimension surface maps), where in each valley a Gaussian function was fitted. Therefore a two dimensional roughness curve consist of a certain amount of valleys, each having a certain depths and widths, as well as a certain distances in between valleys. The valley depth, distance and with parameters are assumed to be the main statistical parameters describing

certain erosion levels. In addition, a method is proposed describing how erosion coverage, based upon impact angles of rain droplets as seen on the Rain Erosion Test specimens, can be scaled to a leading edge surface.

Chapter 4 discusses the standardized roughness configurations which utilize zigzag tapes, as well as the resulting aerodynamic performance losses for the different configurations. No performance losses were observed when zigzag tapes were applied at the stagnation point. Placing zigzag tapes towards pressure side also had no significant effect to the performance. Placing zigzag tapes towards suction side led to abrupt aerodynamic performance losses. Within the coverage investigated, locating zigzag tape furthest up to suction side led to highest performance losses.

The quick erosion model is described in Chapter 5. Erosion was applied initiating at the stagnation point with increasing coverage towards suction side. Three different erosion levels were tested, light erosion (1) was established by hammering a steel brush and medium (2) and heavy (3) erosion were established by hammering an aluminium Rain Erosion Test specimen into the leading edge surface. The resulting patterns for medium and heavy erosion were three dimensionally scanned, leading to a validation of the created erosion patterns to the RET erosion specimens. This showed that reached depths of the erosion patterns were in the same range as the Rain Erosion Test erosion. The aerodynamic performance losses were computed using the wind tunnel. This confirmed that erosion applied at the stagnation point had no influence on aerodynamic performance, whereas coverage applied towards suction side leads to increasing performance losses. For light and medium quick erosion patterns, more gradual performance losses were observed than for the zigzag model. Also for the quick model a method is described how the established erosion data can be incorporated in a BEM calculation, leading to an estimation for AEP loss due to erosion.

Chapter 6 investigates is the third and final model: the detachable leading edge model. This includes the design of the detachable airfoil model itself, a description of the modelling of the erosion patterns and how these modelled erosion patterns can be applied to a leading edge surface. The modelling of the erosion patterns was based upon creating three dimensional Gaussian functions (valleys) at certain coordinates, where each valley has a certain depth, width and distance. Therefore the modelling of the erosion patterns was directly based upon the three main statistical parameters as found for the Rain Erosion Test specimens. The erosion coverage was defined from the Rain Erosion Test coverage study, leading to an erosion coverage located almost directly at the leading edge (only slightly shifted towards pressure side). Furthermore, a validation was performed comparing the modelled erosion patterns to the RET erosion specimens, showing that the statistical parameters compare well to the Rain Erosion Test erosion. Finally lift and drag was measured and the aerodynamic performance results were computed. Based on these results, it became clear that even for light erosion, at the beginning of the linear mass loss curve, performance losses occur. However, increasing the erosion level from medium to heavy, did not result in an additional performance loss. Therefore it was concluded that for the same erosion coverage, from a certain erosion depth the performance loss remains constant. Only increasing the coverage would lead to an additional performance loss.

Final discussions and conclusions of the three models are included in Chapter 7. In this section, the quick and the detachable leading edge model are compared to the zigzag model, both in terms of modelling methods and resulting aerodynamic performance losses. With this study it is proven that an erosion modelling method is possible based upon realistic Rain Erosion Test specimens, leading to accurate aerodynamic performance measurements.

Preface

This MSc thesis was prepared at the Aerodynamics Group at LM Wind Power, the department of Wind Energy at the Technical University of Denmark and the faculty of Aerospace Engineering at Delft University of Technology, in fulfilment of the requirements for acquiring a Masters degree in Engineering from DTU and a Masters degree in Aerospace Engineering from TU Delft.

Thesis committee

Delft University of Technology
Prof.dr. Damiano Casalino
Prof.dr. Gerard van Bussel
Dr.ir. Nando Timmer
Dr.ir. Bas van Oudheusden
Dr.ir. Mac Gaunaa

Technical University of Denmark
Dr.ir. Mac Gaunaa
Dr.ir. Jeppe Johansen

Lunderskov, July 24, 2017

Marijn Leendert Willy Veraart

Acknowledgements

First of all I would like to thank my main thesis advisor Rolf Hansen at LM Wind Power. He allowed this study to be my own work, but was always available to steer me in the right direction whenever he thought this was suitable or when I asked for his support. It was a real pleasure to collaborate with him making this study a great success.

I would also like to thank the other experts within the Aero Group at LM Wind Power, namely Jesper Madsen and Jordy van Kalken. Whenever I ran into a trouble spot or had a question about the research, they were available to discuss the problem and support me in finding a solution. Furthermore I want to thank Hans Paulsen for technical support in the wind tunnel, as well as Jacob Hovad for assistance with the Rain Erosion Test facility. Finally I want to thank all the other colleagues at LM Wind Power who made sure I had a great time while doing this research.

I would also like to acknowledge Mac Gaunaa of the Department of Wind Energy at the Technical University of Denmark and Nando Timmer of the Section of Wind Energy at the Delft University of Technology. I really enjoyed having their long-distance but helpful support via mail, phone and flawless Skype meetings.

Then I would also like to thank Christian Bak and Anders Olsen of the Department of Wind Energy at the Technical University of Denmark, for their participation and valuable input since the very start of the project, leading to successful model proposals and a perfect beginning of the project.

Ultimately, I would like to express my gratitude to my parents and to my sisters for providing me with unfailing support and continuous encouragement throughout my years of study and through the process of researching and writing this thesis. This accomplishment would not have been possible without them. Thank you.

Marijn Leendert Willy Veraart

Contents

List of Figures

List of Tables

CHAPTER 1

Introduction

In this project the deterioration in aerodynamic performance due to leading edge rain erosion is measured. A decrease in aerodynamic performance immediately demonstrates the main problem of leading-edge rain erosion, which is that it directly increases the cost of energy. While operating, the leading-edge of the wind turbine blade is exposed to wear and tear, resulting in a degradation of the surface material and therefore an increase in surface roughness. A rough surface will accelerate the transition development from laminar to turbulent flow. This will lead to a decrease in aerodynamic performance (also defined as a decrease in lift and increase in drag properties), directly resulting in a reduced annual energy production (AEP) and therefore an increase in cost of energy. The erosion phenomenon increases drastically for larger rotor speeds, which is highly important considering the general industry trend of ever-increasing rotor size. It should also be taken into account that the largest rotor sizes are operating at offshore sites, where maintenance costs are high and the durability of the blades (for both structural and aerodynamic performance) is of utmost importance.

The erosion patterns initiate and evolve at the leading edge in the tip region of wind turbine blades, where the leading-edge experiences high velocities and impacts with rain droplets. Besides the high velocities, the required twenty-five years of operational lifetime of a wind turbine makes the erosion a fatigue issue from a structural perspective, where the leading-edge erosion can become a problem in even less than one year [1].

From an aerodynamic perspective, erosion results in a roughened surface, which affects the aerodynamic performance negatively due to early flow separation and transition. The roughened surface at the leading-edge will accelerate the laminar to turbulent transition process of the flow, as roughness elements perturb into the laminar boundary layer and excite flow instabilities. Early flow transition and separation reduce lift, increase drag and impose unsteadiness that can also increase the blade vibrations.

There is an increasing need to improve knowledge on the aerodynamic performance loss, due to the up-scaling of offshore wind turbines. At offshore wind farm sites there are less noise limitations, allowing turbines to run at higher rotational velocities. These trends not only lead to blades operating at higher rotation velocity, but also to an increasing chord length. As can be seen from (1.1), increasing the chord length, as well as an increase in operational velocity, leads to higher experienced chord Reynolds numbers. An increase in Reynolds number subsequently results in a boundary layer thinner relative to the airfoil. Therefore with the up-scaling of wind turbines, the ratio between erosion (roughness) height and boundary layer thickness increases. Erosion now penetrates to a higher extent into the boundary layer, leading to early laminar to turbulent flow transition and decreasing the aerodynamic performance.

$$Re_c = \frac{\rho U_\infty c}{\mu_d} \tag{1.1}$$

1.1 Review on erosion studies

Previous erosion studies were primarily focused on surface roughness and to a lesser extent to leading edge erosion. In these studies surface roughness investigated can either be categorized as two-dimensional (2D, spanwise uniform) or three-dimensional (3D; span-wise variable) roughness. Most investigations were done regarding 2D roughness, as in the aircraft industry there is a higher risk for 2D roughness effects (consider that the aircraft wing surface consists of a riveted panel structure).

Current airfoil designs for wind turbines are validated for roughness sensitivity by using standardized roughness configurations, such as trip strips or zigzag tapes placed at multiple locations along the the leading-edge. Examples of these standardized roughness studies are from Fuglsang et al. [2] and van Rooij and Timmer [3]. Wind turbine blades potentially show more 3D roughness effects, which can be observed as a distributed erosion pattern, implying uncertainties to their roughness validation using standardized roughness configurations.

Recent studies of 3D roughness effects were mostly experimental and simulated erosion as a simplified distributed pattern at the leading-edge of an airfoil, which were tested in a wind tunnel to measure its impact to aerodynamic performance. Examples of studies performed by leading wind energy companies and scientific institutions are: using roughness tapes by Standish et al. (2010) at Siemens Wind Power [4], perforated tape by Gaudern (2014) [5] and a rapid-prototyped (RP) leading-edge by White et al. at Vestas Wind Systems [6], applying vinyl stickers by Langel et al. (2015) and Maniaci et al. (2016) at Sandia National Laboratories [7, 8] and a hand-tooled leading-edge by Sareen et al. (2013) at the University of Illinois [9].

The results of these studies all show detrimental effects of simulated erosion to aerodynamic performance, though both higher [5] or lower [6] aerodynamic performance was measured when comparing the performance to standardized roughness configurations (such as zigzag tape or trip strip). Langel et al (2015) [8] and Maniaci et al. (2016) [7] simulated erosion by applying randomly distributed circles as vinyl stickers to the leading edge. This indicated that for same roughness coverage applied, the roughness height is more important to aerodynamic performance than the roughness density.

In previous research different modelling methods of erosion patterns were used. However, most studies modelled the erosion inaccurately by adding material to the leading-edge, instead of removing material as a negative shape modification (except for the sand-blasting method, rapid prototyped leading edge and hand tooling [6, 9]). Accurately modelling different stages of erosion as a 3D distributed roughness, by removing material from the leading-edge of an airfoil, is therefore a major objective in this study.

In addition, in the prior research done, the roughness investigated resembled heavy erosion patterns, such as coating chipping off and erosion perturbing into to glass lay-up. This was combined with roughness coverages applied up to 15% chord length. In this study early erosion stages are investigated, showing the aerodynamic performance loss for erosion only perturbing into the coating. This also implies that significantly lower coverages should be applied.

Not only the modelling methods of erosion patterns are questionable to resemble realistic erosion patterns, also scaling methods applied leading to certain tested erosion thicknesses resulted in uncertainties. The previous erosion studies all tested the models at relatively low Reynolds numbers compared to operating chord Reynolds numbers as experienced in the tip section of a blade. To overcome this difference, the erosion thicknesses applied were scaled from observed erosion thickness to tested thickness. This scaling method is based upon keeping the roughness Reynolds number constant between operating and testing conditions. The roughness Reynolds number is stated in (1.2), where k is the roughness height (assumed to be equal to erosion thickness) which is scaled from observed erosion to tested erosion thickness. The wall shear stress tau_ω follows from an estimation using XFOIL at a certain operating or testing Reynolds number.

$$Re_k = \frac{\rho k^2 \tau_\omega}{\mu_d} \tag{1.2}$$

In addition to experimental methods, numerical methods were also proposed to investigate eroded and roughened surfaces. Using Computational Fluid Dynamics transition of the flow at two-dimensional airfoils can be predicted by implementing Langtry & Menter's local correlation-based bypass transition model (LCTM) [10, 7, 8, 4]. The Langtry-Menter model introduces two flow parameters and two transport equations that define the distribution between these two flow parameters [11, 12]. Therefore these work in conjunction with each other to compute the criteria the local flow has to meet to activate transition. When both the criteria are met, the local flow is transitioned to the fully turbulent model. This model requires heavy calibration to experimental models for a certain airfoil profile, showing the difficulties to predict flow conditions affected by erosion.

Furthermore, a full Direct Numerical Simulation (DNS) study was performed by Ribeiro et al. (2016) [13], where roughness grits were implemented at the leading edge of the airfoil. Applying only twelve spheres in spanwise direction, each having a certain diameter and chordwise packing density, resulted in more than two million CPU hours required to perform the simulations. Considering an erosion pattern consisting of many roughness features, performing a DNS simulation for now is considered to be infeasible.

1.2 Purpose and objectives

Studying how erosion influences the aerodynamic performance, or more specifically what the influence of a certain stage of erosion has on lift, drag, transition and on separation will be highly relevant. As stated before, this is difficult to predict in numerical simulations because of the many parameters three-dimensional roughness surface entails and computational cost. Therefore an experimental set-up using the LSWT is favourable.

Lift, drag and boundary layer measurements will deliver valuable information on transition and separation. From experiments it is directly measurable to what level a certain stage of erosion influences the lift and drag performance. Lift and drag results can be applied to a Blade Element Momentum (BEM) calculation, leading to an estimated loss in AEP for a certain erosion level. Performance losses due to certain stages of erosion will show the need for development and implementation of leading-edge protection solutions.

The objective is to determine the aerodynamic performance loss of an airfoil with 3D roughness, that simulates different stages of leading-edge erosion. At LM Wind Power (LMWP) a Rain Erosion Test (RET) facility is available, which creates realistic erosion patterns. Different erosion patterns as observed on RET specimens will be identified and charactered, making it possible to model erosion patterns based upon realistic erosion patterns. Subsequently these models will be tested for aerodynamic performance in the LSWT. The general aim is to show the impact of leading-edge erosion on aerodynamic performance, compared to standardized roughness configurations, in terms of lift, drag, transition and separation.

The usage of RET specimens to model erosion patterns is an unprecedented method. Identification and characterization of erosion patterns can be done highly accurately by using specimens from the Rain Erosion Tester. Now RET specimens are available that show early erosion stages with erosion coverage still close to the leading-edge, instead of the highly evolved erosion patterns observed from blade inspections. These RET specimens can be 3D scanned, making it possible to perform an accurate statistical analysis on the depth, shape, size and coverage of the erosion features. Finally testing of the erosion models in the wind tunnel will be performed at Reynolds numbers similar to operating conditions, up to $Re_c = 6 \cdot 10^6$ [14], and therefore at higher values than as performed in previous studies. Consequently, scaling of roughness heights between operating and testing conditions can be avoided, reducing the uncertainties due to scaling.

The corresponding research objectives for this study are:

1. Characterize different erosion levels at an early stage by analysing Rain Erosion Test specimens.
2. Model characterized erosion levels to make them applicable to an airfoil by scaling and transferring characterized erosion levels to a 3D model.
3. Investigate the aerodynamic performance of erosion levels by experimental testing in the low speed wind tunnel.
4. Compare aerodynamic performance erosion levels to standardized roughness configurations by performing wind tunnel tests with zigzag tape applied at different chord locations.

1.3 Selection of erosion models

Different methods can be utilized to create an eroded surface at the leading edge of an airfoil profile. Considering the timespan of this project, three different modelling methods could be designed and tested

in the wind tunnel, out of the different modelling methods initially proposed. Therefore a selection of erosion models was required, keeping in mind the research objectives and main requirements of modelling erosion based upon RET specimens. The three modelling methods proposed are:

1. The standardized roughness configuration (using zigzag tapes).
2. A quick erosion method (where the leading edge surface of an existing airfoil profile will be hand tooled).
3. A detachable leading edge model (separate leading edges can be modelled and 3D printed for each erosion level).

These methods are initially based upon previous erosion studies. The benefits and disadvantages of each method are stated, validating the selection of these models. A selection of the airfoil profiles for each modelling method is also included.

1.3.1 Standardized roughness (zigzag)

The first method considered is standardized roughness, where different zigzag tapes can be applied at the leading edge. This method adds material to the surface and does not resemble realistic erosion patterns. Because this method is used to validate airfoil profiles for roughness sensitivity, experiments should be performed using different zigzag tapes applied at different locations, to compare performance losses to realistic erosion models. Therefore the zigzag model is chosen as the first model to be investigated.

1.3.2 Quick erosion

The quick erosion method makes use of an existing airfoil profile, where erosion patterns will be hand tooled into the leading edge. By hand tooling the surface, material can be removed from the leading edge. Different methods are possible with respect to the hand tooling process, such as hammering, sand-blasting or brushing, where it is expected that the repeatability and controllability of these erosion application methods are problematic. This will heavily depend on the material properties of the surface material of the airfoil profile. A foam material airfoil profile is available at LMWP, where the surface material can be modified faster and easier as compared to an aluminium airfoil profile. A schematic drawing of the quick model is shown in Figure 1.1a.

As this method is relatively fast to apply erosion patterns to, and a foam airfoil profile is available, this method is chosen to be the second model to be tested. This model will show initial trends with respect to erosion depths and coverages, which can be compared to the zigzag model. It is uncertain how erosion patterns for the quick model will compare to RET erosion patterns. Still the quick erosion patterns can be analysed following the same method as the RET specimens, by means of 3D scanning of the patterns. This enables a validation of the quick erosion patterns to the RET specimens.

1.3.3 Detachable leading edge

A scientific approach to model the erosion is by using a detachable leading edge (DLE) model. This enables any surface modification possible, as the leading edge itself can be rapid-prototype (3D printed) in any shape required. Therefore this method is in full control, enabling realistic erosion shape modifications. A schematic drawing of the DLE model is shown in Figure 1.1b.

For each erosion level a detachable leading edge can be designed and 3D printed. While testing, the detachable leading edge can relatively easy be replaced with another leading edge (for a different erosion level). This is beneficial to testing times, where the airfoil profile itself remains installed in the wind tunnel during the full measurement campaign.

A disadvantage is the relatively high costs of designing a new airfoil profile (with a shortened and straight leading edge) and the 3D printing of leading edges. The designing and manufacturing of the new airfoil profile will take time, which needs to be taken into account with respect to the time schedule of the project. Also the DLE design results in a gap between the leading edge and the airfoil profile, potentially disturbing the flow and therefore affecting aerodynamic performance. Still a detachable

leading edge model is the preferred option to (experimentally) model erosion, enabling negative shape modifications and usage of the same airfoil profile for different erosion levels. Therefore this model is chosen as the third model, where designing and manufacturing of the model need to be initiated at the very start of the project.

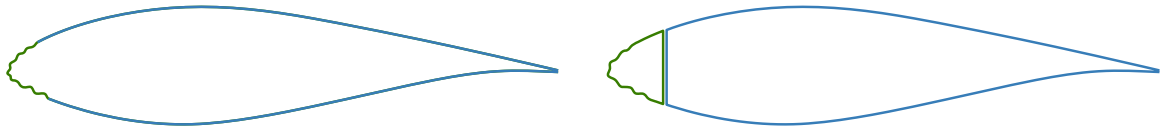

a Quick model **b** Detachable leading edge model

Figure 1.1: Different methods of modifying the leading edge surface to model an erosion pattern.

1.3.4 Selection of airfoil profiles

The zigzag and quick erosion model are based on the same airfoil coordinates, which is an LMWP tip airfoil of 18 % thickness. This airfoil profile therefore is called the *LM18%* airfoil. Exact coordinates of this profile are not included in this report, due to confidentiality. The zigzag model is an aluminium airfoil, whereas the quick erosion model is made out of a polyurethane foam material. Therefore these two models are two different models, but having the same airfoil coordinates (of an *LM18%* airfoil). Both these airfoil models were already available at the start of the project.

For the detachable leading edge model, a *DU-00-W212* airfoil profile is chosen, with a thickness of 21.2 %. Having this thickness the airfoil profile would be located more towards mid-span than in the tip region of the blade. This airfoil profile is publicly available and is a part of the Advanced Aerodynamic Tools for Large Rotors (Avatar) project. The Avatar project is initiated by the European Energy Research Alliance and is motivated by the up-scaling of wind turbines in the range of 10-20 MW, leading to design challenges in order to make these turbines feasible and cost effective. This study is partly funded by the Avatar project, as the leading edge erosion problem is considered to be one of these design challenges (considering the increased erosion effects due to up-scaling of offshore wind turbines). Therefore all design steps and aerodynamic performance results of the detachable leading edge model are made public. In addition, at LMWP an aluminium *DU-00-W212* airfoil is available, making it possible to validate the performance results of the DLE model to the original aluminium *DU-00-W212* model.

In Figure 1.2 the coordinate system of the airfoils is shown, as will be used throughout this report. x-direction is along the chord, originating at the leading edge, whereas y-direction is normal to chord and span, originating at the leading edge, and finally z-direction is along the span. All three airfoil models have a chord length of 900 mm. The pressure side of the airfoil is the downwind location as seen on a blade, whereas suction side is the upwind location.

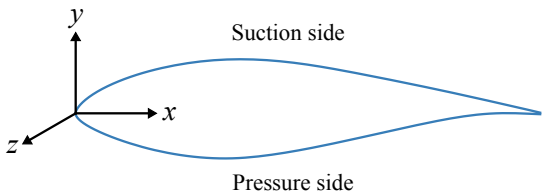

Figure 1.2: xyz coordinates for chordwise distance, thickness and spanwise distance.

1.4 Report structure

At first, Chapter 2 provides a thorough explanation on how aerodynamic performance was measured, in terms of lift, drag and transition location. An investigation of a boundary layer rake is included, scoping the possibility if boundary layer measurements are possible. Erosion patterns are identified and characterized in Chapter 3, based upon three dimensional scans of Rain Erosion Test specimens. This leads to erosion pattern characteristics as well as a method to scale erosion coverage from the RET specimens to a leading edge surface.

As determined from the model selection, three different erosion models are designed to incorporate erosion and tested in the low speed wind tunnel. In Chapter 4 the standardized roughness configurations which utilize zigzag tapes are discussed, as well as the resulting aerodynamic performance losses for the different configurations. Then in Chapter 5, the quick erosion model is described. This includes the method of erosion application by means of hand tooling, as well as a validation of the created erosion patterns to the RET erosion specimens. Aerodynamic performance losses are computed and compared to the zigzag model. Also for the quick model a method is described how the established erosion data can be incorporated in a BEM calculation, leading to an estimation for AEP loss due to erosion. The third and final model reviewed is the detachable leading edge model in Chapter 6. This includes the design of the detachable airfoil model itself, a description of the modelling of the erosion patterns for the DLE and how these modelled erosion patterns can be applied to a leading edge surface. As well as for the quick model, a validation is performed comparing the modelled erosion patterns to the RET erosion specimens. Finally the aerodynamic performance results are compared to the quick and the zigzag model.

A discussion on the main results of the three models is included in Chapter 7. In this section, the quick and the DLE model are compared to the zigzag model. This discussion considers both the different modelling approaches, as the aerodynamic performance results. Final conclusions on the research performed are stated, as well as recommendations for future research in the field of leading edge rain erosion.

CHAPTER 2

Measuring aerodynamic performance

Aerodynamic performance can be measured in terms of lift and drag forces, as well as on transition and separation location. By means of infrared thermography the transition location can be found. Pressure taps, the wake rake and load cells can measure lift and drag. Finally a boundary layer rake was tested to investigate if boundary layer measurements could be performed, also giving information on transition and separation location.

2.1 Infrared thermography

Using infrared (IR) thermography the transition location of the flow on the airfoil can be estimated. While operating the wind tunnel, an infrared lamp heats up the suction side surface of the airfoil. Cooler, ambient air cools down a turbulent surface region faster than a laminar region, resulting in a steep temperature gradient on the airfoil surface. This difference in surface temperature, and therefore the transition location between laminar and turbulent flow, can be visualized using infrared thermography. The IR thermography method was used by Ehrmann et al. (2013) [10] and by Maniaci et al. (2016) [7] to capture the effect of erosion on transition location.

This IR method only works on the quick airfoil model in Chapter 5 due to low thermal conductivity of the airfoil material, where the foam material results in a sufficient temperature difference. The DLE airfoil model in Chapter 6 was build using an aluminium surface and has a high thermal conductivity, where the material cools down equally along the surface. Here a difference in temperature, and therefore transition location, cannot be captured using IR thermography.

The IR lamp and camera were placed in the ceiling of the wind tunnel, pointed at the surface of the airfoil suction side. Operating the FLIR A325 IR camera was done using the FLIR Camera Player software package. This program is a PC based remote control and viewer, enabling focussing of the IR camera remotely. Also frames from the video stream could be saved directly as a snapshot image. The colour palette was set to purple for a clear visualisation of temperature difference.

In Figure 2.1 four images are shown for the clean quick (*LM18%*) airfoil model, at $Re = 3 \cdot 10^6$ and increasing angle of attack. The resolution of the IR camera is low with 320 by 240 pixels. Therefore locating the transition point from an IR image is inaccurate, and is considered to be an estimation. Still at a constant Reynolds number and for increasing angle of attack, a forward shift of transition location towards the leading edge is clearly visible. For the clean airfoil in Figure 2.1a, at zero angle of attack the transition location is at approximately $x_t \approx 50\%$, shifting forward to $x_t \approx 5\%$ for $\alpha = 11°$ in Figure 2.1d. In case of erosion at the leading edge, the transition location is expected to shift forward due to early induced flow transition. This shift in transition location can be compared for increasing erosion levels.

To locate the transition from IR images, predetermined chord interval ticks were marked on the airfoil surface. Normal ink cannot be seen using an IR camera, as normal ink will have the same temperature as the surface where it is applied. Marking of these ticks was possible using an ink that contains silver particles; the ink will reflect the infrared light of the lamp into the camera, making the markings visible. Markings were set at $x = 5, 10, 20, 30, 40$ and $50\%c$.

As can be seen in Figure 2.1, only for a fraction of the airfoil surface a distinct temperature difference showed up between light yellow/orange and dark purple zones. This area is approximately up to half of the airfoil in spanwise direction, and results from the IR lamp being pointed to this half of the airfoil. Subsequently the other half was located in an infrared 'shadow', not being heated sufficiently to show a clear temperature difference.

In Figure 2.1b both the wall interference and a vortex cone can be seen. The wall interference effect for higher angles of attack results in a transition location at the wall located directly at the leading edge, while gradually shifting backwards moving to the middle section of the airfoil. A turbulent vortex is visible as a cone in the shadow (dark purple) part of the laminar region, initiated at the LE probably due to a contamination or particle present at the surface.

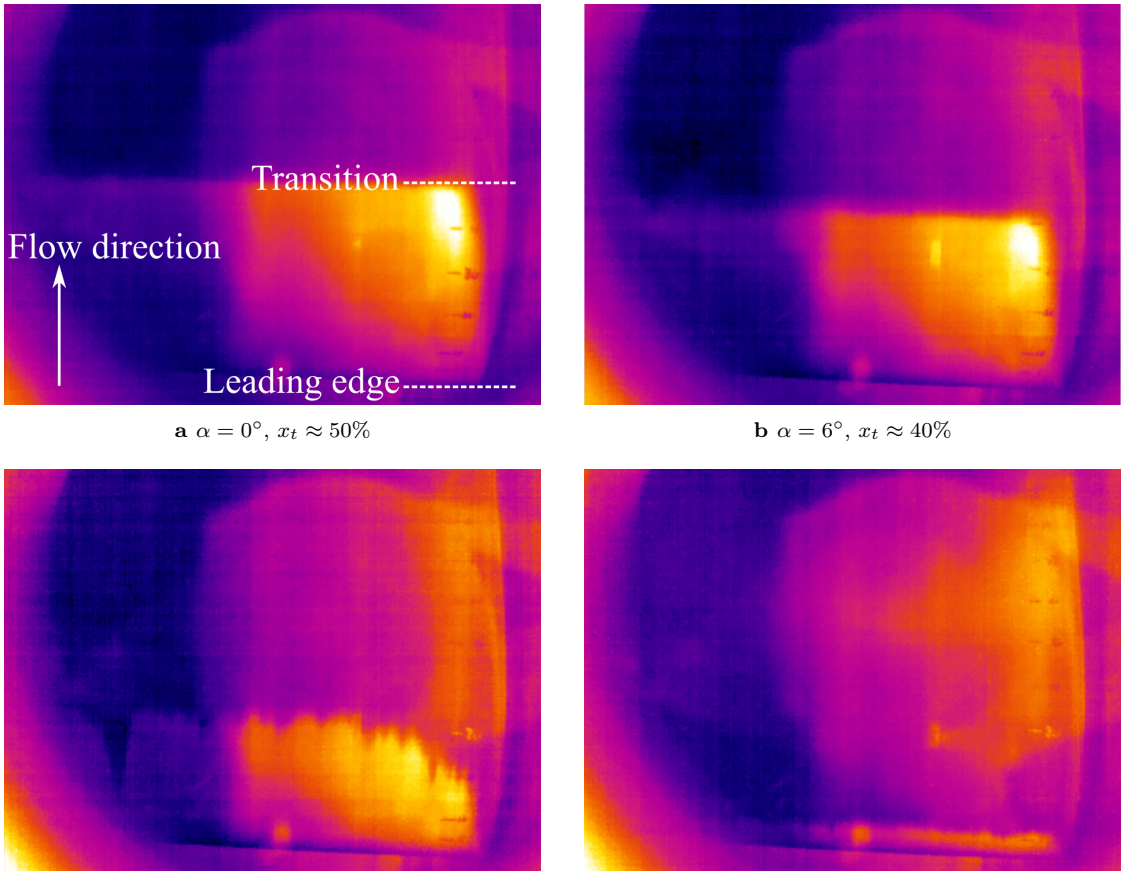

a $\alpha = 0°$, $x_t \approx 50\%$ **b** $\alpha = 6°$, $x_t \approx 40\%$

c $\alpha = 8°$, $x_t \approx 30\%$ **d** $\alpha = 11°$, $x_t \approx 5\%$

Figure 2.1: IR visualisation of shift in transition location for increasing angle of attack ($Re = 3 \cdot 10^6$).

2.2 Pressure taps

By means of pressure taps, the pressure distribution and subsequently the lift coefficient could be determined. Pressure taps are small holes located perpendicular to the surface, along the complete airfoil surface and measure the local static pressure. This results in the pressure distribution around the airfoil and subsequently a computation of the lift force. Measuring the pressure distribution and lift using pressure taps was done by most of the previous erosion studies performed by Standish et al. (2010)[4], White et al. (2011) [6], Ehrmann et al. (2013) [10], Langel et al. (2015) [8],

Maniaci et al. (2016) [7] and Bak et al. (2016) [15]. Incorporation of pressure taps was done in the DLE model and standardized roughness model. In the quick model, no pressure taps are designed because of manufacturing restrictions of the foam material.

Flow around the airfoil is assumed to be tangent to the surface, making the pressure taps perpendicular to the local flow direction and pressurized by the static pressure. The pressure of the pressure taps was measured by tubes that connect the taps to a pressure transducer. A transducer measures the difference in pressure between pressure in the tubes and a reference pressure. The reference pressure of the transducer is atmospheric pressure, where the pressure modules are zeroed against the reference pressure twice a day.

The lift force was computed from the pressure distribution, by integrating the pressure distribution along the chord as shown in (2.3), where the drag coefficient C_d was measured using the wake rake as explained in Section 2.3 [16]. The pressure coefficient C_p was computed for each pressure tap as stated in (2.1), resulting in the normal force coefficient C_n stated in (2.2).

$$C_p(s) = \frac{(p_i - p_\infty)}{q_\infty} \tag{2.1}$$

$$C_n = \frac{1}{c} \int C_p(s) \, \boldsymbol{tds} \tag{2.2}$$

$$C_l = C_n \cos\alpha + C_d \tan\alpha \tag{2.3}$$

From the pressure distribution, there could be determined if the flow is laminar, turbulent or separated. Also an approximation of transition location could be determined. In Figure 2.2 the pressure distributions for three angles of attack and their corresponding lift coefficients are shown for the clean *LM18%* airfoil (no erosion), at $Re = 3 \cdot 10^6$. The negative and positive axes of the pressure distribution in Figure 2.2a are switched, to visualize negative relative pressure correctly with suction (upper) side of the airfoil and positive relative pressure with pressure (lower) side.

For $\alpha \approx 5°$, the pressure distribution shows a laminar flow which is fully attached till approximately 50% chord, where the lift coefficient is on the linear part of the $C_l(\alpha)$ curve. Behind 50% chord the adverse pressure gradient leads to transition. At $\alpha \approx 10°$ the maximum lift coefficient is reached, and the pressure distribution now shows a clear pressure peak at the suction side close to leading edge, followed by a high adverse pressure gradient (transition). Finally in the stall region, where $\alpha \approx 11°$, the pressure distribution flattens out on the suction side, showing fully separated flow after transition. For each α, the stagnation point is the high pressure peak on positive pressure (lower) side. The stagnation point shifts backwards for increasing angle of attack, towards trailing edge on pressure side. For increasing erosion levels within this range in angles of attack, changes in the pressure distributions and associated flow conditions such as early transition could be analysed.

2.3 Wake rake

Profile drag was computed using the wake rake and the momentum deficit approach, and was also used by most of the previous erosion studies: Standish et al. (2010) [4], White et al. (2011) [6], Ehrmann et al. (2013) [10], Sareen et al. (2013) [9], Gaudern (2014) [5], Langel et al. (2015) [8], Maniaci et al. (2016) [7] and Bak et al. (2016) [15].

The wake rake consists of fifty-four total pressure tubes and two static pressure tubes, where each of the tubes is connected to the pressure measuring transducer. Solving the Bernoulli equation by subtracting the static pressure from the local total pressure measurements as shown in (2.4), led to the individual dynamic pressures. The static pressure in the wake was assumed to be constant along y-direction.

$$q_w = p_{t,w} - p_w \tag{2.4}$$

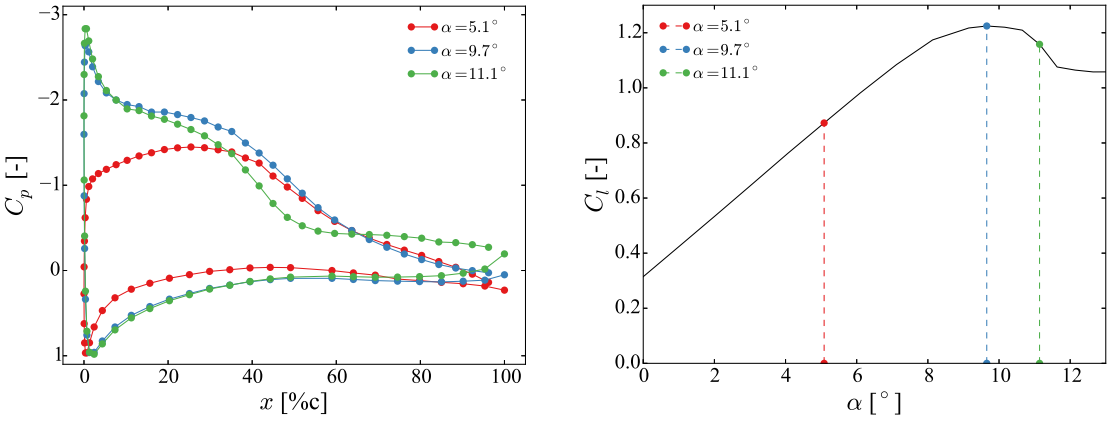

a C_p versus x **b** C_l versus α

Figure 2.2: Airfoil pressure distribution and corresponding lift coefficient for $\alpha \approx [5, 10, 11]°$ for *LM18%* airfoil ($Re_c = 3 \cdot 10^6$).

The local dynamic pressure distribution is shown in Figure 2.3a for zero angle of attack for the *LM18%* airfoil, at the centre span position ($z = 0\,\text{mm}$). The pressure deficit in the wake is clearly visible. Integrating the local dynamic pressures in the wake as stated in (2.5), led to the drag coefficient at this specific span location. Freestream dynamic pressure q_∞ is computed from the local dynamic pressure outside of the wake measurement, which in Figure 2.3a is the approximately constant value just above 1450 Pa).

As can be seen in Figure 2.3a, scatter in the measured pressure data occurs outside of the wake in the linear part. To filter the data from scatter, before integration the linear pressure value is calculated as the average of the top and lower three data points from the wake rake data. After this, the minimum pressure is found (the peak of the wake). Starting at minimum pressure, moving up in y-direction the first point is found with a pressure higher than the averaged linear value. Shifting one point down, this is the first data point between where the integration occurs (therefore assumed to be the end-point of the wake). Again starting at minimum pressure, this time moving down in y-direction, the first point is found with pressure higher than averaged linear pressure. Shifting one point up, this is the second data point between where integration occurs and assumed to be the starting point of the wake.

$$C_d = 2 \int \left(\sqrt{\frac{q_w}{q_\infty}} - \frac{q_w}{q_\infty} \right) d(y/c) \tag{2.5}$$

The wake rake is traversing along the full span of the airfoil, resulting in the drag coefficient measurements at a range of z-locations as shown in Figure 2.3b. Finally the drag coefficient of the airfoil was determined by taking the average of drag coefficient measurements.

At high angles of attack the wake will become too turbulent leading to unrepeatable and unstable measurements. Therefore the drag measurements in the stall region were set to zero, as can be seen for the wake rake drag coefficient measurements in Figure 2.4b.

2.4 Load cells

Another method used to calculate the lift and drag coefficients was by measuring the lift or drag force directly using the load cells, as used in the erosion study by Sareen et al. (2013) [9]. The load cells measure the total lift and drag, which was divided by the airfoil spanwise length to compute the sectional lift and drag coefficient. On each side of the airfoil there were three load cells located, where

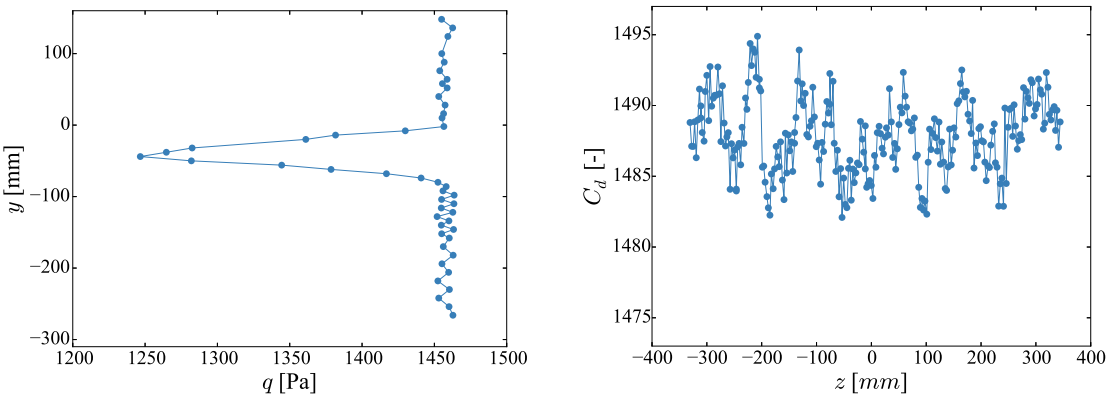

a q versus y **b** C_d versus z

Figure 2.3: Local wake dynamic pressure and drag coefficient for $\alpha = 0°$ for *LM18%* airfoil ($Re_c = 3 \cdot 10^6$).

two cells measured the normal load (up to 700 kg per cell) and one cell measured the transversal load (up to 200 kg per cell).

The load cells result in a misinterpretation when capturing the two-dimensional lift and drag force correctly, as the cells will measure all three-dimensional effects including the wall effects. In Figure 2.4 the lift and drag coefficient is compared for the *LM18%* airfoil, at $Re = 3 \cdot 10^6$, between the load cells and pressure taps for the lift, and between load cells and the wake rake for the drag.

In Figure 2.4a the lift coefficient measured by the load cells and measured by the pressure taps differs is shown, giving similar results. The drag measured by the load cells in Figure 2.4b did not match the more accurate results measured by the wake rake. This is partly due to the three-dimensional wall effects measured by the load cells. For drag measurements using the wake rake, no measurements were taken in the deep stall region at angles of attack lower than −13 ° or higher than 12 °. Meanwhile, load cell drag becomes more accurate outside the drag bucket, and is directly comparable to airfoil pressure drag.

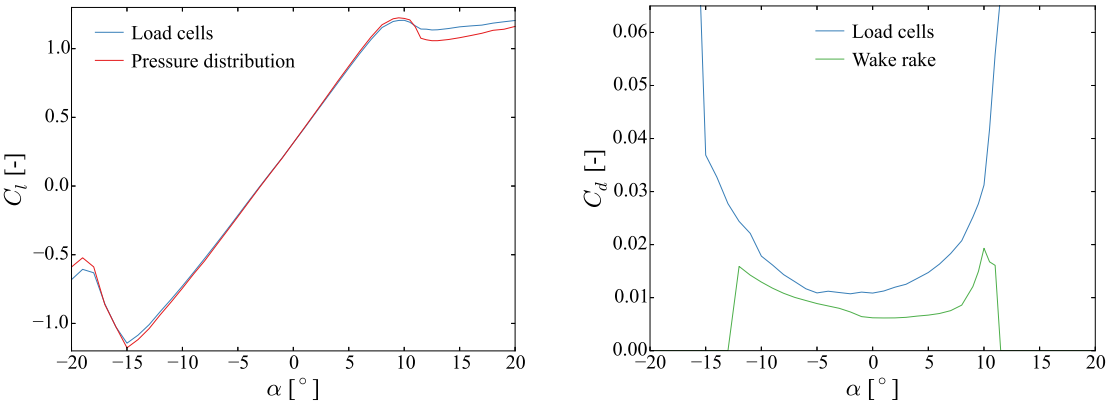

a C_l versus α **b** C_d versus α

Figure 2.4: Lift coefficient and drag coefficients for *LM18%* airfoil ($Re_c = 3 \cdot 10^6$).

2.5 Boundary layer rake

The impact of erosion could also be investigated by inspecting changes in the boundary layer velocity profile at certain chord locations on the airfoil. These potential changes can indicate early transition or separation. The boundary layer velocity profile can be captured by means of a boundary layer rake (BLR). A BLR measures the pressure and velocity distribution close the airfoil surface, from where can be determined if the flow is laminar, turbulent or separated. This method was also applied to the erosion studies by Ehrmann et al. [10] and White et al. [6].

A schematic representation of the velocity profile for subsequently laminar, turbulent and separated flow can be seen in Figure 2.5. The no-slip condition results in zero velocity directly at the airfoil surface. For laminar flow, no chaotic mixing (only particle mixing) of flow perpendicular to the surface occurs, and is located in the region close to the leading edge up till the transition point. In a turbulent flow there is mixing between the layers, which will occur after the transition point. Also for a turbulent flow the velocity increases faster moving up from the surface when comparing to a laminar velocity profile, caused by a higher skin friction drag. Finally flow separation leads to a change of direction of the slow moving flow at the surface, which occurs towards the trailing edge after the separation point.

Changes in the boundary layer velocity profiles can be captured between different erosion levels, for certain angles of attack, Reynolds numbers and chord locations.

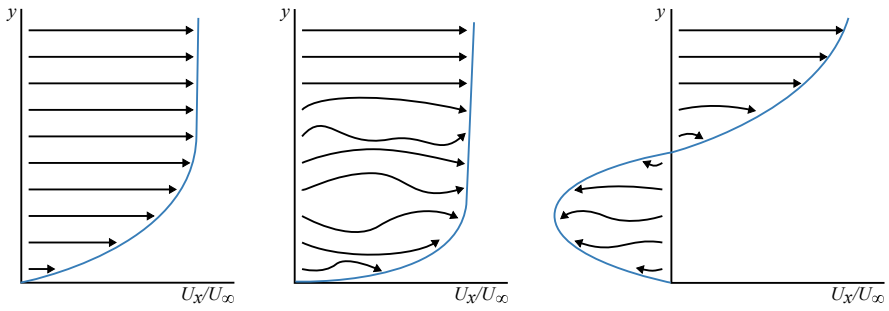

a Laminar **b** Turbulent **c** Separated

Figure 2.5: Schematic velocity profiles for laminar, turbulent and separated flow.

2.5.1 BLR design

A boundary layer rake was designed in collaboration between LMWP and DTU, initially to investigate the boundary layer at the side walls of the wind tunnel. This BLR consists of 22 total pressure tubes, placed in a tube-mount, perpendicular to the airfoil surface and pointed opposite to the flow direction (therefore into the flow). The distribution of the pressure tubes in the tube-mount is shown in Figure 2.6, where the leftmost hole holds the tube which is located closest to the airfoil surface. The resolution is higher (distance lower) for the tubes at the airfoil surface, and decreases for increasing height.

A total pressure tube measures the local total pressure. This total pressure acts as an input to the Bernoulli equation. The static pressure is taken from the pressure tap in the airfoil surface, closest to the location of BLR. As for classical boundary layer theorem, it is assumed that the static pressure is approximately constant inside the boundary layer and is determined by the flow outside of the boundary layer. Therefore with the total pressure distribution measured from the BLR, and the static pressure measured from a pressure tap, the dynamic pressure and resultantly the local flow velocity could be computed.

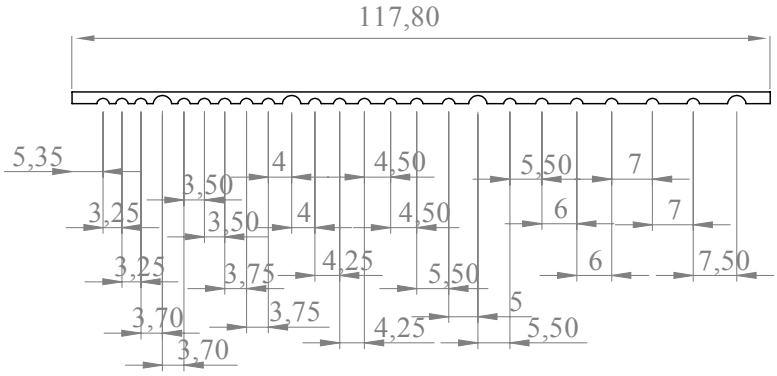

Figure 2.6: Tube-mount distribution BLR (h in mm).

2.5.2 Placement

The BLR was placed with its foot directly onto the airfoil surface at the very trailing-edge. This resulted in having the BLR foot placed normal to the airfoil surface. Due to the length of the tubes and the curvature of the airfoil, the direction of the entrance of the pressure tubes was slightly misaligned with the airfoil surface.

This led to a misalignment of approximately 1.08 ° with respect to the airfoil surface and flow direction (assuming the streamlines along the airfoil follow the airfoil curvature). For a pressure tube with cut head as used in the BLR, a misalignment of 11 ° is allowed according to Gracey et al. (1951) [17]. Here the cylindrical tube insensitivity to inclination is at lowest 11 ° at free-stream velocity of Mach 0.26 , which is approximately 88 m/s. It should be kept in mind that the initial BLR wind tunnel tests were lower up to 50 m/s.

2.5.3 Initial test

As it was uncertain if the resolution of the BLR was sufficient to capture the boundary layer at testing conditions similar to the erosion model experiments, an initial BLR experiment was performed. Similar testing conditions required that the chord Reynolds number was set up to three million. The experiment was performed at an LMWP airfoil with 24% thickness, which at that point in time was set-up in the LSWT for a different project. Performing this experiment at a different airfoil was chosen due to time and availability of the LSWT, already having an airfoil set-up.

The BLR was placed at the trailing edge, with entrance of the tubes approximately located at 85% chord. This was relatively close to the trailing edge, because it was expected that the boundary layer thickness was highest close to the trailing edge. In theory the boundary layer thickness increases while traversing over a surface.

To validate the results, a free-transition Computational Fluid Dynamics (CFD) study was performed that computed the boundary layer thickness along the chord, for different angles of attack and Reynolds numbers. In this study the resolution of the BLR could also be compared to the theoretical boundary layer thickness. The CFD study was executed with support from the Aero Group at LMWP, and a detailed methodology of the EllipSys CFD tools will not be discussed in this project.

The CFD computed boundary layer thickness is also shown in Figures 2.7 and 2.8, as horizontal dashed lines where the colour of the line matches the testing conditions of the colour of the BLR results.

In Figure 2.7 the BLR and CFD results can be seen for increasing angle of attack at chord Reynolds number of three million, where Figure 2.7a shows the pressure distribution and Figure 2.7b the velocity distribution.

For $\alpha = [-4, 0, 5, 8, 10]^\circ$ no clear boundary layer velocity profile could be identified. At zero height the velocity was set to zero due to the no-slip condition, there is no pressure tube located at zero height. The velocity appears to increase till free-stream flow velocity in less than 20 mm. Therefore it

was expected that the boundary layer thickness was also less than 20 mm, which would match with the boundary layer thickness computed by CFD for $\alpha = [-4, 0, 5]^\circ$ (for $\alpha = [8, 10]^\circ$ the CFD results in a higher thickness).

For $\alpha = 12^\circ$ the pressure was measured to be negative for all pressure tubes in Figure 2.7a. This negative pressure is a result because of flow separation, and negative flow in the separation bubble.

Also for several tubes in the BLR, distinct outliers in the results show up. The outliers do not follow the constant curve between 20 mm and 60 mm thickness, though appear also to occur closer to the surface. Probably these outliers were caused by dirt in the total pressure tubes or in the tubes connecting them to the pressure transducer, or pinching of the tubes.

It can be concluded that the resolution of the BLR is too low to capture differences in the velocity profile for increasing angles of attack. Furthermore, the tubes should be cleaned properly to avoid outliers due to dirt.

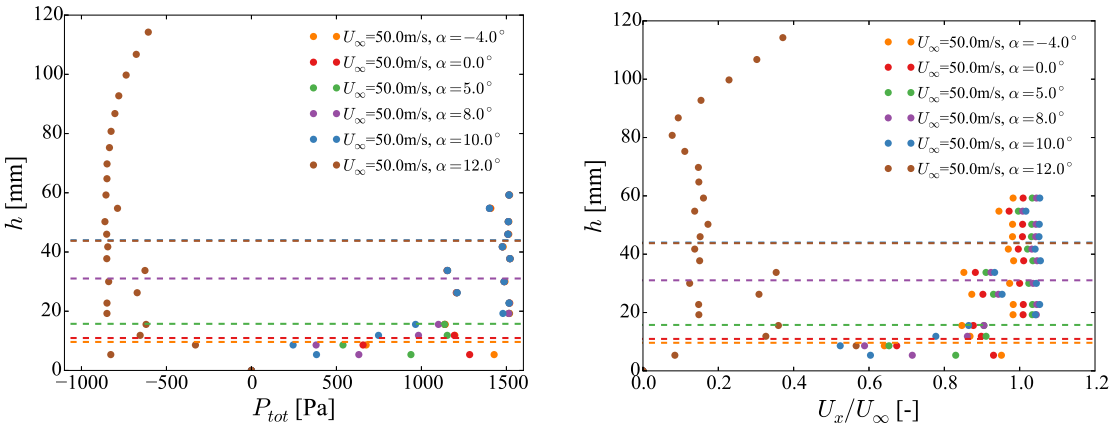

a Pressure distribution

b Velocity distribution

Figure 2.7: Boundary layer for increasing angle of attack ($Re_c = 3 \cdot 10^6$).

In Figure 2.8 the BLR and CFD results can be seen for increasing chord Reynolds number at zero angle of attack, where Figure 2.8a shows the pressure distribution and Figure 2.8b the velocity distribution. Again the results do not show a clear velocity profile, with a boundary layer thickness less than 20 mm. This also matches the CFD computed boundary layer thickness for $U_\infty = [25, 50]/\mathrm{m}s$. Also the outliers of the individual pressure tubes are clearly visible.

2.5.4 Conclusion on BLR

It was concluded that the BLR cannot be used to determine changes in flow transition and separation due to increasing erosion. This is mostly due to the fact that the resolution of the rake is too low to capture the boundary layer velocity profile. Only back-flow in the stall region at a high angle of attack resulted in a clear velocity profile. Also the BLR resulted in a scatter probably caused due to dirt in the pressure tubes, though cleaning the tubes will not improve the resolution of the rake. Therefore in this project the direct influence of erosion to the boundary layer velocity profile cannot and will not be investigated.

The resolution can be improved by placing the rake tilted in an angle instead of perpendicular to the airfoil surface, or by changing the shape of the rake to a an arc such as proposed by Bui et al. (2000) [18] for the design of a boundary layer rake. These configurations would result in a smaller distance between the total pressure tubes, as can be seen in the schematic drawing of the improved configurations in Figure 2.9. The design, manufacturing and validation of a new BLR is not a part

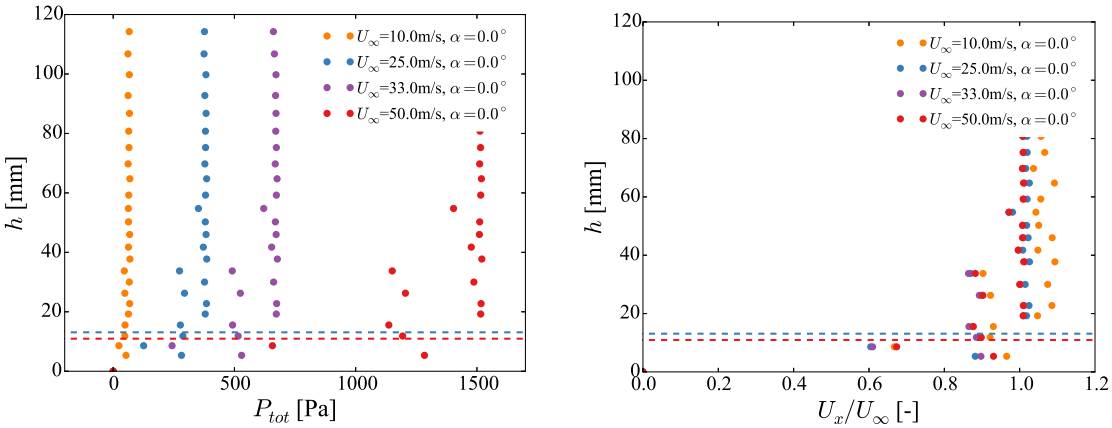

a Pressure distribution

b Velocity distribution

Figure 2.8: Boundary layer for increasing chord Reynolds number ($\alpha = 0°$).

of this project and therefore boundary layer measurements will be excluded from further aerodynamic performance measurements.

Besides using a BLR with total pressure tubes and a different shape configuration, another option to improve the resolution is to use hot-wire anemometry. This method allows local measurements of the flow with reduced spacing between the measurements. Currently there is no hot-wire anemometry set-up in the LWST and therefore this method could not be used.

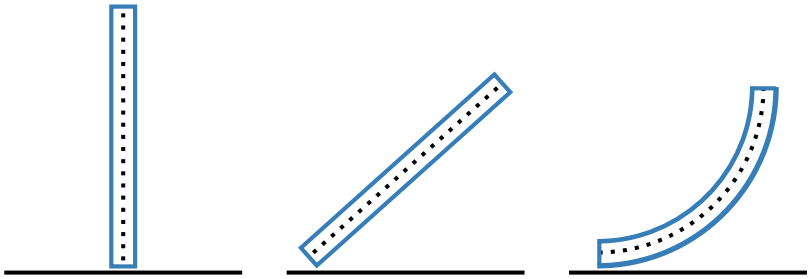

a Original

b Tilted

c Arc

Figure 2.9: Boundary layer rake configurations with tilted and arc for improved resolution.

CHAPTER 3

Characterization of leading-edge erosion

3.1 Establishment of erosion

Erosion patterns were established by means of the Rain Erosion Tester (RET) facility at LMWP. Using this experimental set-up, erosion patterns were created and selected from specimens that comply with the mass loss curve, based upon early erosion levels perturbing only into the coating. Subsequently these specimens could be analysed to find erosion roughness characteristics and statistics. To model erosion scientifically, the erosion surface is based upon these characteristics and statistics as determined from the RET erosion specimens.

A brief explanation of the RET set-up and specimens is given, followed by the method how these specimens were analysed using three-dimensional scanners, including surface inspections using GOM INSPECT software and two-dimensional roughness analysis.

3.1.1 Rain Erosion Tester

The RET apparatus as shown in Figure 3.1a consists of three rotating arms connected in its centre (similar to a wind turbine rotor), with a leading edge (LE) specimen attached to the end of each arm. As the most exposed part of the blade is the LE, tested specimens are shaped close to the LE geometry shape of a symmetrical NACA tip airfoil profile.

These specimens were made internally at LMWP, where coating and lay-ups were applied to represent the same material, application method and quality levels, as they appear on an actual blade. The composite lay-up is designed to avoid buckling during testing at high velocity, and to create a surface and fibre architecture similar to the leading edge of a blade. A cross-section of the specimen is shown in Figure 3.1b, where the dimensions are shown, as well as the lay-up of three Biaxial 450 glass layers and one outer gel-coat layer. The total length of the specimens tested is 225 mm. The average gel-coat thickness for the samples is measured to be approximately 400 μm. Anything below this depth, is assumed to be erosion perturbing into the glass lay-up.

Horizontal rotation of the arms is performed at high velocity (up to a tip speed of 178 $^{m}/_{s}$) through a simulated rain field, with droplet size similar to rain, falling from nozzles and hitting the specimen. Now the high speed impact from droplets provides an accelerated lifetime evaluation of rain erosion at the LE.

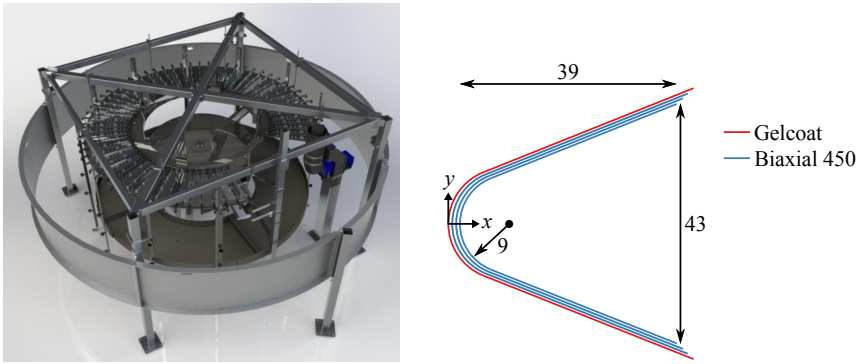

a RET apparatus **b** Cross-section specimen in millimetre

Figure 3.1: Rain Erosion Tester apparatus and test specimen.

3.2 Erosion phases identification: erosion mass loss curve

In the RET, the weight loss of the specimens is measured. Previous studies have shown that the material mass loss of specimens subject to impacting water droplets corresponds to the amount of droplets impacting the surface (or time). This was addressed in literature by Baker et al. (1966) and by Springer et al. (1974) [19, 20], as well as by in-house unpublicised studies at LMWP. These studies investigated the resistance of surface material to impact erosion and showed that there are three specific levels of erosion.

In the first level, zero mass loss and no erosion occurs, therefore the surface material remains intact. In the second level, erosion starts to occur and the mass loss follows a linear curve with respect to the increasing amount of droplets. In this level, erosion perturbs only in the coating, and deterioration of only a single material type results in a linear-mass loss. Finally, in the third level, erosion evolves to an extend that also the glass lay-up is affected. Now both coating and glass/resin will chip off from the surface, resulting in a random mass loss curve as different material types are removed. A schematic representation of the mass loss curve with zero, linear and random mass loss is shown in Figure 3.2.

As explained in Chapter 1, important in this study is to investigate how the early erosion (only damaging the coating) will affect the aerodynamic performance. Therefore erosion phases need to be investigated that are located within the second erosion level (where linear mass loss occurs). Based upon the linear mass loss curve and knowing the weight loss of the specimens in the RET, three erosion phases could be selected from different specimens.

The first phase is located right after incubation on the linear mass loss curve, where incubation is the point where surface damage becomes visible to the human eye. The second phase was selected where the mass loss has increased, but is still located on the linear mass loss curve. Finally the third phase was chosen to be in the beginning of the third erosion level, where the glass lay-up is also affected. The locations of the three selected erosion specimens with corresponding phases on the mass loss curve are also shown in Figure 3.2.

At the leading edge of the RET specimens, erosion is heaviest in the tip section due to the higher rotational speed. Therefore three different RET specimens were selected, where for each of the specimens only the tip region (with an approximately consistent erosion pattern) was considered.

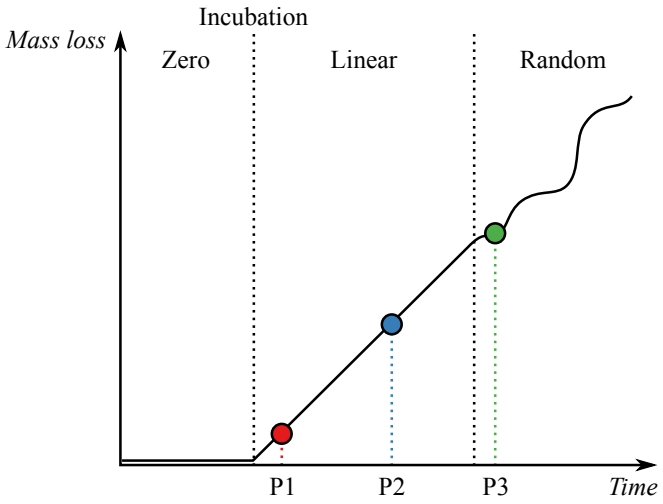

Figure 3.2: Material mass loss curve for increasing number of rain droplets (time), with Phase [1,2,3] erosion indicated.

3.3 Characteristics and statistics

Three-dimensional scans of the RET specimens were made. These were analysed by extracting two-dimension roughness curves as individual sections from the 3D scans. Extracting 2D roughness curves from the 3D scans was necessary as the roughness characteristics change with y-location (which is the distance from centre of RET specimen going up to suction or down to pressure side). After extracting the 2D roughness curves for different y-locations, the 2D roughness characteristics and statistics were computed, where these sectional characteristics depend on y-location. These characteristics and statistics are the basis for modelling the erosion in the detachable leading edge design in Chapter 6. Also transferring the coverage of the erosion from the RET specimens to a model was based upon these sectional characteristics.

3.3.1 Three-dimensional scans

With three erosion phases identified, the next step is the characterization of the erosion patterns. To analyse the patterns, the selected erosion phases were scanned by means of three-dimensional scanners. This scanning procedure was done at Zebicon and made use of GOM ATOS scanners, resulting in 3D polygon files with triangulated surfaces, also known as stereo-lithography (STL) files.

A render of the three STL erosion scans can be seen in Figure 3.3. The increase in erosion (material-loss) is clearly visible going from Phase 1 to Phase 3 erosion, where for Phase 1 only the coating is affected, while for Phase 3 erosion the material chipping off has reached the glass lay-up.

These scans cannot be transferred directly to the shape of a leading edge of an airfoil, as the cross-section is different between the RET specimens and any arbitrary airfoil leading edge. There is no scientific approach to scale and shape the STL files directly and therefore an erosion model needs to be designed from the very start. This model needs to be based upon the characteristics and statistics as computed from the RET erosion scans.

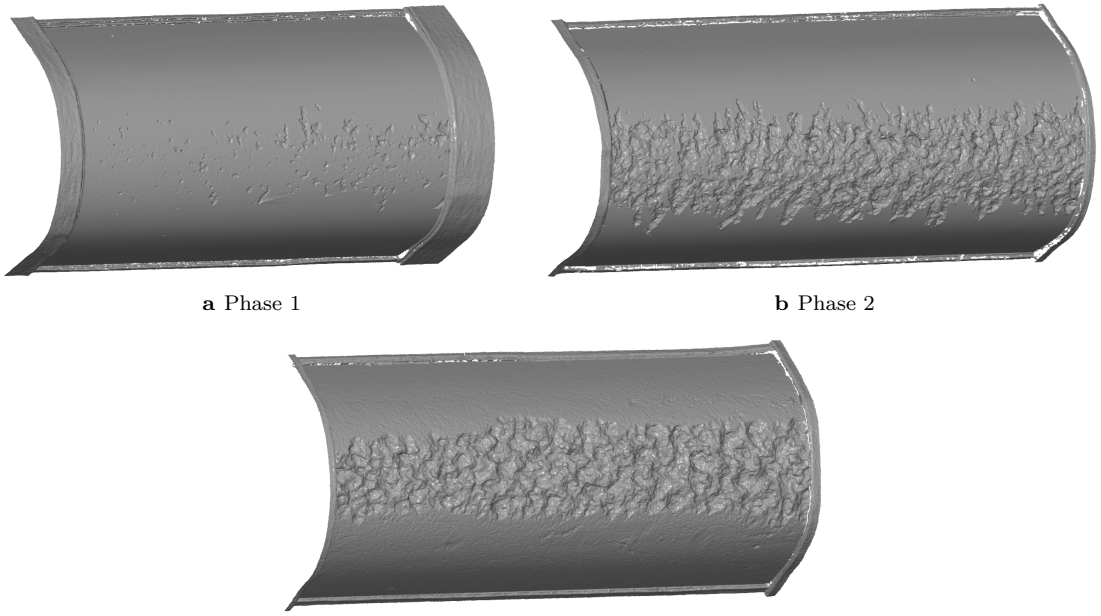

a Phase 1

b Phase 2

c Phase 3

Figure 3.3: Three-dimensional scans of Phase [1,2,3] erosion (y in [mm]).

3.3.2 3D scan to 2D roughness curves

A sectional analysis can be performed by first doing a three-dimensional surface comparison between the 3D scan and the original geometrical form. This 3D surface comparison can be done by using GOM Inspect software. From this surface comparison, cross-sections can be extracted at different y-locations. These sections resultantly appear as two-dimensional roughness curves. Finally 2D roughness curves can be investigated for roughness parameters.

3.3.2.1 Alignment

A 3D surface comparison measures the surface deviations between the erosion scan and the original geometry. In Figure 3.1b it can be seen that the leading edge of the RET specimens has a 9 mm radius. Therefore a CAD drawing with a cylinder of 9 mm radius (and a length longer than the 3D scans) is loaded into GOM Inspect, as the original geometry (also known as the nominal element).

The 3D scans originally also consist of the uneroded straight parts of the surface, outside of the radius at the borders of the specimens, as can be seen in Figures 3.1b and 3.3. These parts were cut-off from the scan before the pre-alignment was performed, to increase the precision of the automated alignment process in GOM Inspect.

Now the pre-alignment aligned the cut 3D scan automatically to the CAD drawing of the cylinder. This was carried out with an automatic global best-fit alignment, making the average deviation between the 3D scan and the CAD cylinder as small as possible. Finally, a manual rotation of the 3D scan along the z-axis was applied, making it possible to rotate the 3D scan ensuring that the centre of the leading edge was aligned with $y = 0$. The result of the pre-alignment and rotation using GOM Inspect can be seen for the Phase 2 erosion scan on the CAD cylinder in Figure 3.4.

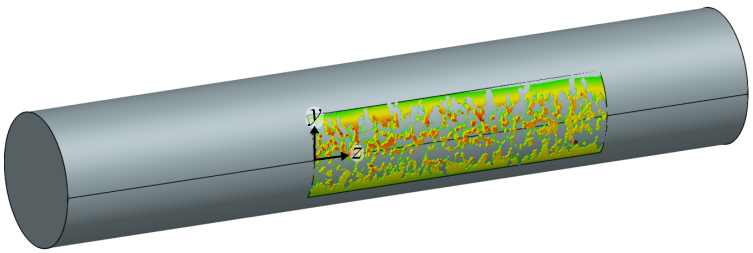

Figure 3.4: Alignment of Phase 2 erosion scan on cylinder, facilitating a surface comparison.

3.3.2.2 Surface analysis: 3D roughness

After alignment, a surface comparison was performed on the 3D scan, resulting in a 3D surface map between the 3D scans and the cylinder as can be seen in Figure 3.5. The three-dimensional roughness is translated to deviations as normal surface distance, where the colour shows how much the 3D scan deviates from the CAD cylinder. For a red colour, the 3D scan bulges out, while for the blue colour the scan surface is negative inwards compared to the CAD cylinder. Therefore negative values show a material loss, with depths going inward. A green colour shows a small difference between the 3D scan and the CAD cylinder.

From the state of the colours, it can be seen that the Phase 1 and Phase 3 erosion scans are aligned correctly with the CAD cylinder. The colours are green in the parts furthest away from the centre line (going up and down from $y = 0\,\text{mm}$), where the erosion is least heavy. For Phase 3 erosion, it is clear that the centre region shows heaviest erosion, with blue colours showing valleys deeper than 1 mm.

The Phase 2 erosion scan shows a misalignment of the 3D scan, as substantial orange and red parts are visible. These colours would mean that material bulges out, while for leading edge erosion this is cannot be true. Therefore it is considered that a misalignment occurred. A reason for misalignment could be the manufacturing tolerances of the RET specimens, resulting in a different radius compared to the CAD cylinder, or an inaccurate GOM Inspect best-fit estimation. In Section 3.3.2.3 a method is explained how to cope with this misalignment.

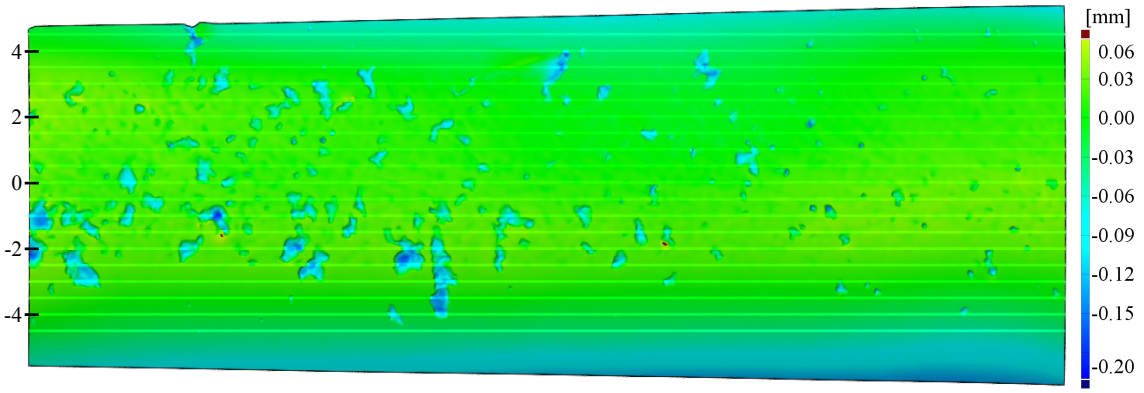

a Phase 1

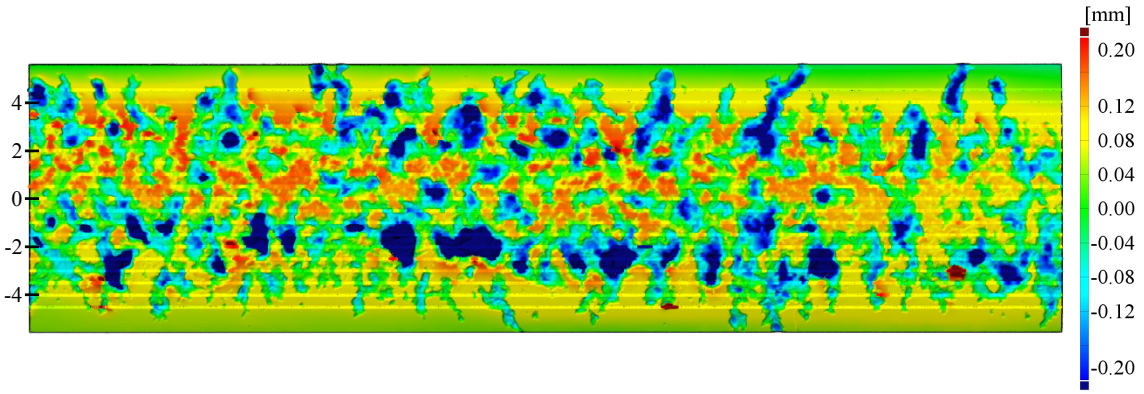

b Phase 2

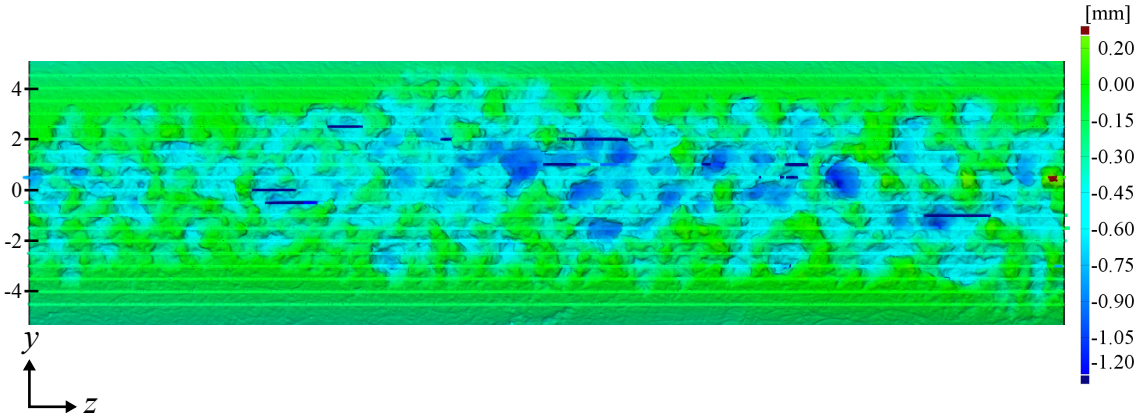

c Phase 3

Figure 3.5: Surface inspection of Phase [1,2,3] erosion with nineteen sections for extracted 2D curves highlighted (spacing between sections is 0.5 mm). For each erosion phase different colour scales for depth were used.

3.3.2.3 Sectional analysis: 2D roughness

To perform a roughness analysis on a 3D surface, 2D roughness curves are required enabling calculations to obtain certain roughness characteristics and statistics. Therefore, from the 3D surface comparison, 2D roughness curves need to be extracted. In GOM Inspect nineteen sections were created in the

y-plane onto the 3D scan, with distances of 0.5 mm in between (going from $y = -4.5$ mm to $y = 4.5$ mm). Now using the 'I-inspect' tool, the values from the surface analysis were extracted resulting in the 2D roughness curves. Locations of roughness curves are highlighted in Figure 3.5, and the roughness curves itself are shown for $y = 0$ mm in Figure 3.6.

Aforementioned, the alignment of the 3D scans deviates slightly for Phase 2 erosion, resulting in inaccurate 2D roughness curves. It is assumed that for each 2D roughness curve, there is still a peak that reaches the original uneroded surface. With finding the third highest peak, the roughness curves were adjusted so that this third highest peak is located at zero normal surface distance. The third highest peak was taken to filter out peaks that might correspond to peaks with positive normal surface distance (bulging out of the surface). This misalignment adjustment is also included in the 2D roughness curves as shown in Figure 3.6.

It can be seen in Figure 3.6, that for Phase 1 and 2 erosion, the normal surface depths are less than 400 μm. Therefore it is concluded that erosion for Phase 1 and 2 only perturbs into the coating, as explained in Section 3.1.1. For Phase 3 erosion, the depths of the valleys are considerably higher than 400 μm, and therefore this erosion phase is located on the random mass loss level where also glass-layers are affected. These results validate the selection of RET specimens and their locations on the mass loss curve as shown in Figure 3.2.

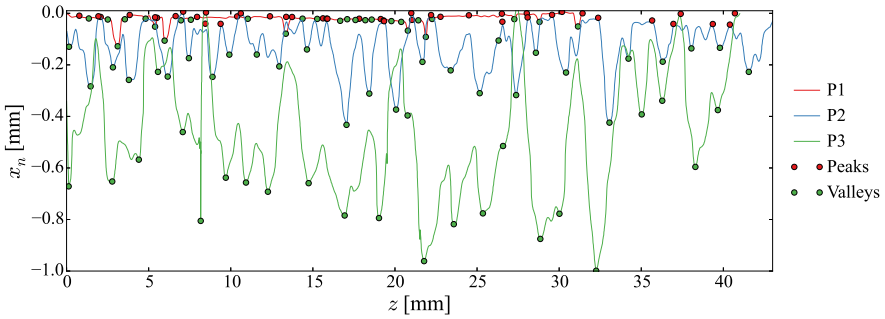

Figure 3.6: 2D roughness curves with peaks and valleys indicated for Phase [1,2,3] erosion, at $y = 0$ mm.

3.3.3 Surface roughness parameters

For each 2D roughness curve, surface roughness parameters were extracted describing the roughness curves in terms of characteristics and statistics. As the parameters were extracted for each individual 2D roughness curve, the parameters were known for each y location. This made it possible to analyse the influence of location from the leading edge to the roughness parameters. Also there could be determined what the influence of the erosion phases is to the parameters, making it possible to conclude which parameters are critical and should be taken into account when modelling erosion patterns.

The roughness parameters were extracted following a surface roughness analysis method as described by Bhusan (2001) [21], leading to amplitude and spatial parameters as well as a statistical analysis. This surface roughness analysis considers roughness curves consisting of peaks with varying heights and spacing in between the peaks, as well as valleys with varying depths and spacing. A peak on the curve is defined as a point higher than two neighbouring points and greater then a threshold value, whereas a valley is defined as a point lower than two neighbouring points and lower than a threshold value. A threshold value for finding peaks and valleys is required to reduce the effect of noise and ensure distinct peaks and valleys are found. Also a peak on a 2D roughness curve is a cross-section of an asperity in the 3D surface map, in the same way a valley (2D) is a cross-section of a summit.

In the case of leading edge erosion the valleys are of higher interest than the peaks, as material in early erosion phases is chipped off and valleys appear. Resultantly, a 2D surface roughness curve is described by a certain amount of valleys with varying widths, depths and distances. Therefore, as an extension to the surface roughness analysis method as described by Bhusan (2001) [21], is the

extraction of Gaussian valley fit parameters. These parameters will describe the varying width of valleys.

Finally a statistical analysis resulted in a surface height distribution. Here the Gaussian probability density functions of the 2D roughness curves were investigated, leading to the skewness and kurtosis, describing the surface height distribution.

3.3.3.1 Amplitude parameters

Mean μ and variance σ^2 are calculated following (3.1) and (3.2), where the standard deviation σ follows by taking the square root from the variance. In Figure 3.7a Phase 1 and Phase 2 erosion show a relatively constant area of mean values along y, where the values smooth out to zero at the boundaries. Phase 3 erosion clearly shows maximum mean values at the leading edge ($y = 0\,\text{mm}$) and gradually smooths out to zero at the boundaries. The standard deviations in Figure 3.7b for the different roughness curves show a similar trend as the mean values.

$$\mu = \frac{1}{L}\int_0^L (x)\,dz \tag{3.1}$$

$$\sigma^2 = \frac{1}{L}\int_0^L (x-\mu)^2\,dz \tag{3.2}$$

The peaks and valleys were found for the 2D roughness curves, based on certain threshold values for the normal surface height and distance in z-direction. For each erosion phase these thresholds are stated in Table 3.1. The valley depth and distance thresholds wee set lower for Phase 1 than for Phase 2 and 3 erosion, as the erosion depth lower than $x_n = 100\,\mu\text{m}$ is only a fraction of the depth compared to Phase 2 and 3 erosion. The found peaks and valleys for $y = 0\,\text{mm}$ are also shown in Figure 3.6, indicating that with these thresholds the distinct peaks and valleys were found.

Table 3.1: Thresholds for finding peaks and valleys of RET specimens.

	Peaks		Valleys	
Phase	x_n [μm]	z [mm]	x_n [μm]	z [mm]
1	850	2	20	0.5
2	850	2	50	2
3	850	2	50	2

Five extreme value parameters were computed. First the average valley depth $x_{n,\mu}$ was computed, as can be seen in Figure 3.7c. This parameter is significantly different between the erosion phases and also shows a constant region of high valley depth in the central region ($-2.5 < y < 2.5$), while smoothing out towards the boundaries. Secondly the distance between the highest peak and the lowest valley $x_{n,max-min}$ is shown in Figure 3.7d. This parameter is less important for describing erosion, as the highest peak in theory should be around zero resulting in similar results to the lowest valley depth parameter. Subsequently the lowest valley depth $x_{n,min}$ is shown in Figure 3.7e, where the deepest valleys again can be found in the central region. The last two extreme value descriptors are the average valley to mean height $x_{n,min-\mu}$ in Figure 3.7f and the distance between the average of the five deepest valleys and the mean $x_{n,5min-\mu}$ in Figure 3.7g. Though also showing a central region with deepest valleys, parameters that perform comparisons to the mean value are of less importance, as erosion will be described from the zero line $x_n = 0\,\text{mm}$. The main focus therefore is on comparisons of valley depth to the zero line, which is the average valley depth parameter $x_{n,\mu}$.

Furthermore, the integral below the roughness curve was computed, by means of the trapezoidal rule. This resulted in the area of material loss, dividing this by the total length along z the area material loss per millimetre A_n is computed, as shown in Figure 3.7h. This area per length should give the same

value as the mean value of the roughness curve μ, as when the mean value of the roughness curve is multiplied with its length, this in theory should give the same area. This is confirmed by Figures 3.7a and 3.7h, where the values are the same.

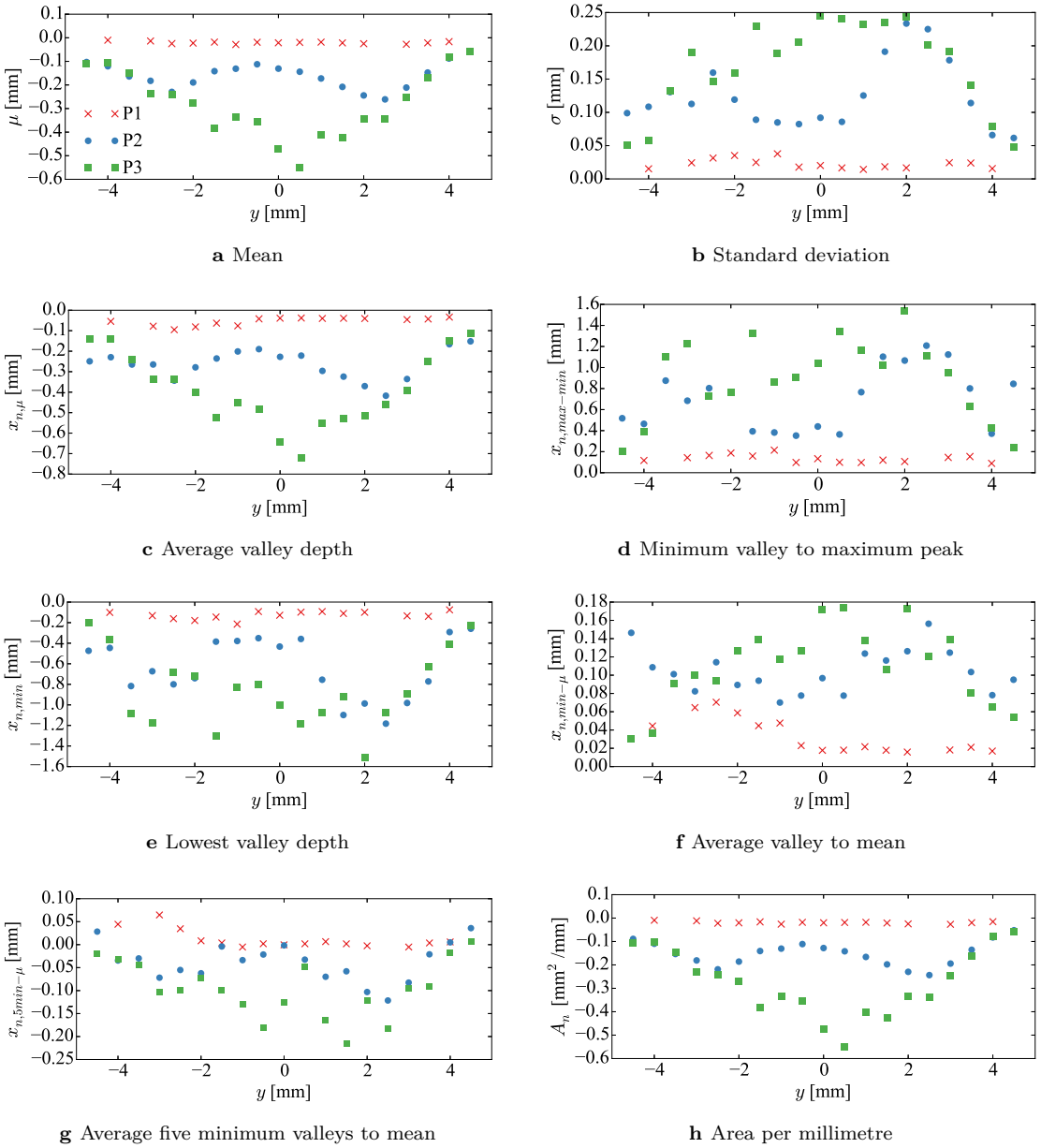

a Mean

b Standard deviation

c Average valley depth

d Minimum valley to maximum peak

e Lowest valley depth

f Average valley to mean

g Average five minimum valleys to mean

h Area per millimetre

Figure 3.7: Average roughness parameters and extreme value descriptors for Phase [1,2,3] erosion.

3.3.3.2 Spatial parameters

Four spatial parameters were computed, describing the valley density and the distance between valleys, as well as the mean of the profile slope and curvature. Spatial parameters valley density and distance were only computed for valleys and not for peaks, as the erosion roughness curves can be described in terms of valleys only, originating at the zero line $x_n = 0\,\text{mm}$.

The valley density per millimetre $n_{v/mm}$ of the 2D roughness curves was computed by taking the total number of found valleys and dividing this by total the length along z. Values for valley density are shown in Figure 3.8a. For Phase 2 and Phase 3 erosion, the valley density is similar compared to each other and shows a higher constant area in the central region ($-3.5 < y < 3.5$), with decreasing density towards the boundaries. For Phase 1 erosion, the peak in valley density is shifted towards positive y-direction. Phase 1 erosion has a higher density of found valleys, though with lower valley depths as for Phase 2 and 3 erosion.

Average valley distance z_μ was computed by finding each individual distance between two adjacent valleys and taking the average of these distances. The values should be the inverse of the valley density, as can be seen in Figure 3.8b, therefore also showing the same trend for the different erosion phases as for the valley density.

Profile gradient was calculated using the NUMPY GRADIENT algorithm, utilizing a second order accurate central difference scheme to compute $\left(\frac{\partial x}{\partial z}\right)$ in each data point and finally averaging the results for each roughness curve. Results are shown in Figure 3.8c. As the average gradient of each curve was computed, these values should be approximately zero, considering a roughness curve going up and down in an equal amount.The average profile curvature was computed using the GAUSSIAN FILTER 1D algorithm to compute $\left(-\frac{\partial^2 x}{\partial z^2}\right)$, as shown in Figure 3.8d.

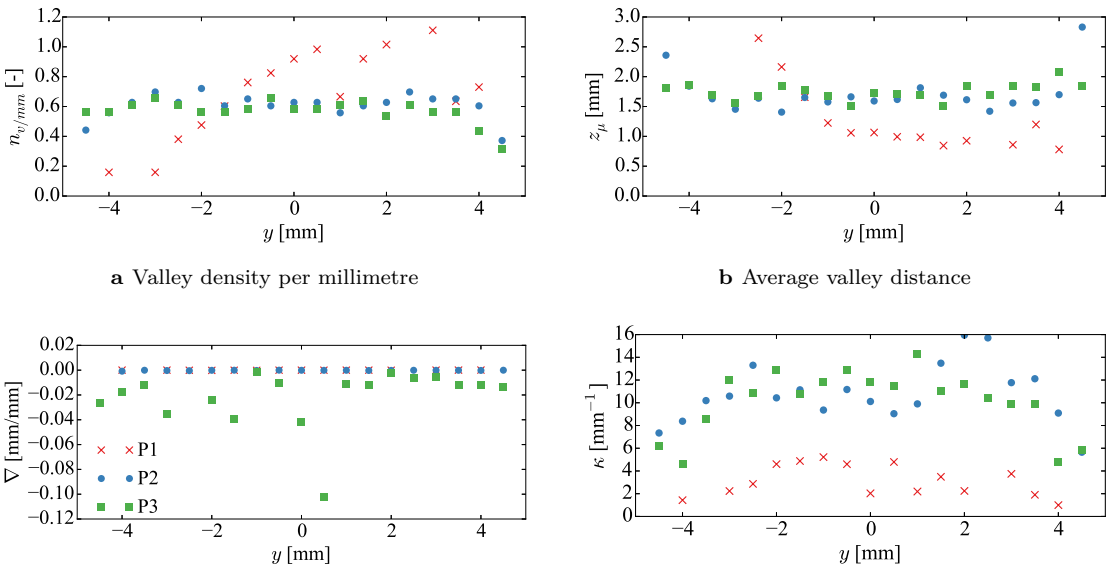

a Valley density per millimetre

b Average valley distance

c Average gradient

d Average curvature

Figure 3.8: Spatial parameters for Phase [1,2,3] erosion.

3.3.3.3 Gaussian valley parameters

It is assumed, that a leading edge erosion roughness curve can be described by many different valleys originating at zero, having certain valley widths, depths and distances. A wide valley in a 2D roughness curve, consisting of certain local minima within the wide valley, can be described by a certain amount of overlapping valleys with different depths and widths, where each individual valley depth matches the local minima. Taking the minimum value of overlapping valleys, should describe the erosion roughness curve. This is of high importance to model an erosion pattern, as described for the DLE erosion model in Section 6.1.

It is assumed that each valley in the 2D roughness curve follows the shape of a Gaussian function (pointing negatively downwards), as shown in (3.3). For each individual valley a Gaussian function was

fitted in the 2D roughness curves. The algorithm which was used to fit the Gaussian functions through the valleys is the SciPy Optimize Curve Fit tool, which uses a non-linear least square to fit a function (in this case a Gaussian function) through the valley data. Using this algorithm optimal values for the parameters a_G, b_G, c_G were found so that the sum of the squared residuals of $f_{Gaussian}(z, p_{opt}) - x_n$ is minimized. The algorithm utilizes initial guesses for a_G, b_G, c_G parameters as described below.

$$f_{Gaussian}(z) = a_G \cdot e^{-\frac{(z-b_G)^2}{2c_G^2}} \tag{3.3}$$

In (3.3) a_G is the height of the Gaussian fit, which is initially set as the valley depth $x_{n,v}$. b_G is the position of the centre of the peak which is same as the valley location z_v. Finally c_G is the Gaussian function standard deviation which needed to be optimized, describing the width of the valley in terms of a standard deviation of the fit σ_v. The initial guess for c_G was taken from the range rule of thumb for estimating a standard deviation; by taking the maximum value minus the minimum value and dividing this by four. The maximum range value is the depth of the valley $x_{n,v}$, whereas the minimum value is zero (the curves originate at zero).

Table 3.2: Gaussian function parameters optimized to fit valleys.

Parameter	Initial guess	Output
a_G	$x_{n,v}$	
b_G	z_v	
c_G	$\left\lvert \frac{x_{n,v}}{4} \right\rvert$	σ_v

The Gaussian fits in each valley are shown as the grey dotted curves in 3.9, located along $y = 0\,\text{mm}$ for Phase [1,2,3] erosion. This also shows that by taking the minimum values of the overlapping Gaussian fits (the minimum fits curve), the 2D roughness curve can be re-modelled. For Phase 1 and 2 erosion, the minimum fits curve matches well with the 2D erosion roughness curve. For Phase 3 erosion, peaks appear going to zero between $10 < z < 25$ for the minimum fit curve, caused by a too high threshold value for the individual valley distance. Still, the full depth of the valleys is reached, where erosion depth is considered the most critical parameter. Therefore these graphs show that fitting Gaussian functions in the valleys of the 2D roughness curves and taking the minimum values of the overlap, appears to be a an accurate method to model 2D erosion.

For each 2D roughness curve, the averaged Gaussian valley parameters (versus y-location) are shown in 3.10. The valley width is defined as the full width at half maximum (FWHM), and was calculated from the Gaussian fit standard deviation as shown in (3.4). Erosion Phase 2 and 3 show, similar to valley depths, that there is a clear central region between $-2.5 < y < 2.5$ of approximately constant highest valley width, while smoothing out to zero at the boundaries. For Phase 1 erosion, the widest valleys are located on the positive y-locations.

$$FWHM_v \approx 2.3548\sigma_v \tag{3.4}$$

With the individual valley widths and depths known, a point cloud was computed as shown in Figure 3.11. This point cloud shows differences between Phase 1 to Phase 3 erosion, going from shallow and wide valleys to deep and narrow valleys.

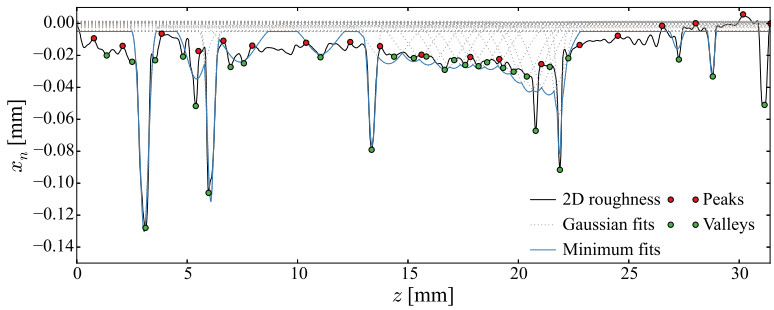

a Phase 1

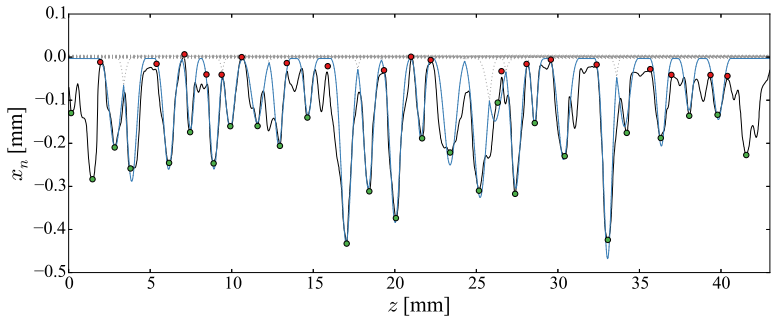

b Phase 2

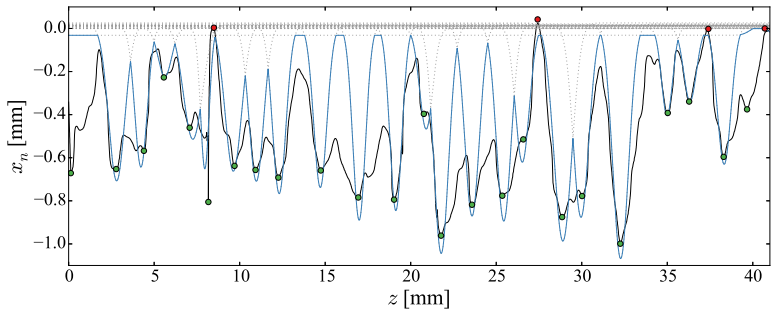

c Phase 3

Figure 3.9: 2D roughness curves and Gaussian fits for Phase [1,2,3] erosion, at $y = 0\,\text{mm}$.

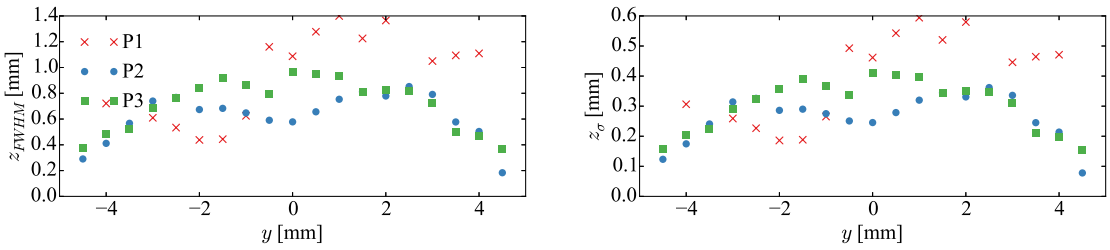

a Average of full width at half minimum fits

b Average of sigma Gaussian fits

Figure 3.10: Gaussian parameters for Phase [1,2,3] erosion.

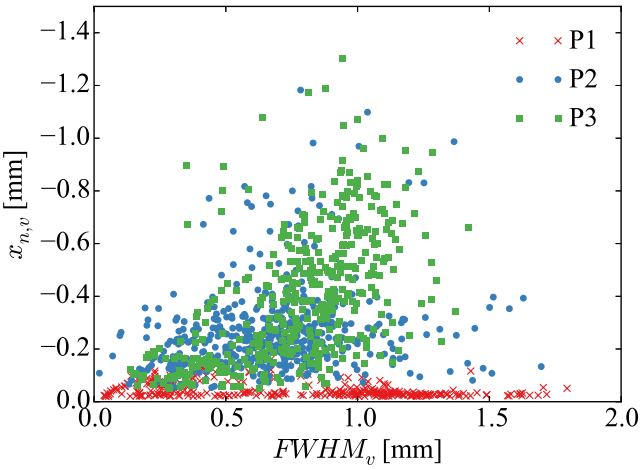

Figure 3.11: Point cloud of all valleys with associated depths and widths for Phase [1,2,3] erosion.

3.3.3.4 Surface height distribution parameters

A statistical analysis was performed on the shape of the 2D roughness curves, investigating its probability density functions and corresponding surface height distribution parameters.

An eroding surface is formed by a cumulative process, where the final shape is the cumulative result of a extensive amount of random local events, namely impacting rain droplets. This cumulative process is governed by a Gaussian form, as defined by the central limit theorem of statistical theory [21]. Because of this, the surface height distribution of an erosion roughness curve will most likely be of a Gaussian form.

The surface height distribution is represented as a probability density function (PDF) P and was estimated using the SciPy Stats Gaussian KDE algorithm. This algorithm performs a kernel density estimation using Gaussian kernels. Also the surface height distribution parameters skewness and kurtosis were computed, following the analytical expressions as stated in (3.5) and (3.6).

$$Sk = \frac{1}{\sigma^3 L} \int_0^L (x-\mu)^3 \, dz \tag{3.5}$$

$$K = \frac{1}{\sigma^4 L} \int_0^L (x-\mu)^4 \, dz \tag{3.6}$$

Kurtosis and skewness have an effect on the shape of the PDF and the shape of the roughness curve, schematically shown in Figure 3.12. Skewness describes the degree of symmetry of the PDF, whereas kurtosis describes the peakedness.

A perfect Gaussian distribution has zero skewness and a kurtosis value of three, resulting in an equal number of local values above and below the mean value. Negative skewness results in a larger amount of local values above the mean compared to the Gaussian, resulting in a roughness curve with narrow valleys as is expected for the shape of an early erosion phase. Positive skewness gives a larger amount of local values below the mean compared to the Gaussian, resulting in a roughness curve with wider valleys and narrow peaks.

High kurtosis results in a peaked PDF, with a high amount of values close to the mean value. Low kurtosis on the other hand results in a blunt PDF, with local values more uniform distributed.

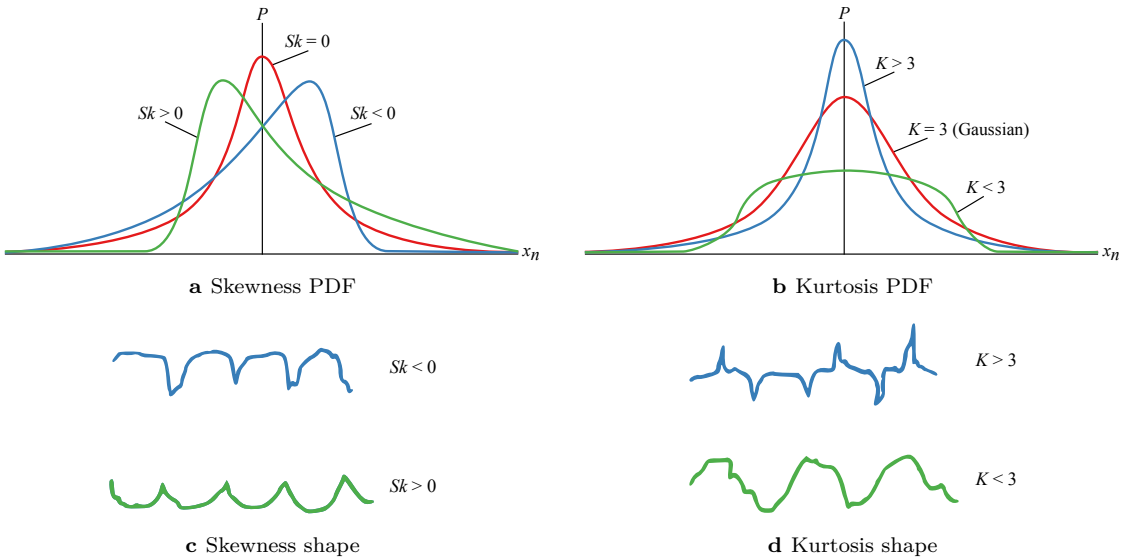

Figure 3.12: Probability density functions for random distributions, with distinct skewness and kurtosis values, together with a visualisation of impact to roughness curve shapes.

The computed probability density functions for the three erosion phases are shown in Figure 3.13. These are only shown for the 2D roughness curves located towards positive y-direction, to increase the distinctness. It is assumed that the PDF will look similar towards negative y-direction, due to symmetry of the RET specimens. Kurtosis and skewness were found for all y-locations, and are shown in Figure 3.14.

In Figure 3.13 the shapes of the PDFs are not completely smooth and sometimes show multiple peaks, though a trend in shapes is recognisable. For Phase 1 erosion a clear peak is located around -0.03 mm, matching with the arithmetic average values as shown in Figure 3.7a. For Phase 2 and Phase 3 erosion, the peaks (and therefore the average) shifts to higher negative values, except for $y = 4$ mm and 4.5 mm, where the high peak remains close to zero as erosion depth decreases moving away from the leading edge.

For all three erosion phases, the shape of the PDFs show negative skewness, with its main peak located closer to zero. This would result in a larger amount of local values above the mean compared to the Gaussian, resulting in a roughness curve shape with narrow valleys as seen in Figures 3.9 and 3.12c. This is confirmed by the computed negative skewness values shown in Figure 3.14a.

The PDFs in Figure 3.13 show less distinct kurtosis shapes. Computed kurtosis values are also changing in Figure 3.14b, with values below and above three, showing no clear trend in kurtosis between different erosion phases and distances from the leading edge.

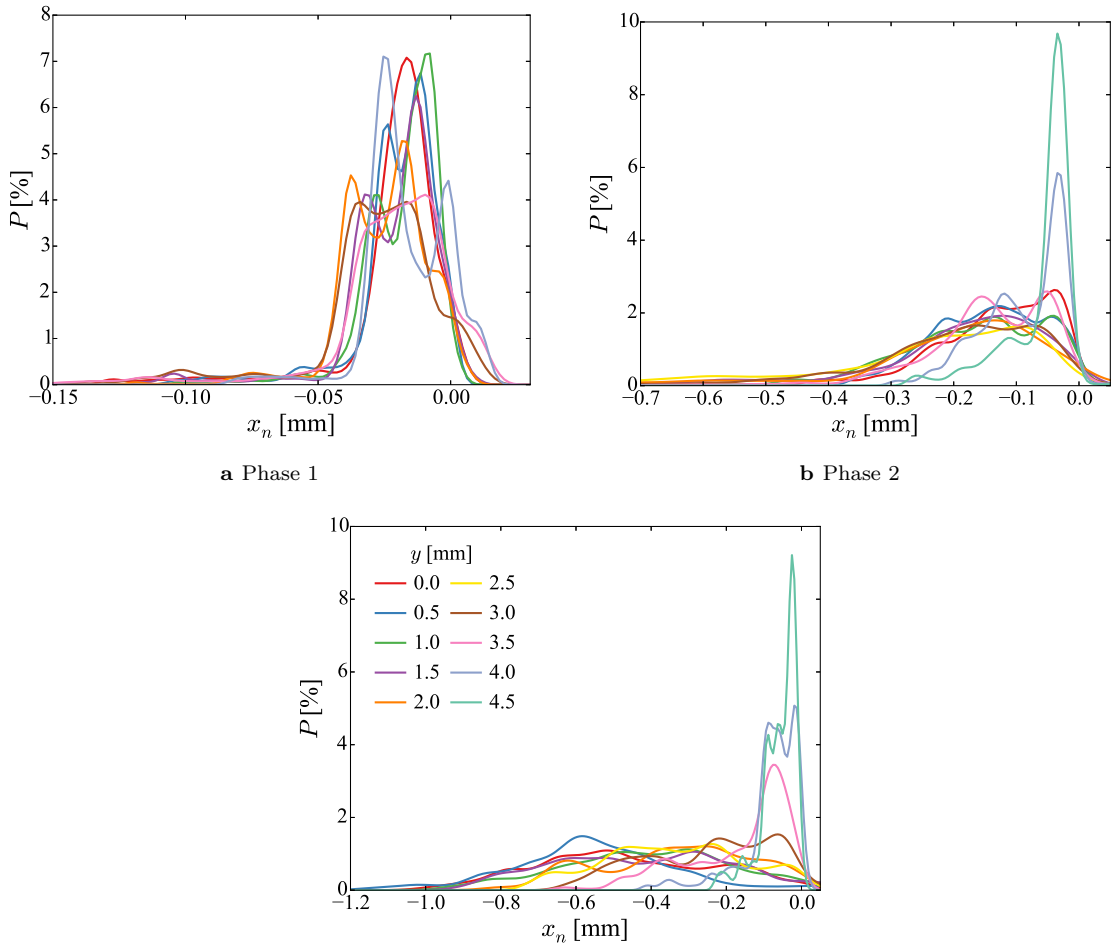

a Phase 1

b Phase 2

c Phase 3

Figure 3.13: Kernel density estimations for Phase [1,2,3] erosion, between $y = 0\,\text{mm}$ and $y = 4.5\,\text{mm}$.

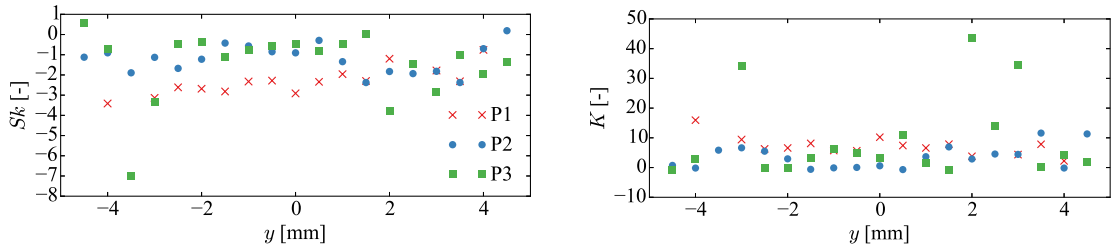

a Skewness

b Kurtosis

Figure 3.14: Surface height distribution parameters for Phase [1,2,3] erosion.

3.4 Leading-edge erosion coverage

The final part of characterizing the erosion, is to determine its coverage on the RET specimens and construct a method how this coverage on an RET specimen can be transferred to the leading edge of an airfoil.

At first, to give an approximation of the erosion coverage at the RET specimens, its statistical parameters were analysed. Though most parameters show a constant centre region and smoothing towards the boundaries, only the average valley depth parameter was considered to define the constant and smoothing zones. This is because erosion depth is assumed to be the most critical factor having an influence on the aerodynamics. Now, for each erosion phase, the constant and smoothing zones could be estimated, as shown in Figure 3.15a. For Phase 1 and 2 erosion, the constant area is set between $-2.5 < y < 2.5\,\text{mm}$, and smooths out to zero between $-2.5 < y < -4.5\,\text{mm}$ and $2.5 < y < 4.5\,\text{mm}$. Phase 3 erosion is set to constant between $-2.0 < y < 2.0\,\text{mm}$, and smooths out to zero between $-2.0 < y < -4.5\,\text{mm}$ and $2.0 < y < 4.5\,\text{mm}$.

The method to transfer this coverage to the leading edge of an airfoil, is based upon the inflow angles of rain droplets at the specific y-locations. Due to high velocity of the RET apparatus, it is assumed that the rain droplets are moving in x-direction. The rotational velocity of the RET specimens is significantly high than the velocity of falling droplets. This allows neglecting the initial droplet velocity and assuming the droplets move in a straight line in x-direction compared to the RET specimen, as shown in Figure 3.15b.

At the y-locations where the constant and smoothed areas were determined based upon the average valley depth $x_{n,\mu}$, the inflow angles of rain droplets were be computed on the RET specimens. These angles, now depending on the geometry of the RET specimens, are shown in Figure 3.15b, where β is the inflow angle defining the constant area and γ defines the smoothed area. β and γ for Phase [1,2,3] erosion are shown in Table 3.3. For each erosion phase, this method results in an angle of $\gamma = 60\,^\circ$ where the erosion stops.

When modelling erosion coverage on the leading edge of an airfoil, as described in Section 6.2.1, the last step is transferring the coverage of the RET specimens to the airfoil. This is done by finding the same angles β and γ on the airfoil leading edge. It should be taken into account that the angles (and therefore coverage location) on an airfoil also depend on the airfoil angle of attack. Assuming rain droplets hit the airfoil straight in x-direction, the impact angles depend both on angle of attack of the airfoil and the geometric angle of airfoil surface.

Assuming that the rain droplets will also hit the airfoil in a straight line is a conservative approach. In case the rain droplets would follow the flow streamlines along the airfoil, the stagnation point would be shifted further towards the pressure side. Erosion coverage then initiates further down on pressure side, where the influence of erosion is expected to be less. Therefore assuming the rain droplets impact the airfoil straight in x-direction, will result in erosion initiating close to the leading edge (depending on the angle of attack), closer to suction side and having a higher impact on the aerodynamic performance.

Table 3.3: Erosion coverage angles β and γ for Phase [1,2,3] erosion

Phase	β [°]	γ [°]
1	73.9	60.0
2	73.9	60.0
3	77.2	60.0

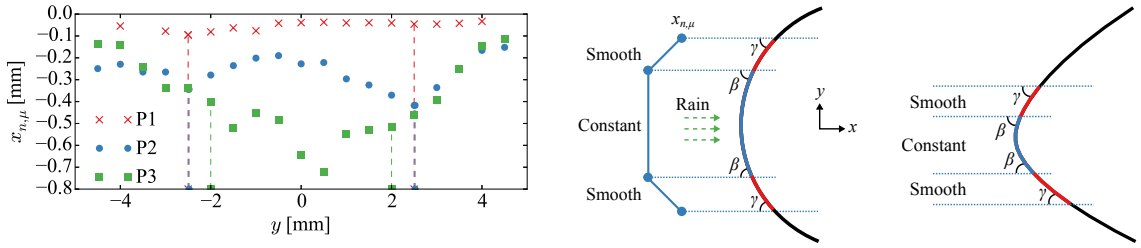

a Average valley depth **b** On RET specimen **c** Applied to airfoil LE

Figure 3.15: Constant and smoothed erosion coverage determination from RET specimens to airfoil LE.

3.5 Conclusion on erosion characterization

Three erosion phases were selected based upon the mass loss curve, where Phase 1 erosion is located immediately after incubation on the linear part of the mass loss curve. Phase 2 erosion is still located on the linear part, but has increased erosion depths. Phase 3 erosion simulates early break-through in the glass-layer, reaching the random level of mass loss.

Parameters were computed based upon extracted 2D roughness curves. It was concluded that the erosion pattern can be described by valleys originating at zero height, having certain valley depths, distances and widths. Therefore the erosion pattern is governed by three main parameters, namely the average valley depth parameter $x_{n,\mu}$, the average valley distance z_μ (or density) parameter and finally the average valley width parameter z_σ.

These three parameters are assumed to be constant in the constant region, where the constant region was defined by the average valley depth parameter. Subsequently for these three parameters, an average and standard deviation was computed for the combined 2D roughness curves in this constant zone. Combining the roughness curves in the constant zone, results to a higher amount of data to obtain more accurate results for the average and standard deviation of the three main roughness parameters. When modelling erosion, the average and standard deviations of the valley depth ($\mu_{x_{n,\mu}}$ and $\sigma_{x_{n,\mu}}$), distance (μ_{z_μ} and σ_{z_μ}) and width (μ_{z_σ} and σ_{z_σ}) parameters are taken as an input to the model, as explained in Section 6.1. These computed input parameters are shown in Table 3.4. Between the three erosion phases, only the average for valley depth is significantly different. For valley depth and distance, the average parameters appear to be constant between the erosion phases.

All other obtained roughness parameters can be used to validate the modelled erosion patterns to the RET specimens.

Table 3.4: Average and standard deviation of valley depth, distance and width parameters, for Phase [1,2,3] erosion, which will act as an input to the DLE erosion model.

	Valley depth		Valley distance		Valley width	
Phase	$\mu_{x_{n,\mu}}$ [mm]	$\sigma_{x_{n,\mu}}$ [mm]	μ_{z_μ} [mm]	σ_{z_μ} [mm]	μ_{z_σ} [mm]	σ_{z_σ} [mm]
1	-0.0503	0.0341	1.50	1.71	0.336	0.199
2	-0.284	0.173	1.60	0.476	0.301	0.135
3	-0.536	0.231	1.69	0.541	0.373	0.131

CHAPTER 4

Standardized roughness: zigzag tapes

The standardized roughness experiments in the LSWT were performed on an *LM18%* tip airfoil profile, as a measurement campaign which was performed before the start of this erosion study. At different chordwise locations zigzag tapes with varying thickness were placed. By placing a zigzag tape, the flow transitions at the location of the tape, leading to a decrease in aerodynamic performance. This method simulates the effects of leading edge erosion, and is applied by the industry for airfoil design to validate aerodynamic performance for roughened (eroded) leading edge surfaces.

Investigating what the result is of applying zigzag tapes at different chordwise locations, both on pressure and on suction side, will give an indication of where eroded surfaces at the leading edge have higher or lower impact. Also two different tapes with different thickness were applied, where it is expected that higher thickness penetrates deeper into the boundary layer, disturbing the flow to a higher extent and therefore resulting in a lower aerodynamic performance.

Zigzag tapes are added to the leading edge surface. In comparison to an eroded surface with negative shape modification, material is added leading to a positive shape modification. Therefore results of the quick erosion model in Chapter 5 and the detachable leading edge erosion model in Chapter 6 should be compared to the zigzag model, analysing if standardized roughness experiments which utilize zigzag tapes led to similar results.

An *LM18%* tip airfoil was used with pressure taps included to measure the lift. This is an LMWP internal airfoil, where coordinates and distribution of pressure taps are confidential. Chord length of the profile is 900 mm.

4.1 Configurations

Zigzag tape applied measured the dimensions as shown in Figure 4.1, where width is 6 mm, peak distance is 3 mm and angle is 70 °. Two different tape thicknesses were tested, subsequently of 0.205 mm and 0.4 mm thickness. Thinner zigzag tapes of 0.1 mm would have been available as well. The experiments of the zigzag study were performed before initiation of this erosion study, and due to time limitations for testing in the LSWT there was no possibility to investigate this thinner tape.

Though tape adds material to the surface, the tested tape thicknesses were compared to the erosion depths of the RET specimens in Table 3.4. This shows that for 0.205 mm zigzag tape the thickness compares with Phase 2 erosion at -0.284 mm. For 0.4 mm zigzag tape the thickness compares with Phase 3 erosion depth at -0.536 mm.

The first zigzag tape was applied at the location of the stagnation point at design angle of attack $\alpha_d = 7^\circ$ at $Re = 3 \cdot 10^6$. The stagnation point location followed from an LMWP EllypSys CFD analysis on the airfoil pressure distribution and finding the location of the pressure peak. Resultantly the stagnation point was found to be at $x = 1.03\,\%$c on the pressure side. At the stagnation point it is expected that flow disturbance due to the tape will be least, where the flow is capable to survive disturbances due to the pressure peak.

Additional lines of zigzag tape were placed both towards pressure and suction side, at surface distance steps of 12 mm from tape centre to tape centre. This led to an analysis of experiments with zigzag tapes of 0.2 mm thickness with increasing zigzag coverage, 0.4 mm zigzag tapes with increasing coverage, and a series for increasing thickness by combining 0.2 mm and 0.4 mm thickness.

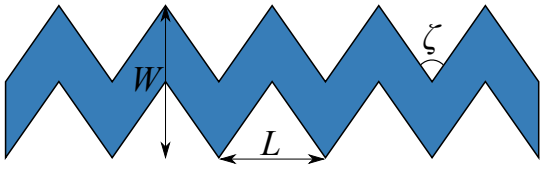

Figure 4.1: Zigzag tape with dimensions $W = 6\,\text{mm}$, $L_{zz} = 3\,\text{mm}$, $\zeta = 70\,°$.

4.1.1 Zigzag tape with 0.2 mm thickness

In Figure 4.2a the different configuration are shown for zigzag tapes with 0.2 mm thickness. First a zigzag tape was placed at the stagnation point (SP), followed by an addition tape towards suction side (1SS), then towards pressure side (1PS), and so on. Final configuration led to a tape at the stagnation point (SP), two towards suction side (2SS) and two towards pressure side (2PS). Therefore zigzag tape coverage initiates at the stagnation point, and final coverage goes up past the leading edge towards suction side (as well as further down towards pressure side).

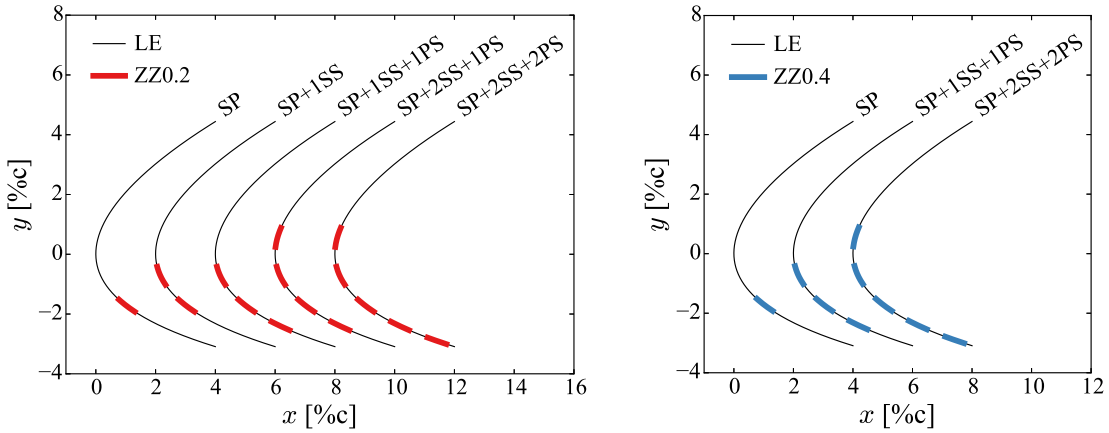

a Thickness 0.2mm

b Thickness 0.4mm

Figure 4.2: Configurations for 0.2 mm and 0.4 mm thick zigzag tapes on LE, shifts between LE $x = 2\,\%$c.

4.1.2 Zigzag tape with 0.4 mm thickness

In Figure 4.2b the different configuration are shown for zigzag tapes with 0.4 mm thickness. First a zigzag tape was placed at the stagnation point (SP), followed by an additional tape both towards suction side (1SS) and pressure side (1PS), then again both towards suction side (2SS) and pressure side (2PS).

4.1.3 Increasing thickness and coverage

For the increasing thickness analysis both the thickness and coverage increased, as shown in Figure 4.3. First an 0.2 mm tape was placed at the stagnation point, subsequently a tape was added towards both suction and pressure side. Then the stagnation point tape was replaced with an 0.4 mm, followed by

adding tapes again on both pressure and suction side. This until there were only 0.4 mm tapes, one at the stagnation point, two towards suction and two towards pressure side.

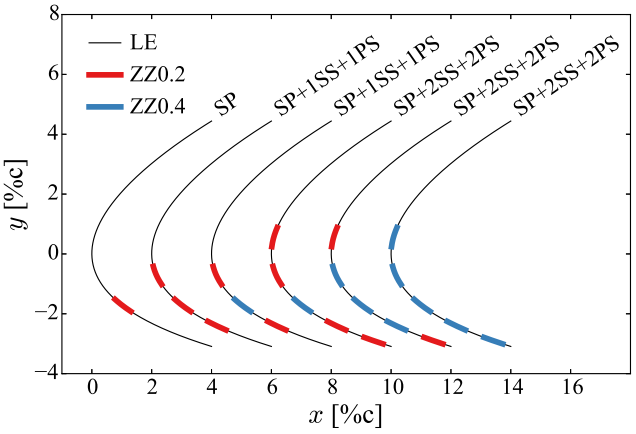

Figure 4.3: Configurations for increasing thickness zigzag tapes on LE, shifts between LE $x = 2\,\%$c.

4.2 Aerodynamic performance results

Experiments in the LSWT were performed at $Re = 3 \cdot 10^6$ and $Re = 6 \cdot 10^6$, to simulate operating conditions of a wind turbine blade. Lift and moment were computed from the airfoil pressure distribution as measured by the pressure taps. Drag was calculated from the velocity deficit measured by the wake rake. This led to lift, drag and moment polars. Also the performance degradation was computed at design angle of attack, for each configuration leading to a decrease in lift, increase in drag and decrease in lift over drag.

4.2.1 Zigzag tape with 0.2 mm thickness

Results are shown for configurations with zigzag tapes of 0.2 mm thickness, tested at $Re = 3 \cdot 10^6$ and $Re = 6 \cdot 10^6$.

4.2.1.1 $Re = 3 \cdot 10^6$

The lift curves in Figure 4.4a show similar results when comparing zigzag tape at the stagnation point to the clean case. After applying the first tape towards suction side, lift decreased above $\alpha = 6°$. Adding a tape towards the pressure side, led to a similar curve compared to having a tape towards suction side. Subsequently adding another tape towards suction side, decreased the lift already above $\alpha = 1°$ and also shifted the drag region to a lower angle of attack. Now adding another tape towards pressure side, led to a lift curve similar to the previous curve.

Drag results in Figure 4.4b show that in the positive angle of attack range, drag results are similar after applying a tape at the stagnation point compared to the clean curve. Drag increased when a tape was applied towards suction side, whereas it remained similar to the previous curve when a tape was applied towards pressure side. The largest step in drag increase occurred after applying the second tape towards suction side. Both from lift and drag results this indicated that applying a tape towards pressure side has a negligible impact on the positive lift (at $\alpha > 0°$), whereas applying tapes towards suction side led to detrimental effects to the positive lift. When the second tape towards suction was applied (so furthest away from the stagnation point and passed the leading edge), the detrimental effect was largest.

This is further confirmed by the lift over drag results in Figure 4.4d. Zigzag tape at the stagnation point gave a similar curve to the clean case, except a performance decrease in the region between $\alpha = -2°$ and 3° but still reaching the maximum lift over drag values as for the clean case. Applying a tape towards suction side led to a drop in lift over drag coefficient above $\alpha = 4°$, where applying a tape towards pressure side shows a similar curve as the previous. The largest drop in lift over drag occurred when applying a second tape towards suction side, starting at $\alpha = 0°$.

In Table 4.2 the relative performance loss is shown for lift, drag and lift over drag coefficient, at design angle of attack. Design angle of attack was assumed to be at maximum lift over drag coefficient for the clean case, therefore $\alpha_d = 6°$. Performance loss was negligible at design angle of attack when a tape was applied at the stagnation point. Performance loss was small when a tape was applied towards the suction side, though again at higher angles of attack a performance loss can be observed in Figure 4.5d. A large performance loss of 56 % resulted after applying a second tape towards suction side. This abrupt performance loss in lift over drag shows that application of zigzag tapes, as soon as they pass the leading edge, become too violent. Therefore zigzag tapes might not resemble an eroded surface, where it is expected that a gradual increase of erosion causes more gradual steps in performance loss.

Table 4.1: Lift and drag results at $\alpha_d = 7°$ for 0.2 mm zigzag tapes ($Re = 3 \cdot 10^6$).

Configuration[ZZ]	C_l-decrease [%]	C_d-increase [%]	C_l/C_d-decrease [%]
Clean	0	0	0
SP[0.2]	0.10	-0.24	-0.04
SP[0.2]+1SS[0.2]	2.82	1.74	3.47
SP[0.2]+1SS[0.2]+1PS[0.2]	3.06	-2.27	0.51
SP[0.2]+2SS[0.2]+1PS[0.2]	12.2	100.1	56.1
SP[0.2]+2SS[0.2]+2PS[0.2]	12.3	114.1	59.0

4.2.1.2 $Re = 6 \cdot 10^6$

At $Re = 6 \cdot 10^6$ the trend in performance loss is similar to $Re = 3 \cdot 10^6$. Only now the lift curves in Figure 4.5a show that after applying the first tape towards suction side, lift decreased at a lower angle of attack, which is at $\alpha = 4°$ (compared to $\alpha = 5°$ for $Re = 3 \cdot 10^6$). Adding another tape towards suction side, shifted the decrease in lift occurring at $\alpha = 0°$ (compared to $\alpha = 1°$ for $Re = 3 \cdot 10^6$). Therefore at higher Reynolds number, with zigzag tapes applied towards suction side, the lift gets affected at lower angles attack. As the boundary layer thickness decreases for higher angles of attack, while the thickness of zigzag tape remains the same, the tape perturbs deeper into the boundary layer. This probably causes early flow transition (a shift of transition location towards leading edge), at lower angles of attack compared to experiments at lower Reynolds number.

Drag results in Figure 4.5b show that at $\alpha > 5°$, drag was similar after applying a tape at the stagnation point compared to the clean curve. Drag increased when a tape was applied towards suction side, whereas it remained similar to the previous curve after a tape was applied towards pressure side. Also here the largest step in drag increase occurred after applying the second tape towards suction side.

The lift over drag results in Figure 4.5d show that a zigzag tape placed at the stagnation point gave similar results as for the clean case, only slightly decreased in the region between $\alpha = -2°$ and 5°. Applying a tape towards suction side led to a drop in lift over drag coefficient above $\alpha = 6°$, where applying a tape towards pressure side gave a similar curve as the previous. The largest drop in lift over drag occurred when applying a second tape towards suction side, starting at $\alpha = 1°$.

In Table 4.1 the relative performance loss is shown for lift, drag and lift over drag, at design angle of attack. Design angle of attack was assumed to be at maximum lift over drag coefficient for the clean case, therefore $\alpha_d = 6°$. This also shows that the performance loss is negligible when a tape is applied

at the stagnation point. Performance loss was relatively small after a tape was applied towards the suction side, though at higher angles of attack a performance loss can be observed in Figure 4.5d. Now a performance loss of 53 % occurred after a second tape was applied towards suction side.

Final relative performance loss at $Re = 6 \cdot 10^6$, with two zigzag tapes towards suction side and two zigzag tapes towards pressure side, was 54 %. This is less than for $Re = 3 \cdot 10^6$, where final performance loss was 59 %. This difference in relative performance loss for different Reynolds numbers probably results from the fact that at higher Reynolds numbers more energy is added to the flow, leading to higher lift coefficients. The absolute performance loss due to early transition might be more similar between different Reynolds numbers, leading to a different relative performance loss.

Table 4.2: Lift and drag results at $\alpha_d = 6°$ for 0.2 mm zigzag tapes ($Re = 6 \cdot 10^6$).

Configuration[ZZ]	C_l-decrease [%]	C_d-increase [%]	C_l/C_d-decrease [%]
Clean	0	0	0
SP[0.2]	0.08	-2.33	-1.68
SP[0.2]+1SS[0.2]	1.59	4.89	6.85
SP[0.2]+1SS[0.2]+1PS[0.2]	1.35	18.4	5.16
SP[0.2]+2SS[0.2]+1PS[0.2]	8.52	95.1	53.4
SP[0.2]+2SS[0.2]+2PS[0.2]	8.53	96.0	53.6

4.2.2 Zigzag tape with 0.4 mm width

Results are shown for configurations with zigzag tapes of 0.4 mm thickness, tested at $Re = 3 \cdot 10^6$ and $Re = 6 \cdot 10^6$.

4.2.2.1 $Re = 3 \cdot 10^6$

Again the lift curves in Figure 4.6a show similar results when comparing zigzag tape at the stagnation point to the clean case. When placing a tape both towards suction and pressure side, lift decreased above $\alpha = 4°$. For the 0.2 mm tape this case with a tape towards suction and pressure side, lift decreased above $\alpha = 6°$ as shown in Figure 4.4a. Adding an additional tape towards suction and pressure side, decreased the lift above $\alpha = 1°$ (which was also $\alpha = 1°$ for 0.2 mm tape). Therefore when tapes were applied close to the stagnation point, increasing the tape thickness had an effect as it shifted the initiation of lift decrease to a lower angle of attack. Tapes applied further up towards suction side (and pressure side) appeared to effect the flow more because of their location than because of their thickness. Also further away from the stagnation point (towards suction side), the thickness was less significant to aerodynamic performance as the flow was already disturbed (in the form of early flow transition) by the tape locate closer to the stagnation point.

Drag results in Figure 4.6b show that in the positive angle of attack range, drag for tape at the stagnation point was similar to the clean curve. Drag increased when a tape was applied towards suction and pressure side. It is assumed that the lift decrease and drag increase were caused by the tapes applied towards suction side, this because for 0.2 mm tape the application of tapes towards pressure side had no significant effect on the positive lift.

The lift over drag results are shown in Figure 4.6d. Zigzag tape at the stagnation point gave a similar curve to the clean case, only decreased in the region between $\alpha = -2°$ and 5° but still reaching the maximum lift over drag values as for the clean case. Placing a tape towards suction and pressure side led to a drop in lift over drag coefficient from $\alpha = 3°$. The largest drop in lift over drag occurred after applying a second tape towards suction and pressure side, starting at $\alpha = 0°$.

In Table 4.3 the relative performance loss is shown for lift, drag and lift over drag coefficient, at design angle of attack. Again design angle of attack was assumed to be at $\alpha_d = 7°$. Performance

loss was negligible at design angle of attack when a tape was applied at the stagnation point. A large performance loss of 32 % resulted when a tape was applied towards suction and pressure side. For 0.2 mm thickness with one tape toward suction and pressure side, no significant performance loss was measured at design angle of attack. This also confirms that increased tape thickness has an impact on the performance, in case the tapes are applied closest to the stagnation point. Final configuration, with two tapes towards suction and towards pressure side, led to a 62 % decrease in aerodynamic performance. This is slightly higher than for 0.2 mm thickness tapes, resulting in a loss of 59 %. At this distance from the stagnation point, different thicknesses did not result in large differences in performance loss.

Table 4.3: Lift and drag results at $\alpha_d = 7°$ for 0.4 mm zigzag tapes ($Re = 3 \cdot 10^6$).

Configuration[ZZ]	C_l-decrease [%]	C_d-increase [%]	C_l/C_d-decrease [%]
Clean	0	0	0
SP[0.4]	0.05	-1.39	-1.39
SP[0.4]+1SS[0.4]+1PS[0.4]	4.02	41.6	32.1
SP[0.4]+2SS[0.4]+2PS[0.4]	13.6	127.7	62.0

4.2.2.2 $Re = 6 \cdot 10^6$

The trend in performance loss is similar to $Re = 3 \cdot 10^6$. The lift curves in Figure 4.7a show that when applying the first tape towards suction and pressure side, lift decreased at a lower angle of attack, which is from $\alpha = 3°$ (compared to $\alpha = 4°$ for $Re = 3 \cdot 10^6$). Adding another tape towards suction side, shifted the decrease in lift occurring at $\alpha = 0°$ (compared to $\alpha = 1°$ for $Re = 3 \cdot 10^6$). As for the 0.2 mm tapes, for increasing Reynolds number the lift started to decrease from a lower angle of attack.

Drag results in Figure 4.7b show that at $\alpha > 5°$, having tape at the stagnation point is similar to the clean curve. Drag increased when a tape was applied towards suction and pressure side. The largest step in drag increase occurred after applying the second tape towards suction and pressure side.

The lift over drag results in Figure 4.7d show that zigzag tape at the stagnation point gave a similar curve to the clean case, slightly decreased in the region between $\alpha = -2°$ and 5°. Applying a tape towards suction side led to a drop in lift over drag coefficient above $\alpha = 6°$, where applying a tape towards pressure side shows a similar curve as the previous. The largest drop in lift over drag occurred when applying a second tape towards suction side, starting at $\alpha = 1°$.

Lift over drag results are shown in Figure 4.7d. Zigzag tape at the stagnation point gave a similar curve to the clean case, only decreased in the region between $\alpha = -2°$ and 10° but still reaches the maximum lift over drag values as for the clean case. Applying a tape towards suction and pressure side led to a drop in lift over drag coefficient from $\alpha = 2.5°$. The largest drop in lift over drag occurred when applying a second tape towards suction and pressure side, starting at $\alpha = -1°$. Compared to $Re = 3 \cdot 10^6$, increased Reynolds number shifted the angle of attack where the performance loss initiated with approximately one degree.

In Table 4.4 the relative performance loss is shown for lift, drag and lift over drag, at design angle of attack $\alpha_d = 6°$. The performance loss is negligible when a tape was applied at the stagnation point. When tape was applied towards suction and pressure side, performance loss was 48.1 %, which is higher than 32.1 % as measured for $Re = 3 \cdot 10^6$. For this tape coverage the thicker tape still leads to a higher relative performance loss at design angle of attack.

Final relative performance loss at $Re = 6 \cdot 10^6$, with two zigzag tapes towards suction side and two zigzag tapes towards pressure side, was 55 %. This is less than for $Re = 3 \cdot 10^6$, where final performance loss is 62 %. This difference in relative performance loss for different Reynolds numbers probably results from the fact that at higher Reynolds numbers more energy is added to the flow. Higher Reynolds number leads to early transition occurring at a lower angle of attack, though at angles of attack where the flow is fully transitioned (in this case also at the design angle of attack), the relative performance loss is less for higher Reynolds number.

Table 4.4: Lift and drag results at $\alpha_d = 6°$ for 0.4 mm zigzag tapes ($Re = 6 \cdot 10^6$).

Configuration[ZZ]	C_l-decrease [%]	C_d-increase [%]	C_l/C_d-decrease [%]
Clean	0	0	0
SP[0.4]	0.48	0.40	1.54
SP[0.4]+1SS[0.4]+1PS[0.4]	7.00	74.3	48.1
SP[0.4]+2SS[0.4]+2PS[0.4]	9.40	100.5	55.0

4.2.3 Increasing thickness

Results are shown for configurations with zigzag tapes of increasing thickness, tested at $Re = 3 \cdot 10^6$ and $Re = 6 \cdot 10^6$. This shows a combination of results between the 0.2 mm tape results, the 0.4 mm tape results, and new experiments with a combination of 0.2 mm and 0.4 mm tape.

4.2.3.1 $Re = 3 \cdot 10^6$

The lift polars in Figure 4.8a show again that results are similar between the clean case and the tape applied at the stagnation point. A decrease in lift occurred when a tape was applied towards suction and pressure side, mainly caused by the tape towards suction side. Increasing the tape thickness at the stagnation point gave no significant effect. Adding a second tape towards suction and pressure side decreased the lift, caused by the second tape towards suction side. After increasing the thickness of the first tapes towards suction and pressure side lift did not increase. Increasing the thickness of the second tapes towards suction and pressure side decreased the lift only in the maximum lift region. Therefore increasing the thickness of tapes after these were applied further down to suction side gave no significant impact on lift.

Drag in Figure 4.8b shows a similar trend. At the stagnation point the tape has no influence. Placing the first tapes towards suction and pressure sides increased the drag, but still reached clean drag values between $\alpha = 3°$ and $7°$. Increasing the thickness at the stagnation point also gave a drag increase between $\alpha = 3°$ and $7°$. Adding second tapes to suction and pressure sides increased the drag, where further increasing the thickness does not show a large drag increase.

The lift over drag results are shown in Figure 4.8d. After applying the first tapes the performance decreased above $\alpha = 6°$. Increasing the thickness at the stagnation point decreased the performance between $\alpha = 3°$ and $7°$, due to the increased drag in that region. Adding second tapes decreased the performance initiating at $\alpha = 0°$. Increasing thicknesses did not result in a significant difference as soon as two tapes towards suction and pressure side were applied.

In Table 4.5 the performance losses are shown at design angle of attack $\alpha_d = 7°$. This also revealed a significant performance loss of 39 % as soon as 0.4 mm tape was placed at the stagnation point with an 0.2 mm towards suction and pressure side. Additional tapes and increased thickness decreased the performance up to 62 %. This also shows that using zigzag tapes, no gradual performance loss can be established which would be expected for different levels of (early stage) erosion.

Table 4.5: Lift and drag results at $\alpha_d = 7°$ for increasing thickness ($Re = 3 \cdot 10^6$).

Configuration[ZZ]	C_l-decrease [%]	C_d-increase [%]	C_l/C_d-decrease [%]
Clean	0	0	0
SP[0.2]	0.10	-0.24	-0.04
SP[0.2]+1SS[0.2]+1PS[0.2]	3.06	-2.27	0.51
SP[0.4]+1SS[0.2]+1PS[0.2]	5.43	54.1	38.7
SP[0.4]+2SS[0.2]+2PS[0.2]	12.3	114.6	59.1
SP[0.4]+1SS[0.4]+1SS[0.2]+1PS[0.4]+1PS[0.2]	12.6	118.9	60.1
SP[0.4]+2SS[0.4]+2PS[0.4]	13.6	127.7	62.0

4.2.3.2 $Re = 6 \cdot 10^6$

At $Re = 6 \cdot 10^6$ the lift curves in Figure 4.9a show the same trend is observed as for $Re = 3 \cdot 10^6$. There is no influence to lift when a tape was applied at the stagnation point. A decrease occurred when the first tapes were applied towards suction and pressure side. Increasing the thickness at the stagnation point did not influence the lift. Subsequently adding second tapes towards suction and pressure side resulted in a lift decrease. Again increasing the thickness in the stagnation point did not decrease the lift. Increasing the thickness of the outer tapes decreased the lift in the maximum lift region.

For drag in Figure 4.9b placing tape at the stagnation point had no influence at $\alpha > 5°$. Placing the first tapes towards suction and pressure sides increased the drag along its full range in angle of attack. Increasing the thickness at the stagnation point gave an additional drag increase between $\alpha = 3°$ and 9°. Adding second tapes to suction and pressure sides increased the drag, where additional increase of thickness does not show a large drag increase.

The lift over drag results are shown in Figure 4.9d. After applying the first tapes the performance decreased above $\alpha = 5°$, which is one degree lower compared to $Re = 3 \cdot 10^6$. Increasing the thickness at the stagnation point shifted the angle where the performance loss initiated to $\alpha = 3°$, due to the increased drag. Adding second tapes decreased the performance initiating at $\alpha = 0°$. Increasing thicknesses of all tapes finally led to a performance loss initiated at $\alpha = -1°$.

In Table 4.6 the performance losses are stated. A 31 % decrease occurred when tape of 0.4 mm was applied at the stagnation point including a tape of 0.2 mm towards suction and pressure side. The relative performance loss for this configuration was less for $Re = 6 \cdot 10^6$ than for $Re = 3 \cdot 10^6$, where it was 39 %. Final configurations also show lower relative performance losses at $Re = 3 \cdot 10^6$ than for at $Re = 6 \cdot 10^6$.

Table 4.6: Lift and drag results at $\alpha_d = 6°$ for increasing thickness ($Re = 6 \cdot 10^6$).

Configuration[ZZ]	C_l-decrease [%]	C_d-increase [%]	C_l/C_d-decrease [%]
Clean	0	0	0
SP[0.2]	0.08	-2.33	-1.68
SP[0.2]+1SS[0.2]+1PS[0.2]	1.35	18.4	5.16
SP[0.4]+1SS[0.2]+1PS[0.2]	3.12	41.0	31.3
SP[0.4]+2SS[0.2]+2PS[0.2]	8.62	96.3	53.7
SP[0.4]+1SS[0.4]+1SS[0.2]+1PS[0.4]+1PS[0.2]	8.63	93.2	53.0
SP[0.4]+2SS[0.4]+2PS[0.4]	9.40	100.5	55.0

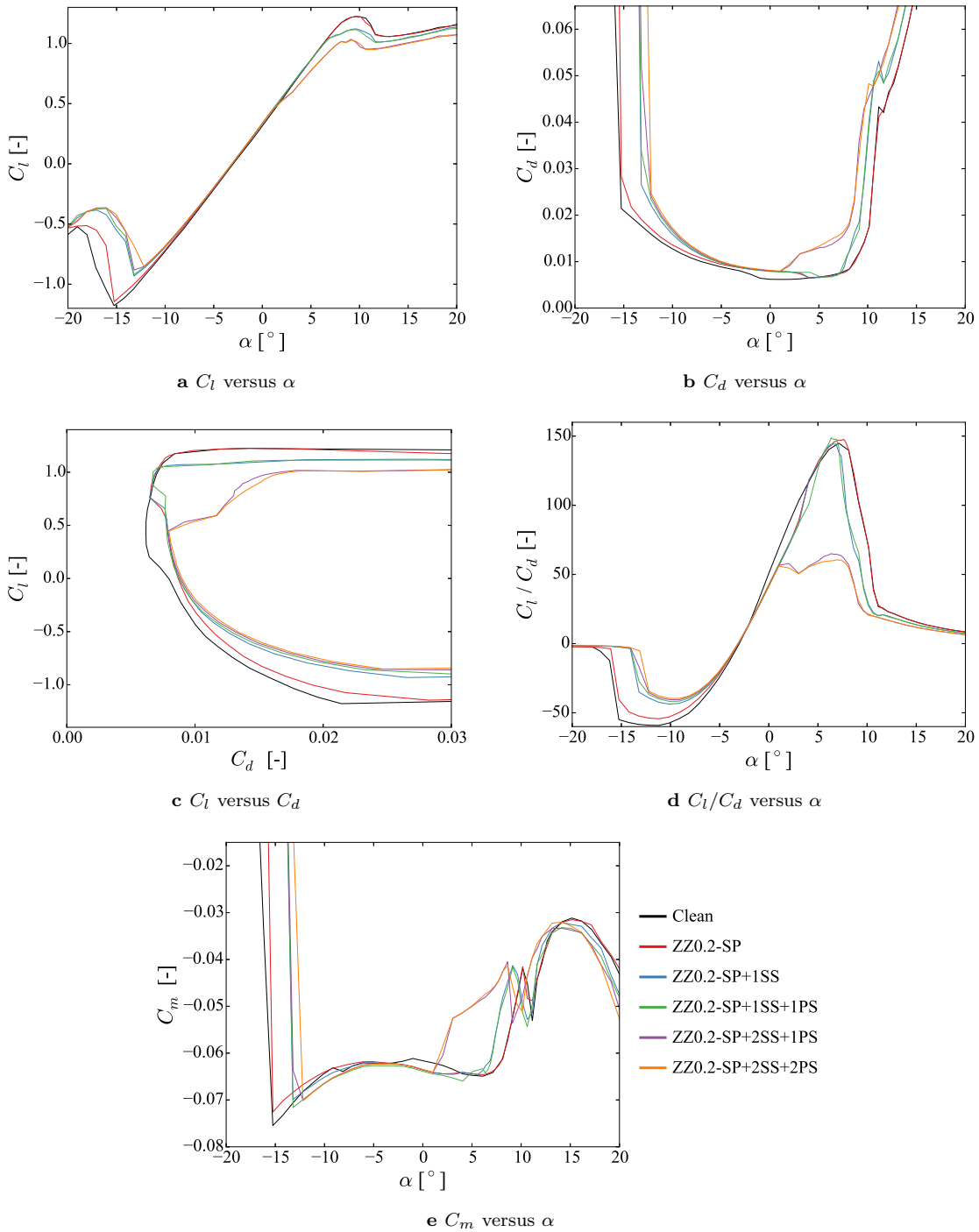

a C_l versus α

b C_d versus α

c C_l versus C_d

d C_l/C_d versus α

e C_m versus α

Figure 4.4: Aerodynamic performance for zigzag tape 0.2 mm width and $Re = 3 \cdot 10^6$.

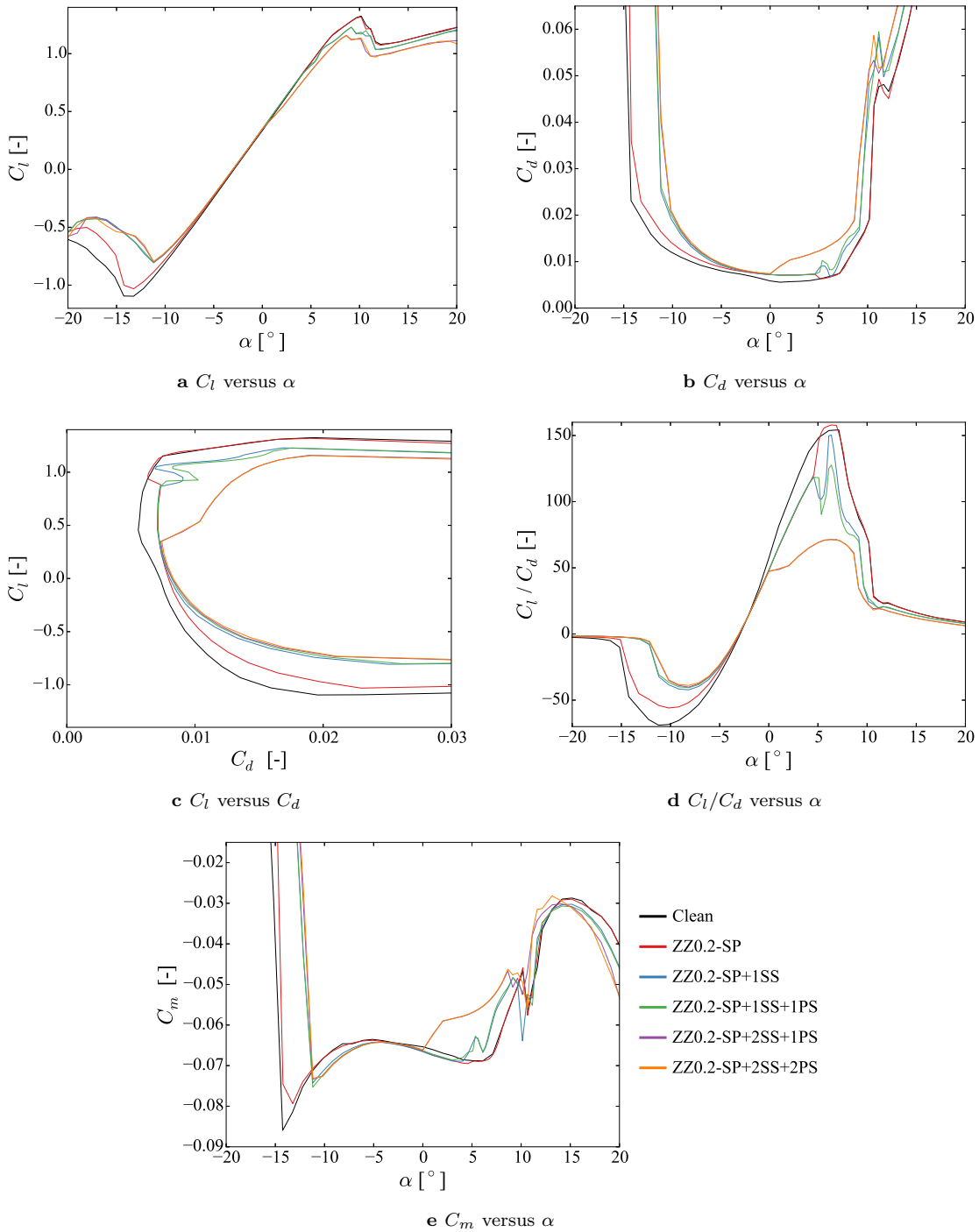

a C_l versus α

b C_d versus α

c C_l versus C_d

d C_l/C_d versus α

e C_m versus α

Figure 4.5: Aerodynamic performance for zigzag tape 0.2 mm width and $Re = 6 \cdot 10^6$.

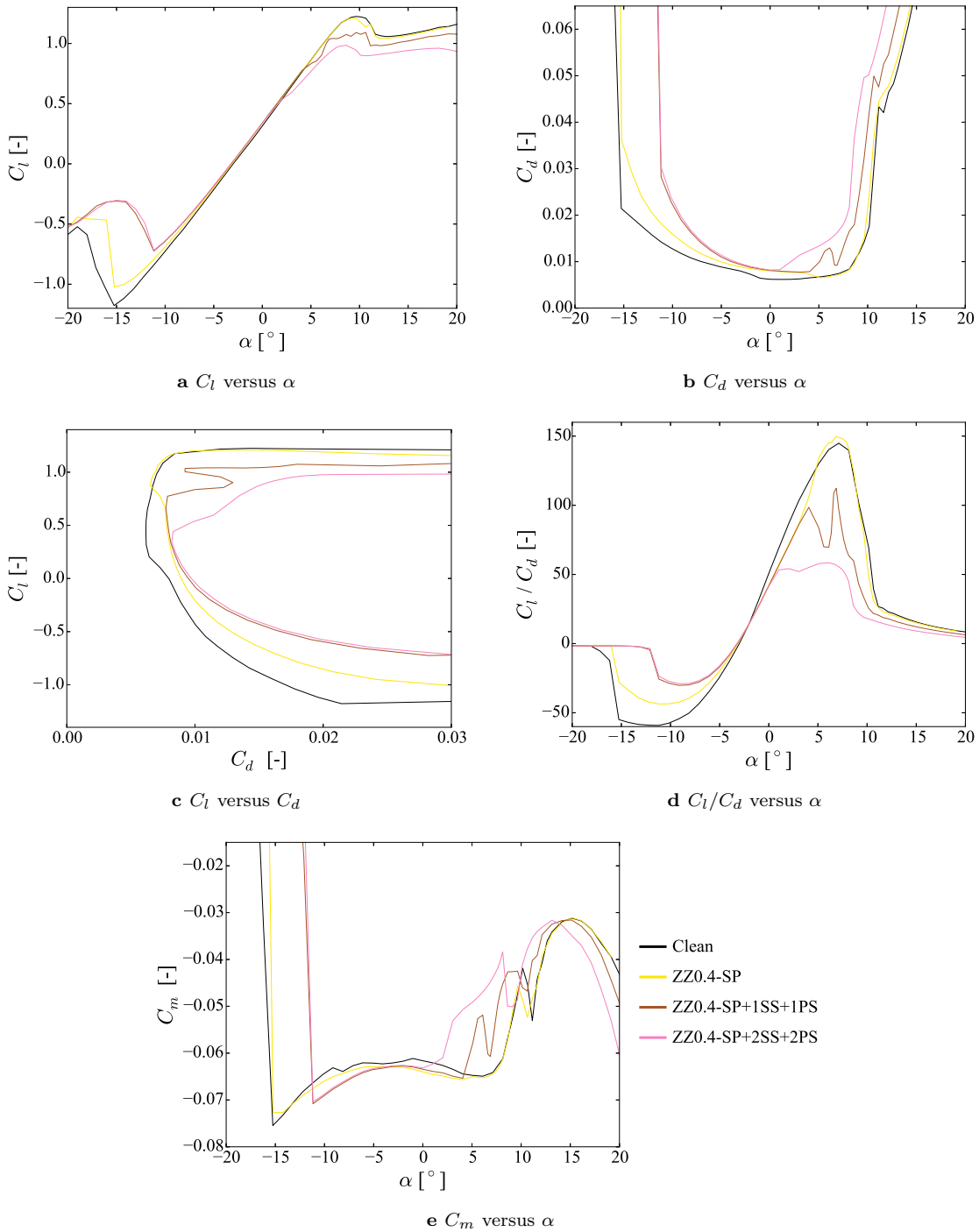

a C_l versus α

b C_d versus α

c C_l versus C_d

d C_l/C_d versus α

e C_m versus α

Figure 4.6: Aerodynamic performance for zigzag tape 0.4 mm width and $Re = 3 \cdot 10^6$.

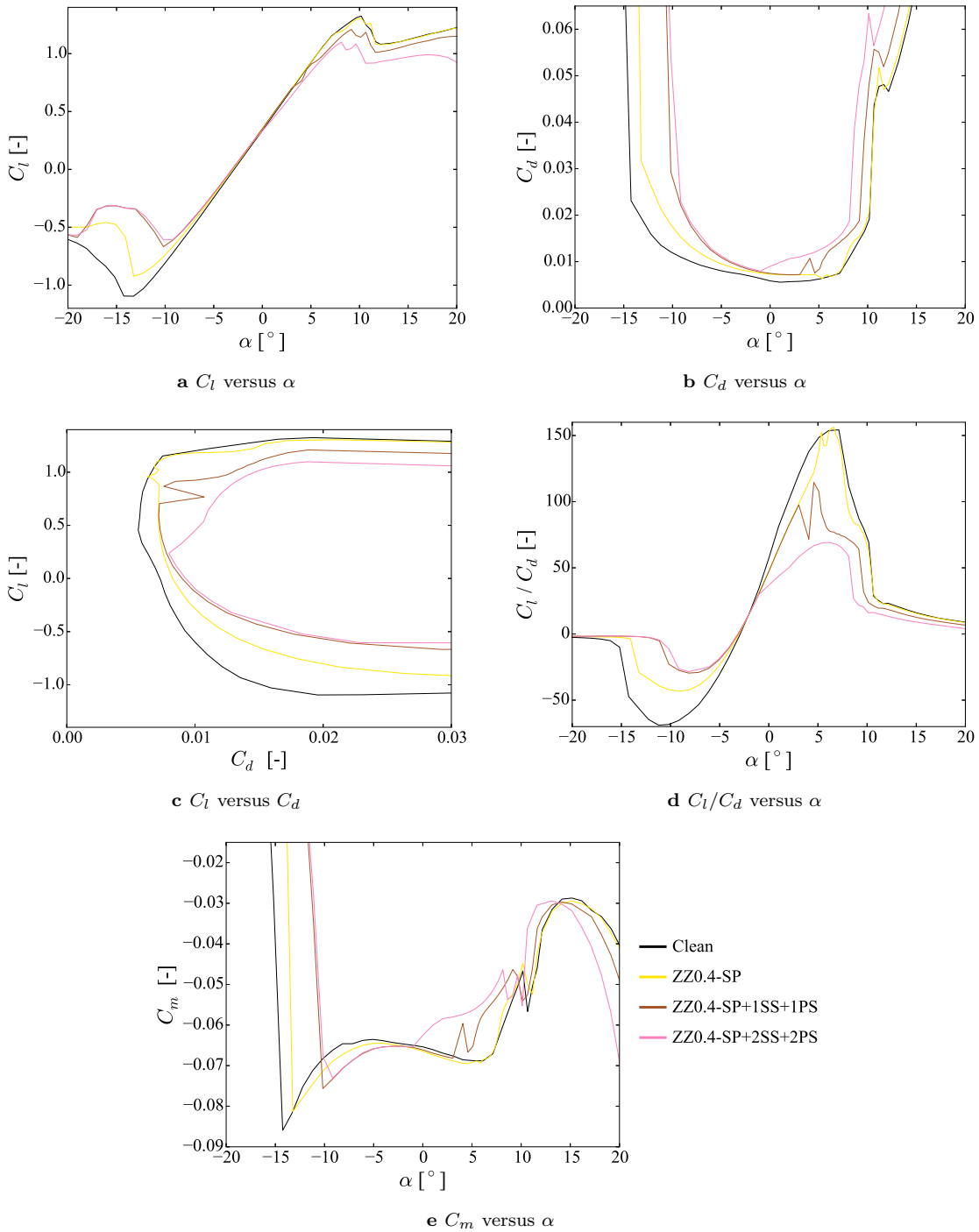

a C_l versus α

b C_d versus α

c C_l versus C_d

d C_l/C_d versus α

e C_m versus α

Figure 4.7: Aerodynamic performance for zigzag tape 0.4 mm width and $Re = 6 \cdot 10^6$.

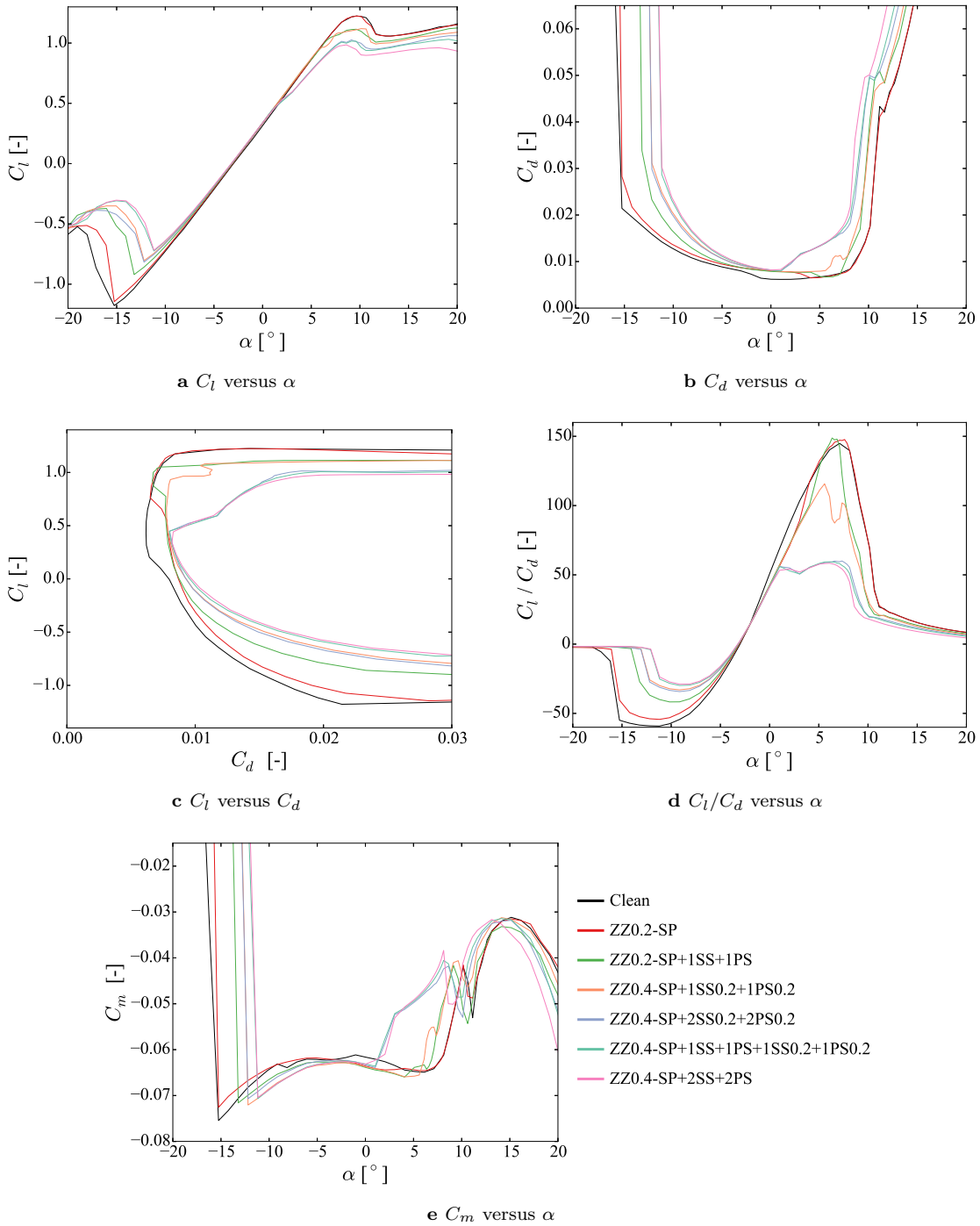

a C_l versus α

b C_d versus α

c C_l versus C_d

d C_l/C_d versus α

e C_m versus α

Figure 4.8: Aerodynamic performance for increasing erosion and $Re = 3 \cdot 10^6$.

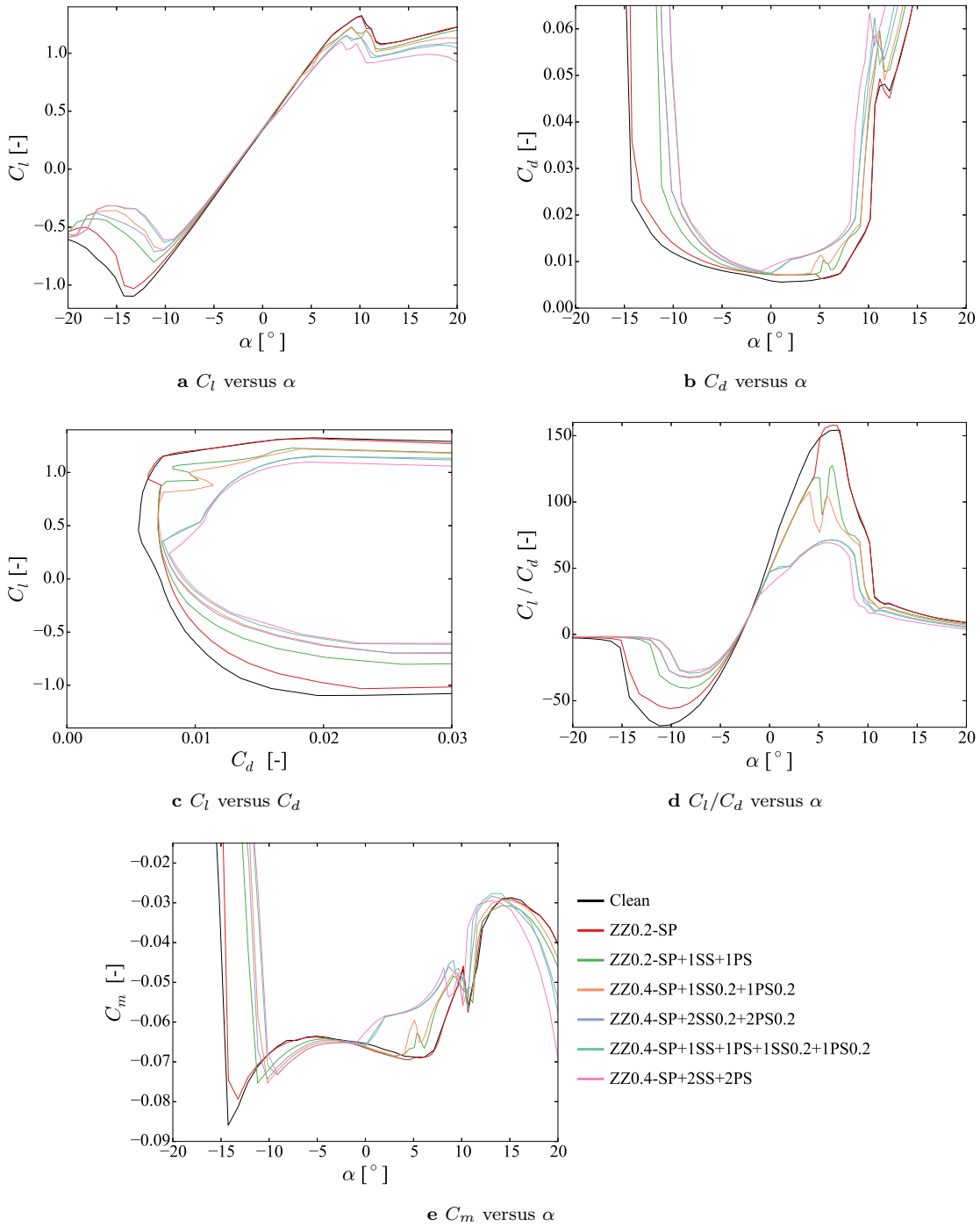

a C_l versus α

b C_d versus α

c C_l versus C_d

d C_l/C_d versus α

e C_m versus α

Figure 4.9: Aerodynamic performance for increasing erosion and $Re = 6 \cdot 10^6$.

CHAPTER 5

Quick erosion

The quick erosion model is an *LM18%* tip airfoil profile, having the same airfoil profile as the zigzag model in Chapter 4, and was build at House of Composites. Airfoil coordinates are not shown as the *LM18%* geometrical airfoil data is not available for public use. The material is a dense polyurethane foam material, which allowed its surface to be modified by hand-tooling. Therefore different erosion patterns could be established at the airfoil leading edge, and tested for impact on aerodynamic performance in the LSWT.

This concept for erosion testing, initially is not a very scientific method, as the application of erosion by hand-tooling is difficult to control and to repeat. Still, this method is useful to investigate trends in impact of erosion when considering erosion depths and coverage. Application of erosion was performed in a short timespan compared to the DLE model, as the complex DLE model needed to be designed from scratch whereas the quick model was already available.

In this chapter, an explanation is given of which different erosion levels and coverages were considered, as well as how the surface was modified to establish erosion patterns. The erosion patterns were 3D scanned, making it possible to perform a statistical analysis on the patterns similar to the RET specimens as discussed in Chapter 3. In this validation, the main statistical parameters between the quick erosion patterns and the RET specimens were compared.

Each erosion level was tested for aerodynamic performance in the LSWT, where transition locations were recorded using IR thermography as explained in Section 2.1, and lift was measured using the load cells and drag using the wake rake. The foam material did not allow incorporation of pressure taps, therefore lift could not be measured from the airfoil surface pressure distribution.

Finally, following a BEM method, the power curve was established. This directly shows what the impact of erosion of the quick model is to the power production.

5.1 Erosion levels and coverage

Three different erosion levels were tested, namely light, medium and heavy erosion. Light erosion represents erosion located on the mass loss curve in Figure 3.2, directly after incubation, where the erosion only penetrates into the coating with maximum depths less than 400 μm. Medium and heavy erosion are located further down the mass loss curve, where erosion would reach the glass-layers with maximum depths higher than 400 μm.

Coverage of the erosion at the leading edge is not based upon the RET specimen coverage study as explained in Section 3.4. When the quick erosion model was tested, the RET coverage study still needed to be performed. For the quick model, erosion coverage is based upon the location of the stagnation point. In this case, there was assumed that rain droplets would follow the streamlines, initially impacting at the stagnation point. Location of the stagnation point depends on the angle of attack, where for $\alpha = 0\,^\circ$ the stagnation point is located directly at the leading edge (y=0). For increasing angle of attack, the stagnation point will shift backwards on the pressure side.

Three angles of attack were considered, with accompanying stagnation points and initial locations for erosion, namely $\alpha = [0, 4, 7]^\circ$. As stated, for $\alpha = 0\,^\circ$ the stagnation point is directly at the leading edge. Assuming that the airfoil operates most often at the design angle of attack α_d, erosion initiates at $\alpha_d = 7\,^\circ$. Here the stagnation point was found using the LMWP EllipSys CFD tool, at $x_{s.p.} = 1.03\,\%$c. Subsequently $\alpha = 4\,^\circ$ was chosen as this angle is approximately in the middle between $0\,^\circ$ and $7\,^\circ$.

For $\alpha = 4\,°$, the stagnation point was found from the airfoil pressure distribution measured at an aluminium *LM18%* airfoil model with pressure taps included. The aluminium *LM18%* airfoil was the same model as used for the standardized roughness study in Chapter 4. From the pressure distribution, the chord location was estimated with a local maximum relating to a value of $C_p = 1$. In Figure 5.1 the estimated location of stagnation point is shown to be $x_{s.p.} \approx 0.32\,\%$c. This estimation was set in between two measuring points, as the pressure coefficient is not equal to one directly at the location of the pressure taps.

Angles higher than $\alpha_d = 7°$ were not considered, as for higher angles of attack the stagnation point would shift further aft on the pressure side. Erosion located on pressure side is assumed to be of less impact on the aerodynamic performance than erosion located towards suction side, as concluded for the zigzag model in Chapter 4.

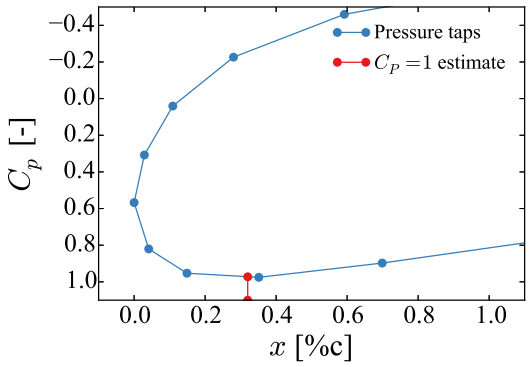

Figure 5.1: Airfoil pressure distribution to estimate stagnation point location for $\alpha = 4°$ for *LM18%* airfoil ($Re_c = 3 \cdot 10^6$).

Finally another two erosion locations were selected, both located further up towards suction side. The surface distances in between these locations were set to be the same distance as between the stagnation point at $\alpha = 4°$ and $0°$. This surface distance was calculated using the CAD drawing in Siemens NX to be $y_s = 9.28\,$mm. These locations were chosen to investigate widespread erosion, where the leading edge is heavily damaged.

The coverage of each erosion level at the airfoil is shown in Figure 5.2. The first three light erosion levels [L1,L2,L3] show erosion initiating at the stagnation point at $\alpha_d = 7°$, progressing to coverage where the stagnation point is located at the leading edge. Subsequently medium [M1,M2,M3] and heavy [H1,H2,H3] erosion were applied in the same way as for light erosion. Light, medium and heavy erosion were applied in the first location up towards suction side as [H3-L4,H3-M4,H4]. Finally light, medium and heavy erosion were applied in the second location up towards suction side as [H4-L5,H4-M5,H5]. The surface height in y-direction of one applied erosion band, at at any location (as an example for Light 1), was estimated to be 8 mm.

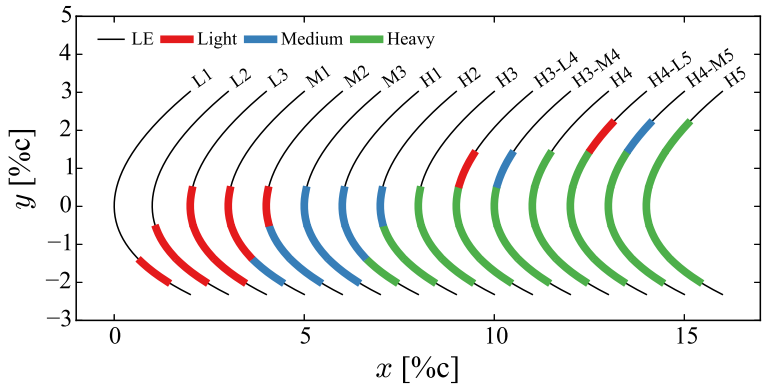

Figure 5.2: Location of light, medium and heavy erosion on *LM18%* airfoil, shifts between LE $x = 1\,\%$c.

5.2 Shaping procedure

Shaping of the erosion in the surface was done by the following hand-tooling method. As required to model the erosion accurately, material needed to be removed from the surface. By placing a tool to the surface, and hitting the tool with a hammer, the foam material was compressed and sometimes chipped off.

Different tools were tested to investigate which one resulted in a shape modification being similar to the erosion patterns as seen on the RET specimens. This investigation was based on visual inspection and the feeling of the roughened surface between the hand-tooled pattern and the RET specimens. Different tools tested were files with certain tooth sizes, a steel brush with cut wires and different aluminium RET specimens. From this analysis it appeared that the steel brush resulted in an erosion pattern similar to Phase 1 erosion of the RET specimen, whereas RET specimens could be used to create a pattern similar to Phase 2 and Phase 3 erosion.

In Figure 5.3 a picture is shown of the steel brush and an RET specimen, used as tools to create the erosion patterns. In Figure 5.4 a close-up is shown of the tools used, where the steel brush resulted in light erosion, the RET specimen in Figure 5.4b in medium erosion, and the RET specimen in Figure 5.4c in heavy erosion. The RET specimen used to create heavy erosion, shows wider and deeper valleys compared to the RET specimen used for medium erosion.

a Steel brush with shortened wires (Light)

b RET specimen (Medium and Heavy)

Figure 5.3: Tools for shaping light, medium and heavy erosion.

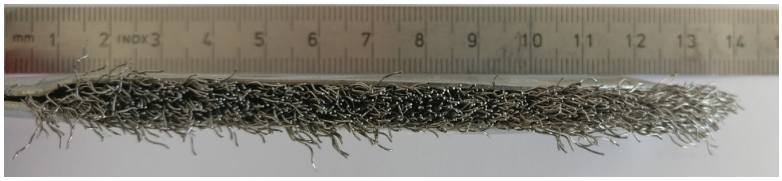

a Steel brush (light)

b RET specimen (medium)

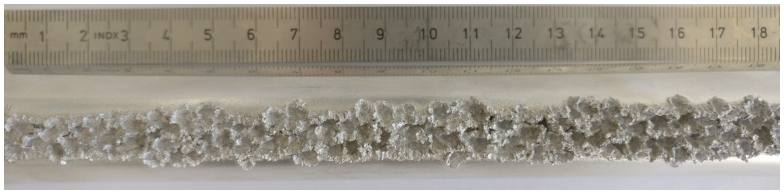

c RET specimen (heavy)

Figure 5.4: Close-up patterns of shaping tools for light, medium and heavy erosion.

By placing the tool to the surface and hitting the tool with a hammer, the erosion patterns were created. It was difficult to predict what the depth of the erosion patterns applied would be, as well as to control the force (and depth) of the hammer. As stated before, the depths of the erosion levels are most imporant to investigate similarities with erosion from the RET specimens. Therefore the patterns were 3D scanned to investigate the depths and other statistical parameters, as described in Section 5.3. Therefore the application of erosion is an unscientific approach which is difficult to control, but still the patterns can be 3D scanned and validated to see how well these compare to RET erosion specimens.

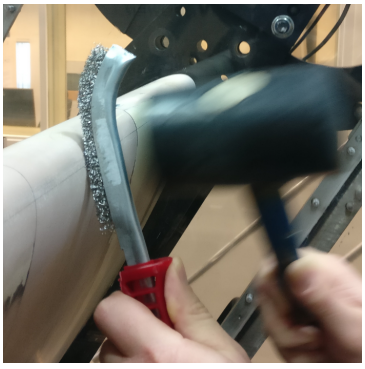

a Light

b Medium and Heavy

Figure 5.5: Shaping procedure for light, medium and heavy erosion.

The results of the shaping procedure can be seen in Figure 5.6. Subsequently a light, medium and heavy erosion pattern is shown. An increase in valley depth, width and density is clearly visible. The width in spanwise direction between the black lines is 10 cm.

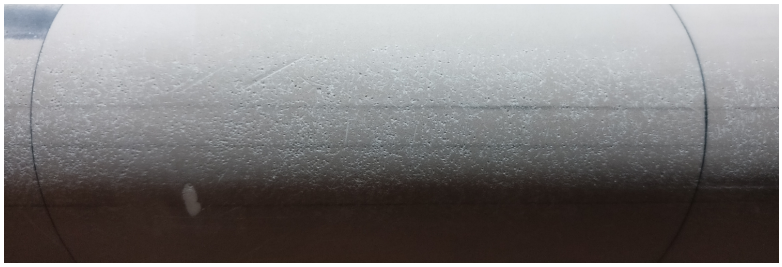

a Light 3

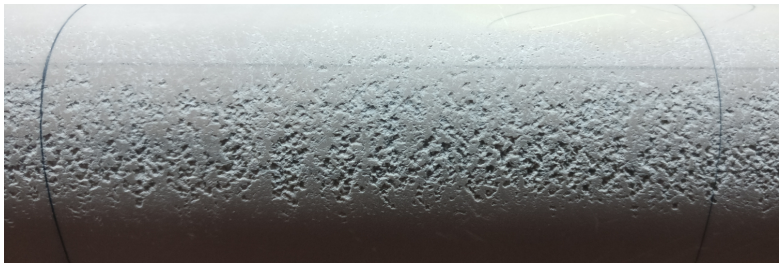

b Medium 2

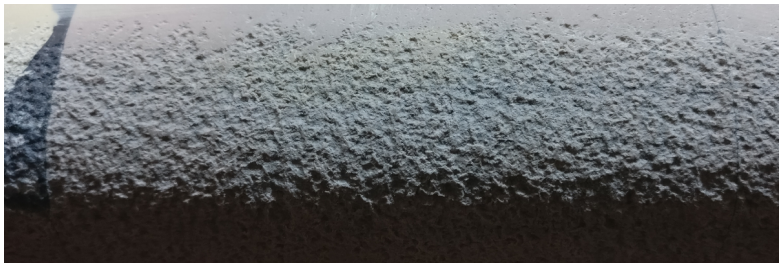

c Heavy 5

Figure 5.6: Pictures of quick erosion patterns, light (L3), medium (M2), heavy (H5), shaped using steel brush or RET specimens.

5.3 Validation to RET characteristics

The 3D scans facilitated a statistical analysis of the erosion patterns, similar to which was done for characterizing erosion from the RET specimens in Chapter 3. The statistical parameters of the quick erosion patterns were compared to the RET specimens to see how well they match, considering the main parameters of valley depth, width and distance.

Scans were performed on a medium and heavy erosion pattern, as the airfoil was only scanned after all tests (and erosion applications) were done. A medium erosion pattern was kept intact at the leading edge close to the wall, where no heavy erosion was applied at this location. This was done to make scanning of a medium erosion pattern possible. Scanning of the patterns was performed at Zebicon, the same company as where the RET specimens were scanned.

The 3D surface map of each scan is shown in Figure 5.7. Medium 3 erosion is shown in Figure 5.7a, whereas heavy 5 erosion was scanned at two different locations, resulting in heavy 5 (1) and heavy 5 (2) scans in subsequently Figures 5.7b and 5.7c.

Differences between the heavy 5 locations can be seen. For heavy 5 (2) in Figure 5.7c, there is an orange coloured part on the pressure side of the scan (negative y), meaning that there would be material coming out of the surface. Also the maximum valley depths are less deep compared to heavy

5 (1). This is caused by a misalignment of the heavy 5 (2) scan, therefore misalignment should be dealt with accordingly, following the same method as described in Section 3.3.2.3. Another cause of different valley depths is the uncontrollability of the erosion shaping method, leading to a varying range of depths along the span.

In the 3D surface maps in Figure 5.7 it can also be seen that the coverage matches well for the intended erosion level coverage, as shown in Figure 5.2. Medium 3 erosion was applied approximately between $-18 < y < 4.5\,\text{mm}$, or $-2 < y < 0.5\,\%\text{c}$ when considering the chord length of 900 mm. Heavy 5 erosion was applied approximately between $-18 < y < 18\,\text{mm}$, which matches with $-2 < y < 2\,\%\text{c}$. Therefore it is concluded that the coverage of applying erosion following this method is in control.

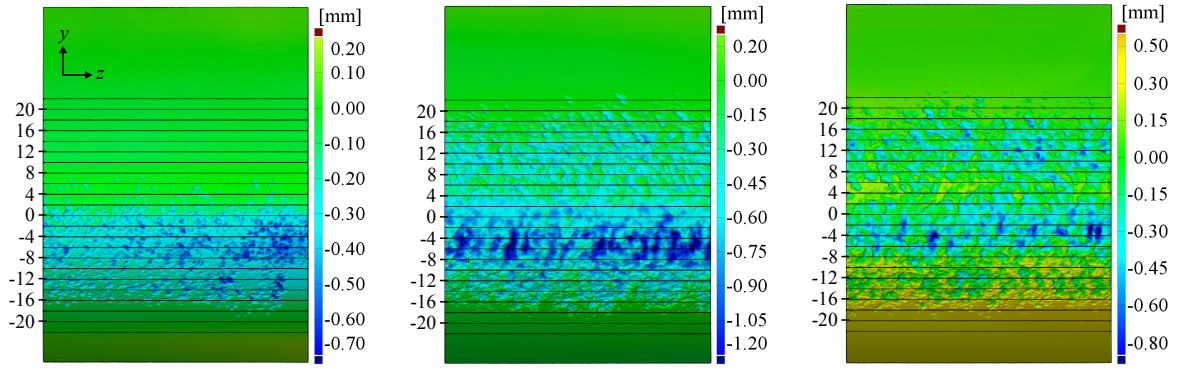

a Medium 3 **b** Heavy 5 (1) **c** Heavy 5 (2)

Figure 5.7: Three-dimensional scans of medium 3 and heavy 5 erosion (y in [mm]). For each erosion level different colour scales were used.

The next step in the statistical analysis was extracting 2D roughness curves from the 3D surface maps. Here also the alignment method was applied, leading to the 2D roughness curves. The 2D roughness curves are shown in Figure 5.8 at $y = -4\,\text{mm}$. For medium 3 and heavy 5 erosion, at this y location the erosion is heaviest as can be seen in Figure 5.6. Also thresholds for finding peaks and valleys are stated in Table 5.1, leading to the peaks and valleys data necessary to perform the statistical analysis.

Table 5.1: Thresholds for finding peaks and valleys quick erosion.

	Peaks		Valleys	
	x_n [μm]	z [mm]	x_n [μm]	z [mm]
M3	300	2	20	2
H5 (1)	300	2	50	2
H5 (2)	300	2	50	2

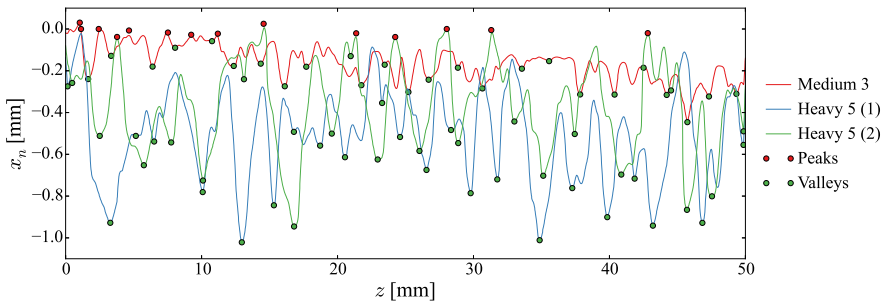

Figure 5.8: 2D roughness curves for medium 3 and heavy 5 erosion, at $y = -4\,\text{mm}$.

As concluded in Section 3.3.3 the most important parameters are the valley depth, distance and width. The results of these parameters versus y location are shown in Figure 5.9.

Erosion applied for medium or heavy erosion was expected to be approximately constant along y, but this is not the case as shown in the 3D surface maps in Figure 5.8 and for the statistical parameters in Figure 5.9. This confirms that the application method is not in control, as the erosion is smoothed out at the boundaries. Nevertheless, the smoothing at the boundaries is a feature that is also observed at the eroded RET specimens, and therefore is assumed to be a realistic representation of erosion.

On the pressure side, for negative y values, a difference is observed between the two heavy 5 erosion locations. Heavy 5 (1) shows deeper average valleys and higher valley widths in this region, confirming the difficulty to control the application of erosion.

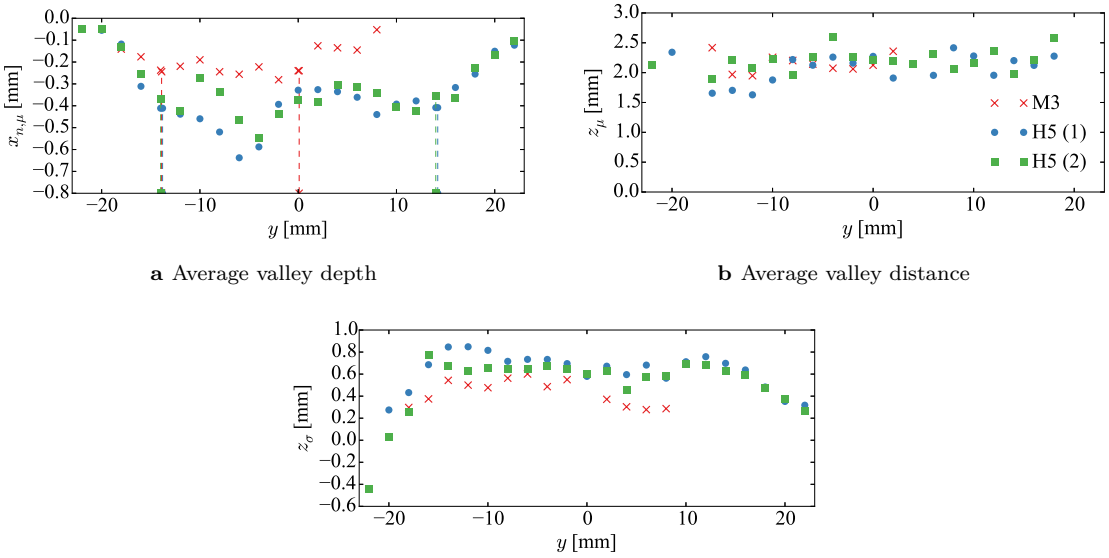

a Average valley depth

b Average valley distance

c Average of sigma Gaussian fits (width)

Figure 5.9: Valley depth, distance and width parameters along y, for Medium 3 and Heavy 5 erosion.

To extract the average and standard deviation of the main statistical parameters (valley depth, width and distance), following the same method as for the RET specimens, first a constant area is selected. The constant areas for medium and heavy erosion are indicated in Figure 5.9a. For medium erosion, the pattern appears to be constant between $-14 < y < 0\,\text{mm}$, whereas for heavy erosion, the pattern is approximately constant between $-14 < y < 14\,\text{mm}$.

These parameters are shown in Table 5.2 and were compared to the RET specimen parameters in Table 3.4. Now when considering the averages of valley depth: medium erosion results in $\mu_{x_{n,\mu}} = -0.2363$

wich matches well with Phase 2 erosion $\mu_{x_{n,\mu}} = -0.22836$. Heavy erosion $\mu_{x_{n,\mu}} = [-0.4265, -0.3831]$ is more shallow than Phase 3 erosion at $\mu_{x_{n,\mu}} = -0.5359$, but is still considered to be close. From this it was concluded that following this application method, erosion depths can be reached similar to erosion as seen on RET specimens.

Heavy erosion has wider valleys than medium erosion, as expected from the close-up of the shaping tools shown in Figure 5.3. Average valley widths and distances are higher for the quick erosion patterns (medium and heavy) compared to the RET specimens, though assumed to be of less influence to aerodynamic performance than erosion depth.

All other statistical parameters have not been compared to the RET specimens and can be found in Appendix A. As there was no 3D scan for the light pattern, no statistics were computed and therefore could not be compared to the RET specimens.

Table 5.2: Average and standard deviation of valley depth, distance and width parameters, for Medium 3 and Heavy 5 erosion.

	Valley depth		Valley distance		Valley width	
Level	$\mu_{x_{n,\mu}}$ [mm]	$\sigma_{x_{n,\mu}}$ [mm]	μ_{z_μ} [mm]	σ_{z_μ} [mm]	μ_{z_σ} [mm]	σ_{z_σ} [mm]
M3	-0.236	0.0985	2.09	0.690	0.540	0.253
H5 (1)	-0.427	0.178	2.05	0.705	0.717	0.303
H5 (2)	-0.381	0.168	2.19	0.727	0.628	0.281

5.4 Aerodynamic performance results

Aerodynamic performance was measured in terms of lift and drag by the load cells, and in terms of transition location by infrared thermography. Analysis of aerodynamic performance was done at $Re = 3 \cdot 10^6$ and $Re = 6 \cdot 10^6$, simulating realistic operational conditions.

5.4.1 IR: transition

Following the IR thermography method as described in Section 2.1, the transition location on the airfoil surface was found. These locations of transition are estimates, as finding the exact location was difficult considering the low resolution of the IR camera.

For a range in angles of attack, an IR image was taken and the transition location was estimated. It is expected that for increasing erosion levels, the transition location shifts forward towards the leading edge. Transition locations of each angle of attack and each erosion level were compared to each other, to analyse this shift in transition location. Early transition subsequently results in detrimental effects on lift and drag, as will be shown in Section 5.4.2.

5.4.1.1 $Re = 3 \cdot 10^6$

For each angle of attack, the transition location was estimated as the chord distance from the leading edge. At a certain angle of attack, the IR image will show a heavily disturbed flow, where vortices are initiated at the leading edge and show up as cones in the (for lower angles of attack undisturbed) flow. At this point, a clear transition location cannot be defined and is considered as being shifted fully towards the leading edge, resulting in $x_t = 0\,\%$c. The angle of attack where this clear transition shift towards the leading edge appears, is valuable to compare between the different erosion levels.

The IR images for the angles of attack where the transition location shift occurs, are shown in Figure 5.11. This shows that going from a clean airfoil to increasing erosion levels, the angle of attack decreases at which the transition shift occurs. For increasing erosion levels, the angle of attack decreases

where the transition shift is visible as a heavily disturbed flow with cones (vortices) initiating at the leading edge.

For light 1 (L1) erosion, where erosion is located at the design angle of attack stagnation point, no clear difference in transition shift is visible compared to the clean airfoil. No change was also observed when increasing the erosion at the stagnation point going from light 3 (L3) to medium 1 (M1) erosion, as well as going from medium 3 (M3) to heavy 1 (H1) erosion. IR images of medium 1 (M1) and medium 3 (M3) erosion are not included in Figure 5.11, as M1 is similar to L3 and H1 similar to M3. This shows that erosion located directly at the stagnation point has no significant impact on a transition shift, and therefore is expected to also have a minor effect on lift and drag as will be discussed in Section 5.4.2. This is probably caused by the boundary layer containing the maximum amount of energy at the stagnation point and therefore cannot easily be disturbed. In general no shift in transition location can be observed before cones in the previously laminar part of the flow start to appear.

Medium 2 erosion results in a transition shift at the design angle of attack. Therefore at this erosion level the flow would already be heavily disturbed at optimal operating conditions. Further increasing the erosion continues to shift the transition location, except for increasing erosion at the stagnation point. Also there is no clear shift between H4 and H4-L5 erosion. It appears that at this level the flow is already disturbed to an extend that adding light erosion towards suction side only has a minor impact. The final heavy 5 erosion level leads to a fully turbulent flow already at negative angles of attack.

In Figure 5.10a for each erosion level the estimates of transition locations for a range in angle of attack are shown. This also shows no significant difference between clean and light 1 erosion, where erosion initiates at the stagnation point. Light 2 erosion is also still similar to the clean curve, though more cones appear in the flow as can be seen in Figure 5.11b. Light 3 erosion has a fully turbulent flow at $\alpha = 8°$ and as stated before is similar to medium 1 erosion. Subsequently transition shifts occur going from M1 to M2 erosion and going from H1 to H2 to H3 erosion, as well as for increasing erosion to medium and heavy levels up to the suction side (H3-M4 to H4 and H4-M5 to H5).

For future IR-thermography studies it is recommended to investigate at a higher resolution in angles of attack, by taking images with a lower step size in angles of attack. Still with this study the trend in transition shift for increasing erosion levels is clearly visible.

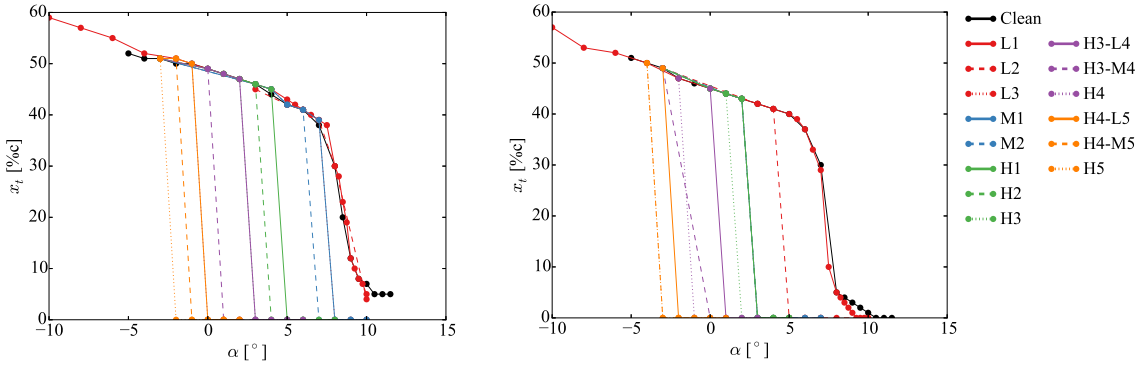

a $Re = 3 \cdot 10^6$ **b** $Re = 6 \cdot 10^6$

Figure 5.10: Quick erosion transition locations as determined by IR-thermography. The linear part of the curves indicate the angle of attack where sudden early transition (at leading edge) due to erosion occurs. Therefore the different linear curves show the transition shift to a lower angle of attack for higher erosion levels.

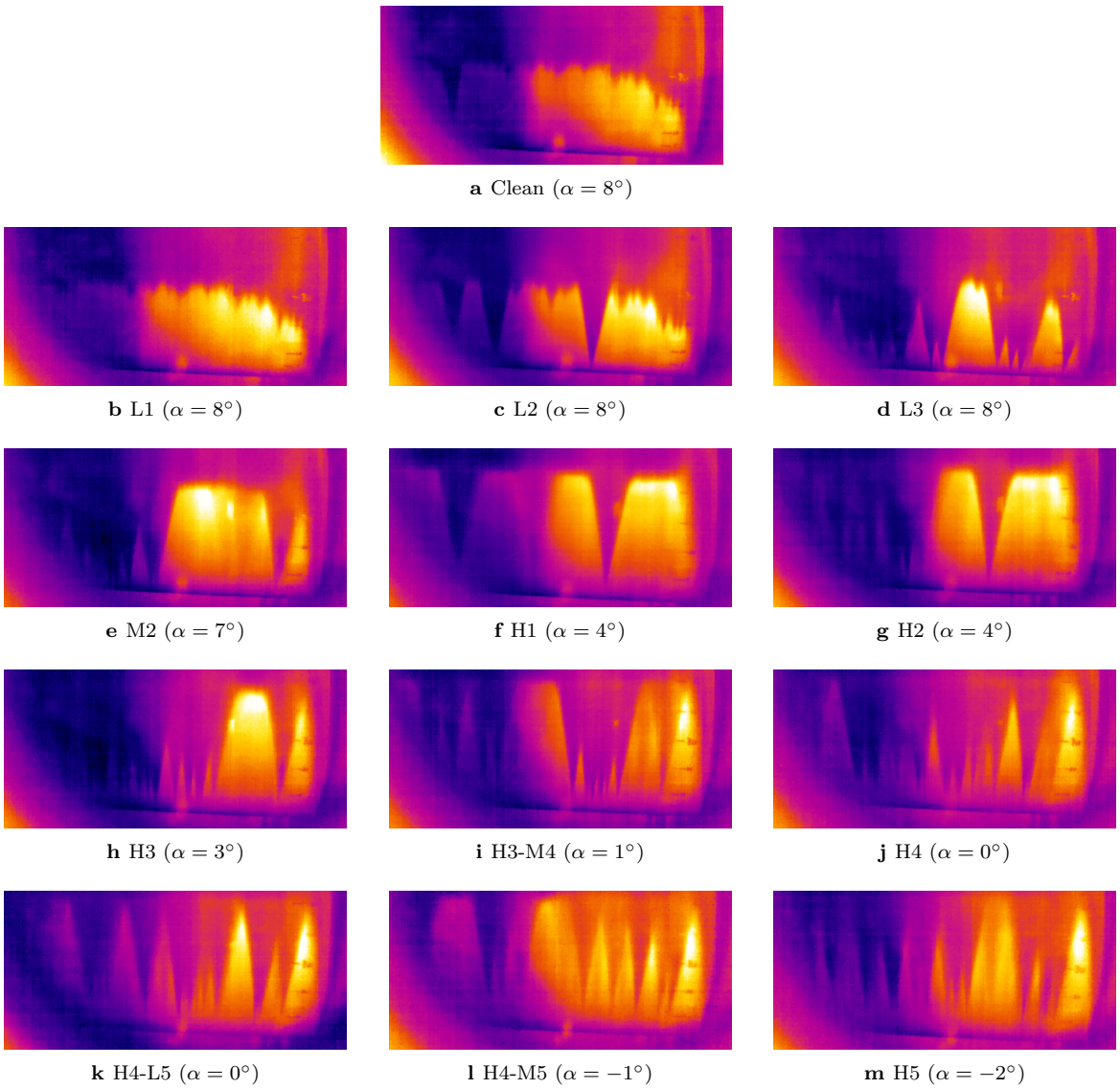

a Clean ($\alpha = 8°$)

b L1 ($\alpha = 8°$) **c** L2 ($\alpha = 8°$) **d** L3 ($\alpha = 8°$)

e M2 ($\alpha = 7°$) **f** H1 ($\alpha = 4°$) **g** H2 ($\alpha = 4°$)

h H3 ($\alpha = 3°$) **i** H3-M4 ($\alpha = 1°$) **j** H4 ($\alpha = 0°$)

k H4-L5 ($\alpha = 0°$) **l** H4-M5 ($\alpha = -1°$) **m** H5 ($\alpha = -2°$)

Figure 5.11: IR for quick erosion $Re = 3 \cdot 10^6$.

5.4.1.2 $Re = 6 \cdot 10^6$

In Figure 5.12 the IR images can be seen for $Re = 6 \cdot 10^6$, where the effect of erosion to the flow is worse compared to $Re = 3 \cdot 10^6$. For light 2 erosion, the flow transitions already at $\alpha = 5°$ to fully turbulent from the leading edge. For all erosion levels, the transition to a fully turbulent flow appears at lower angles of attack compared to $Re = 3 \cdot 10^6$. This shows a clear Reynolds effect, where erosion influences the aerodynamic performance increasingly for higher Reynolds numbers. This is because at higher Reynolds number the boundary layer of the flow is thinner, resulting to the flow experiencing worse conditions.

As for $Re = 3 \cdot 10^6$, erosion initiating at the stagnation point does not show significant changes to the flow, when comparing clean to L1 or L3 to M1 erosion. In general going from light 3 (via M2 and M3) to heavy 1 erosion the flow does not shift significantly, more cones appear but transition to fully turbulent flow remains at approximately $\alpha = 3°$. Highest shifts in flow transition occurs when the erosion is applied up towards suction side, so going from M1 to M2, or M2 to H1.

In Figure 5.10b the estimates of transition locations versus angle of attack are shown. This shows the same trend as for $Re = 3 \cdot 10^6$. There is no significant difference between clean and light 1 erosion, where erosion initiates at the stagnation point. Only now already for light 2 erosion, the transition to fully turbulent flow is shifted (at $\alpha = 5°$). Light 3 to heavy 1 erosion are similar, though more cones appear in the flow as can be seen in Figure 5.12g. Subsequently transition shifts occur increasing from H1 erosion. H3-M4 erosion lacks IR measurements between $-3 < \alpha < 0°$, therefore the transition shift appears to be mismatched compared to the others. The expected transition shift would approximately be at $\alpha = -1°$.

Images should have been taken at lower step size in angle of attack, to better capture the difference between the erosion levels. Now too rough estimates of transition shifts were taken, as can be seen for H3-M4 erosion.

Still these tests confirm that for both Reynolds numbers the erosion located directly at the stagnation point has the least impact on transition location. The impact increases when applying erosion to suction side. The zigzag study in Chapter 4 showed the same conclusions.

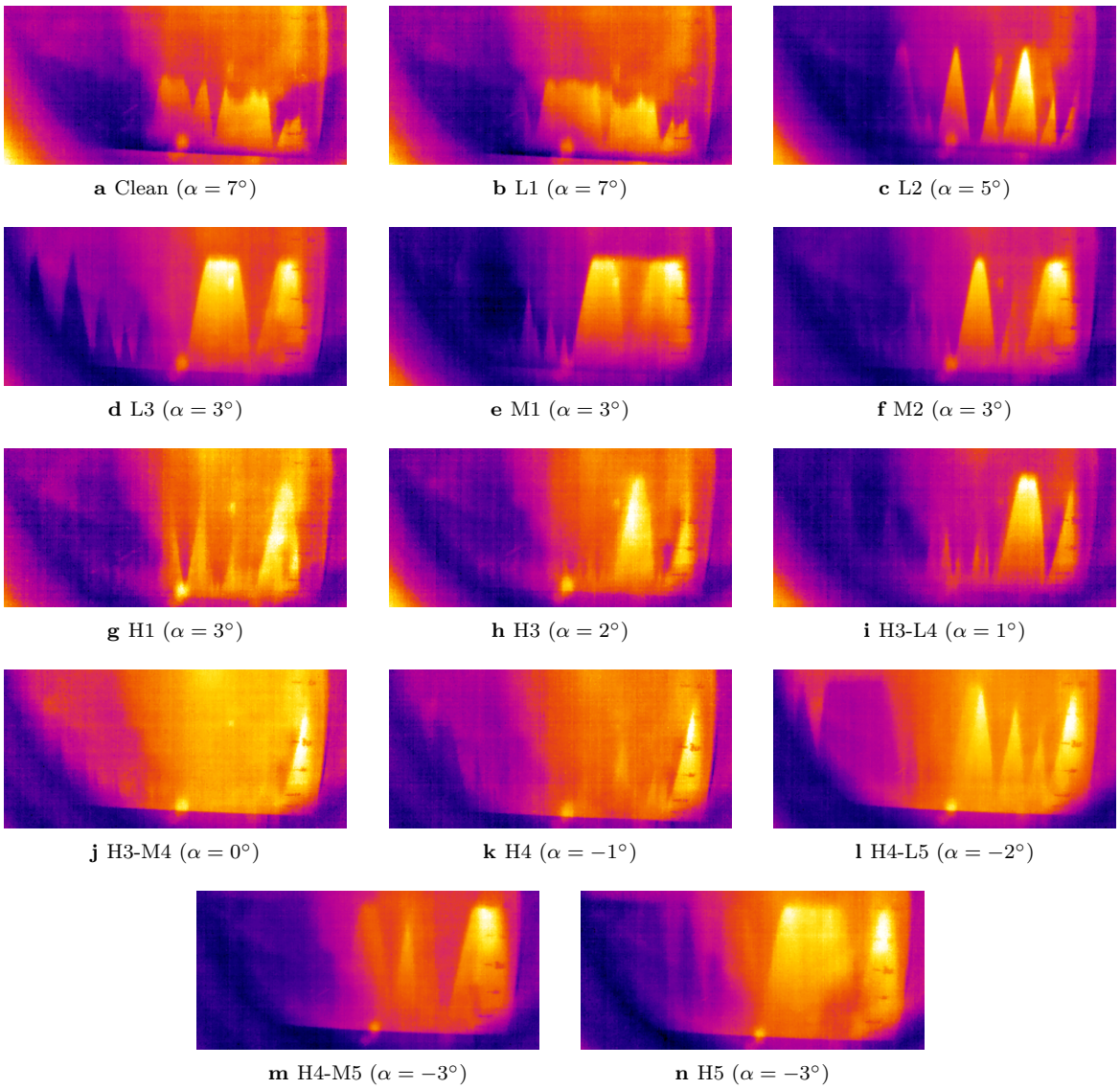

a Clean ($\alpha = 7°$) **b** L1 ($\alpha = 7°$) **c** L2 ($\alpha = 5°$)

d L3 ($\alpha = 3°$) **e** M1 ($\alpha = 3°$) **f** M2 ($\alpha = 3°$)

g H1 ($\alpha = 3°$) **h** H3 ($\alpha = 2°$) **i** H3-L4 ($\alpha = 1°$)

j H3-M4 ($\alpha = 0°$) **k** H4 ($\alpha = -1°$) **l** H4-L5 ($\alpha = -2°$)

m H4-M5 ($\alpha = -3°$) **n** H5 ($\alpha = -3°$)

Figure 5.12: IR for quick erosion $Re = 6 \cdot 10^6$.

5.4.2 Lift and drag

The lift and moment coefficients were measured using the load cells. The drag coefficient in the linear part of the lift curve was established by means of a traversing wake rake. Outside of the linear part of the lift curve, the drag was measured using the load cells. This is caused by the fact that the wake rake cannot measure the drag when the flow becomes too turbulent in the stall region. Also lift versus drag coefficient and lift over drag versus angle of attack were computed. Measurements were taken going from a high positive angle of attack to negative, both for $Re = 3 \cdot 10^6$ and $Re = 6 \cdot 10^6$. Finally, the decrease in lift and increase in drag for each erosion level compared to the clean airfoil were calculated, at the angle of attack where lift over drag coefficient is maximum.

5.4.2.1 $Re = 3 \cdot 10^6$

In Figure 5.13 the lift, drag and moment coefficients are shown for each tested quick erosion level. In general increasing erosion decreases the lift and increases the drag.

For each erosion level the lift curves in Figure 5.13a appear to follow the clean curve, until the angle of attack where the estimated transition shift occurs. As an example the curves for M3 and H1 erosion, where the transition shift occurs at $\alpha = 4°$ as can be seen in Figure 5.11f; above this angle the curves show a different gradient and deviate significantly from the clean curve. This confirms that the shift in transition location due to increased erosion has a detrimental effect on the lift performance.

When applying erosion at the stagnation point, the lift is marginally affected as compared to applying erosion further up to suction side. The curve for L1 erosion is similar to the clean curve, as well as M1 erosion is similar to L3 and H1 is similar to M3. This confirms with IR thermography where no transition shifts were observed when erosion was applied at the stagnation point. Increasing the erosion also shifts the stall region to a lower angle of attack, as the maximum lift coefficient is reached at a lower angle compared to the clean curve.

Drag results in Figure 5.13b show the heaviest increase when erosion is applied furthest up on suction side, as for [L3,M3,H4] erosion. From L3 erosion and up, the drag has increased along its full range in angle of attack. Also the drag results show a shift in stall region, where from medium erosion the drag results become unreliable for angles above $\alpha = 7°$ compared to the clean curve.

From Figure 5.13d the maximum lift over drag coefficient was determined for the clean airfoil, with its corresponding angle of attack at $\alpha = 7°$. These lift over drag results also show the trend that increasing erosion at the stagnation point has the least impact, whereas increasing the erosion towards furthest up on suction side results in the highest decrease in performance (going from L2 to L3, from M2 to M3 and from H2 to H3).

Finally the percentage decrease in lift and increase in drag are shown in Table 5.3, compared to the clean airfoil at $\alpha = 7°$, the angle where C_l/C_d is maximum for the clean curve. A large step in lift decrease and drag increase occurs at L3 and M3 erosion, where erosion is applied up to suction side. Above M3 erosion, the performance loss at $\alpha = 7°$ decreases more gradually, as the flow is already completely transitioned to a turbulent flow directly at the leading edge.

Table 5.3: Lift and drag results at $\alpha_d = 7°$ for quick erosion ($Re = 3 \cdot 10^6$).

Phase	C_l-decrease [%]	C_d-increase [%]	C_l/C_d-decrease [%]
Clean	0	0	0
L1	1.02	-1.99	-0.99
L2	2.18	4.70	6.57
L3	4.97	35.1	29.7
M1	3.99	28.9	25.5
M2	5.35	33.9	29.3
M3	10.8	93.9	54.0
H1	11.1	94.0	54.2
H2	12.1	97.3	55.5
H3	12.6	102.6	56.9
H3-L4	13.6	104.6	57.8
H3-M4	12.9	106.7	57.9
H4	14.0	115.7	60.1
H4-L5	14.4	115.5	60.3
H4-M5	16.9	123.2	62.8
H5	16.4	130.0	63.7

5.4.2.2 $Re = 6 \cdot 10^6$

For $Re = 6 \cdot 10^6$ in Figure 5.14 the aerodynamic performance is shown for each erosion level. The effect of higher Reynolds number is that the transition shift occurs at lower angles of attack. Above these transition angles, the lift curves for the different erosion levels in Figure 5.14a are more similar to each other as compared to the $Re = 3 \cdot 10^6$ results. From L3 erosion, the transition shift occurs at $\alpha = 3°$, where for increasing erosion levels the lift results are similar above this angle. The flow is already disturbed to an extent that heavier erosion has less impact on the lift.

The same trend in lift and drag results is seen for applying erosion at the stagnation point, where these are marginally affected as compared to applying erosion further up to suction side. The curve for L1 erosion is similar to the clean curve, as well as M1 erosion is similar to L3 and H1 is similar to M3.

Subsequently from Figure 5.13d the maximum lift over drag coefficient was determined for the clean airfoil, with its corresponding angle of attack at $\alpha = 6°$. These lift over drag results also show the trend that increasing erosion at the stagnation point has the least impact, whereas increasing the erosion towards furthest up on suction side results in the highest decrease in performance (going from L2 to L3, from M2 to M3 and from H2 to H3).

Finally the percentage decrease in lift and increase in drag are shown in Table 5.4, compared to the clean airfoil at $\alpha = 6°$ for maximum C_l/C_d. Here a large step in lift over drag decrease occurs already at L2 erosion, where erosion is applied up to suction side. Above L2 erosion, the performance loss at $\alpha = 6°$ decreases more gradually, because of the completely transitioned flow directly at the leading edge. Light erosion up to M3 shows performance losses higher compared to $Re = 3 \cdot 10^6$, mainly for the drag coefficient. This shows that for early erosion stages, the erosion has an increasing detrimental effect to aerodynamic performance for higher Reynolds numbers. Because the boundary layer thickness decreases for higher Reynolds numbers, the erosion will disturb the boundary layer to a higher extent.

The maximum relative performance loss is less for $Re = 6 \cdot 10^6$ than for $Re = 3 \cdot 10^6$, which was also observed for the zigzag model. At higher Reynolds number, for fully transitioned flow, a higher amount of energy is added to the flow, whereas the absolute performance loss is similar to testing at lower Reynolds number. Therefore the relative performance loss will be less.

Table 5.4: Lift and drag results at $\alpha_d = 6°$ for quick erosion ($Re = 6 \cdot 10^6$).

Phase	C_l-decrease [%]	C_d-increase [%]	C_l/C_d-decrease [%]
Clean	0	0	0
L1	0.08	5.57	5.36
L2	3.86	40.3	31.5
L3	6.83	68.6	44.7
M1	6.96	65.6	43.8
M2	6.86	67.3	44.3
M3	7.32	73.6	46.6
H1	6.54	75.1	46.6
H2	7.14	73.8	46.6
H3	7.32	77.8	47.9
H3-L4	6.70	78.2	47.7
H3-M4	7.02	79.1	48.1
H4	7.28	83.9	49.6
H4-L5	7.16	84.9	49.8
H4-M5	7.68	86.9	50.6
H5	7.70	91.1	51.7

5.5 Power loss

The power loss due to leading edge erosion was estimated using a Blade Element Momentum calculation. As the *LM18%* tip airfoil is being used an LMWP blade, the eroded aerodynamic polars could be used in a BEM set-up for this particular blade. This blade is being used for a 2.5 MW wind turbine, where the tip length, airfoil thickness and airfoil distribution are confidential.

There is chosen to perform the Annual Energy Production (AEP) calculation at a point in time where breakthrough occurs in the tip region of the blade. When heavier erosion is observed, a repair is a necessity due to structural degradation of the blade.

5.5.1 BEM inputs

A thorough description of the BEM tool is not included, as this is an internal BEM software developed by LMWP. The tool is based upon general blade element momentum theory, leading to the power curve and AEP and requires the following three input files. These three files are the blade file, the profile file and the turbine file.

The blade file with sectional info describes the airfoil distribution, and therefore where each particular airfoil is located along the blade. At these exact locations the polar data will be the same as for the corresponding airfoils as described in the profile file. In between these exact locations, the airfoil polar data is computed as an interpolation of the polar data from the two airfoils on each side of this arbitrary location. Subsequently the profile file with sectional polar data includes the lift, drag and moment polars from $\alpha = -180\,^\circ$ till $\alpha = 180\,^\circ$ for each airfoil used in this blade. Finally the turbine file describes the control parameters of the turbine and the considered wind class.

1. Blade file with sectional info
2. Profile file with sectional polar data
3. Turbine file with turbine related info

These three files were used to calculate the AEP for a turbine with clean blades and was used as a reference for the baseline AEP.

To incorporate leading edge erosion, the inputs needed to be adjusted. The turbine file remained the same, as it describes external climate parameters and the control of the turbine. In the profile file the polar data was adjusted for the airfoils located at the eroded parts of the blade.

5.5.2 Erosion coverage along the blade

RET tests at LMWP showed that for a maximum tip speed corresponding to this blade, the breakthrough (heavy erosion with delamination) of erosion in the tip region will occur after a certain amount of time and rainfall. This point in time is confidential, though occurs well within the operational lifetime of an average wind turbine. Also RET tests showed that incubation (light erosion) occurs at the spanwise region which encounters wind speeds higher than a certain velocity (also confidential). This means that for this specific blade, after the certain amount of years it takes till breakthrough occurs in the tip region, erosion will occur from 85 % from the root and all the way to the tip (100 %).

The blade file with sectional info results in three airfoils that will be affected by this erosion stage, as these three airfoils lie on the outer region in the eroded zone. Thickness of these airfoils are confidential, though the tip airfoil is similar to the *LM18%* tip airfoil as tested for the quick erosion model. Airfoil distributions are as follows: the tip airfoil is located directly at the tip at 100 %, the near-tip airfoil is located at 95 % and finally the inboard airfoil is located at 85 % of the tip length.

The inboard airfoil spans from 85 % further inwards towards the root, and therefore spans further inwards than were erosion would occur. Exchanging clean to eroded data for the inboard airfoil would be incorrect, as this would lead to a performance decrease at inboard sections of the blade where the blade is still considered to be clean.

As a solution, another airfoil was inserted between the eroded near-tip airfoil and the clean inboard airfoil. This auxiliary airfoil profile was given a certain thickness similar to the inboard airfoil, and is located at 87 % which is close to the inboard airfoil. This method ensured that erosion data was only applied to the blade from 87 % to the tip.

The resulting airfoil distribution, with tip, near-tip and auxiliary airfoils considered to be eroded and the inboard airfoil considered to be clean, are shown in Figure 5.15. Also the relative erosion coverage is shown, with heavy erosion for the tip airfoil, medium erosion for the near-tip airfoil and light erosion for the auxiliary airfoil. In between these locations the BEM tool interpolates between the bordering airfoil polar data.

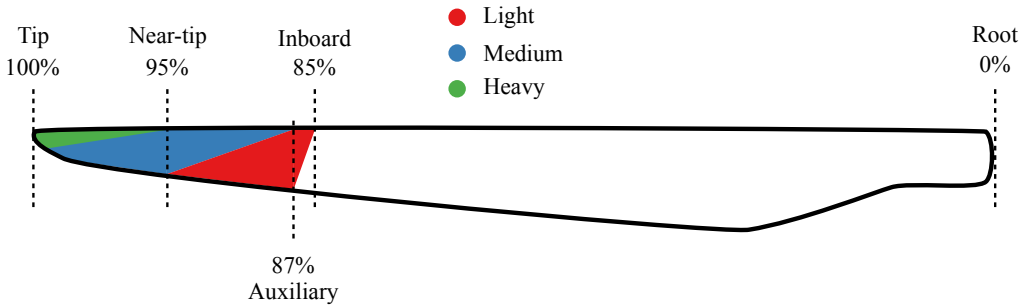

Figure 5.15: Spanwise coverage of erosion levels and airfoil distribution for BEM study.

5.5.3 Erosion polar data

The development of erosion on a blade will be proportional to the incoming wind speed, which is related to the rotational velocity. Therefore incoming wind speed is highest at the tip and lower at the inboard regions of the blade (lowest at the root). Following this pattern, erosion levels were considered as light, medium and heavy erosion corresponding to each eroded airfoil profile (subsequently the auxiliary, near-tip and tip airfoil). The polar data for light, medium and heavy erosion was taken from the quick erosion model, using the light 3 polar data for the auxiliary airfoil, the medium 3 data for the near-tip airfoil and finally heavy 3 data for the tip airfoil.

These three erosion levels were measured during the quick erosion campaign on the *LM18%* airfoil which can be used directly for the tip airfoil. However no erosion data exists for the near-tip and inboard airfoil profiles. There the data of the quick erosion campaign was extrapolated to the near-tip and inboard airfoils.

For each of the three airfoil profiles there is described how the quick erosion data was used to obtain the extrapolated erosion data.

5.5.3.1 Tip airfoil

First the clean data for the tip airfoil was taken from the BEM profile file, in a range of $\alpha = -180\,^\circ$ to $\alpha = 180\,^\circ$. Secondly the wind tunnel data for quick erosion heavy 3 was taken as well as the corresponding clean case at the relevant Reynolds number from Section 5.4.2. The absolute difference was calculated between the clean and the eroded case for lift, drag and moment coefficients. Now this absolute difference in lift, drag and moment coefficient was applied to the BEM clean profile data.

As the range in angle of attack of data for the quick model is only approximately from $\alpha = -15\,^\circ$ to $\alpha = 15\,^\circ$, the erosion difference could only be applied to the tip airfoil data within this range. Outside of this range it can be assumed that the erosion has no impact, as the wind turbine blades in normal operation will not encounter these extreme angles of attack. Therefore at the borders of this range the modified for erosion data was interpolated to the original clean tip airfoil data, to avoid discontinuities in the final erosion polars.

Finally the BEM clean polar data was replaced with the tip erosion polars in the profile input file for the BEM computation. The modified lift and drag polars are shown in Figure 5.16. The modified moment polar was obtained following the same methodology but is not shown below.

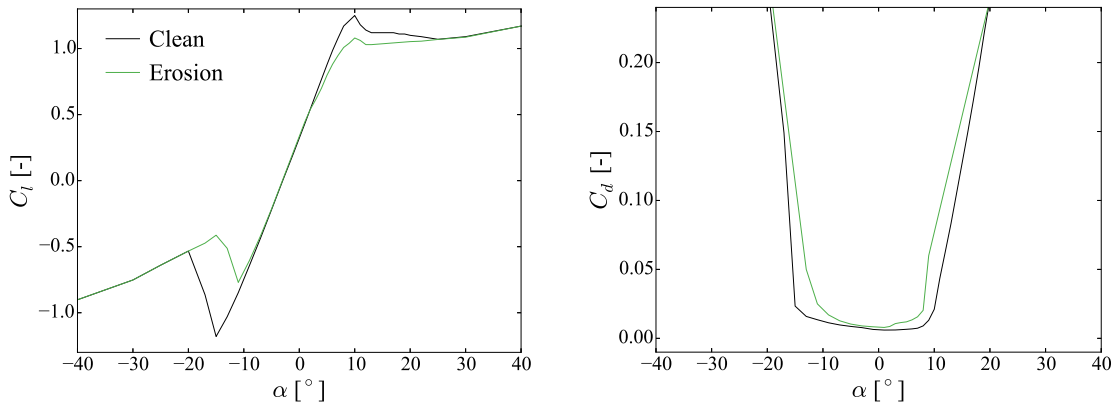

a Lift **b** Drag

Figure 5.16: Lift and drag polars for the tip airfoil after modifying with heavy erosion data.

5.5.3.2 Near-tip airfoil

The BEM clean data for the near-tip airfoil was taken, in a range of $\alpha = -180\,°$ to $\alpha = 180\,°$. Now the wind tunnel data for quick erosion medium 3 was taken as well as the corresponding clean case at the relevant Reynolds number from Section 5.4.2. This time the relative difference was calculated between the clean and the eroded case for lift, drag and moment coefficients.

The absolute difference cannot be used as two airfoil profiles with different thickness were compared, with different lift slopes and different angles of attack for maximum lift. Therefore the angles of attack for the medium 3 erosion polars were shifted, ensuring the maximum lift coefficient of the medium 3 polar is located at the same angle of attack as for the clean near-tip airfoil profile. Subsequently the relative difference in lift, drag and moment coefficient was applied to the BEM clean tip airfoil data.

As for the tip airfoil, the curves were inspected for discontinuities and interpolated at the border regions where the relative difference due to erosion was applied. The BEM clean polars for lift, drag and moment coefficient were replaced with the near-tip erosion polars in the profile input file for the BEM computation. The modified lift and drag polars are shown in Figure 5.17.

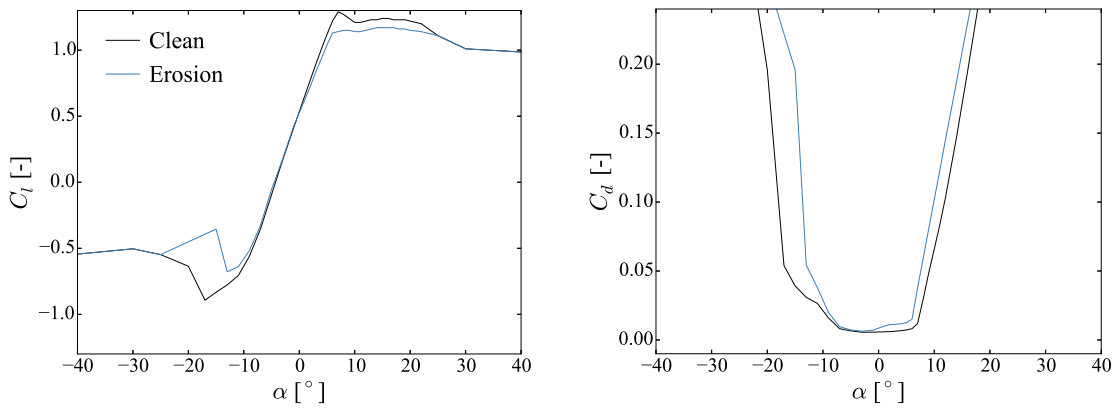

a Lift **b** Drag

Figure 5.17: Lift and drag polars for the near-tip airfoil after modifying with medium erosion data.

5.5.3.3 Auxiliary airfoil

For the auxiliary airfoil the clean BEM data was taken to be the same data as for the inboard airfoil profile, as the auxiliary airfoil is located close to the inboard airfoil. The wind tunnel data for quick erosion light 3 was taken as well as the corresponding clean case at the relevant Reynolds number from Section 5.4.2. Also for the auxiliary airfoil the relative difference was calculated from the quick erosion campaign, between the clean and the eroded case for lift, drag and moment coefficients.

The angles of attack for the light 3 erosion polars were shifted, ensuring the maximum lift coefficient of the light 3 polar is located at the same angle of attack as for the clean auxiliary (inboard) airfoil profile. The relative difference in lift, drag and moment coefficient was applied to the clean auxiliary airfoil data, followed by an inspection for discontinuities and interpolation at the border regions where the relative difference due to erosion was applied.

Now the auxiliary airfoil erosion polars were included in the profile input file, at a spanwise location just after the inboard airfoil (closer towards the tip). The eroded auxiliary airfoil lift and drag polars are shown in Figure 5.18. The polars for the inboard airfoil in the profile input file remain to be the same, which is uneroded.

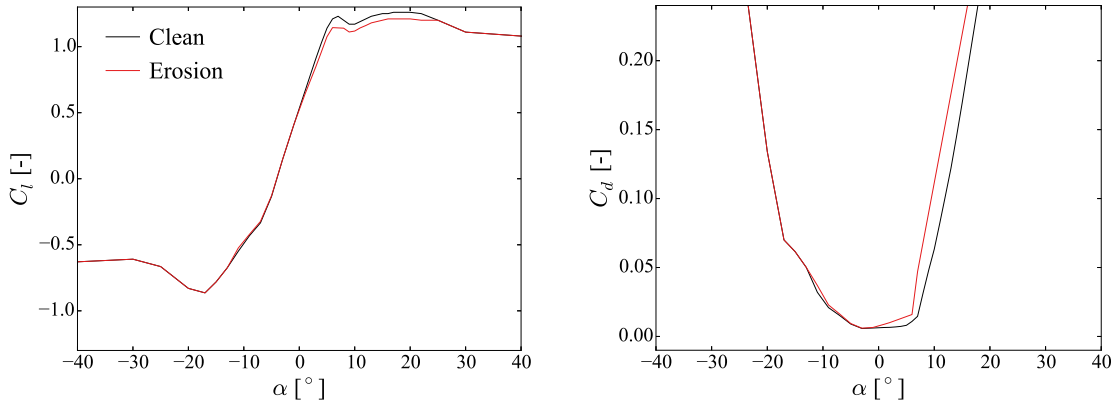

a Lift **b** Drag

Figure 5.18: Lift and drag polars for the inboard airfoil after modifying with light erosion data.

5.5.4 AEP calculations

Finally the AEP calculation was done in the same way as for the AEP calculation for the clean case. To compute the eroded case, the input profile file was used that included the eroded polars for the tip, near-tip and auxiliary airfoil profiles. This led to both the power curve and the annual energy production, as shown in Figure 5.19. As an example at an average wind speed of 7.5 $^{m}/_{s}$ the potential loss in annual energy production due to leading edge erosion will be approximately 1 %, which can be immediately linked to a loss in revenue.

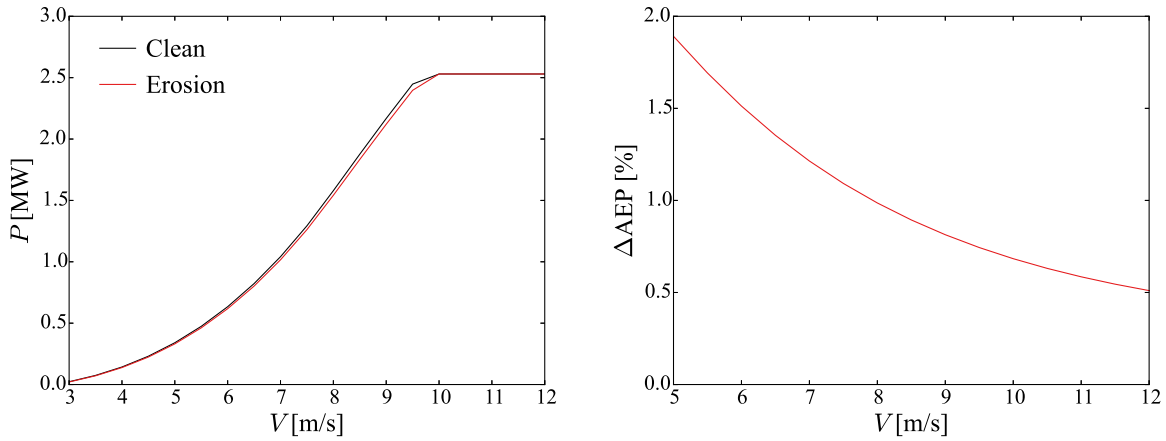

a Power curve

b AEP loss

Figure 5.19: The power curve and annual energy production for the clean versus the eroded blade.

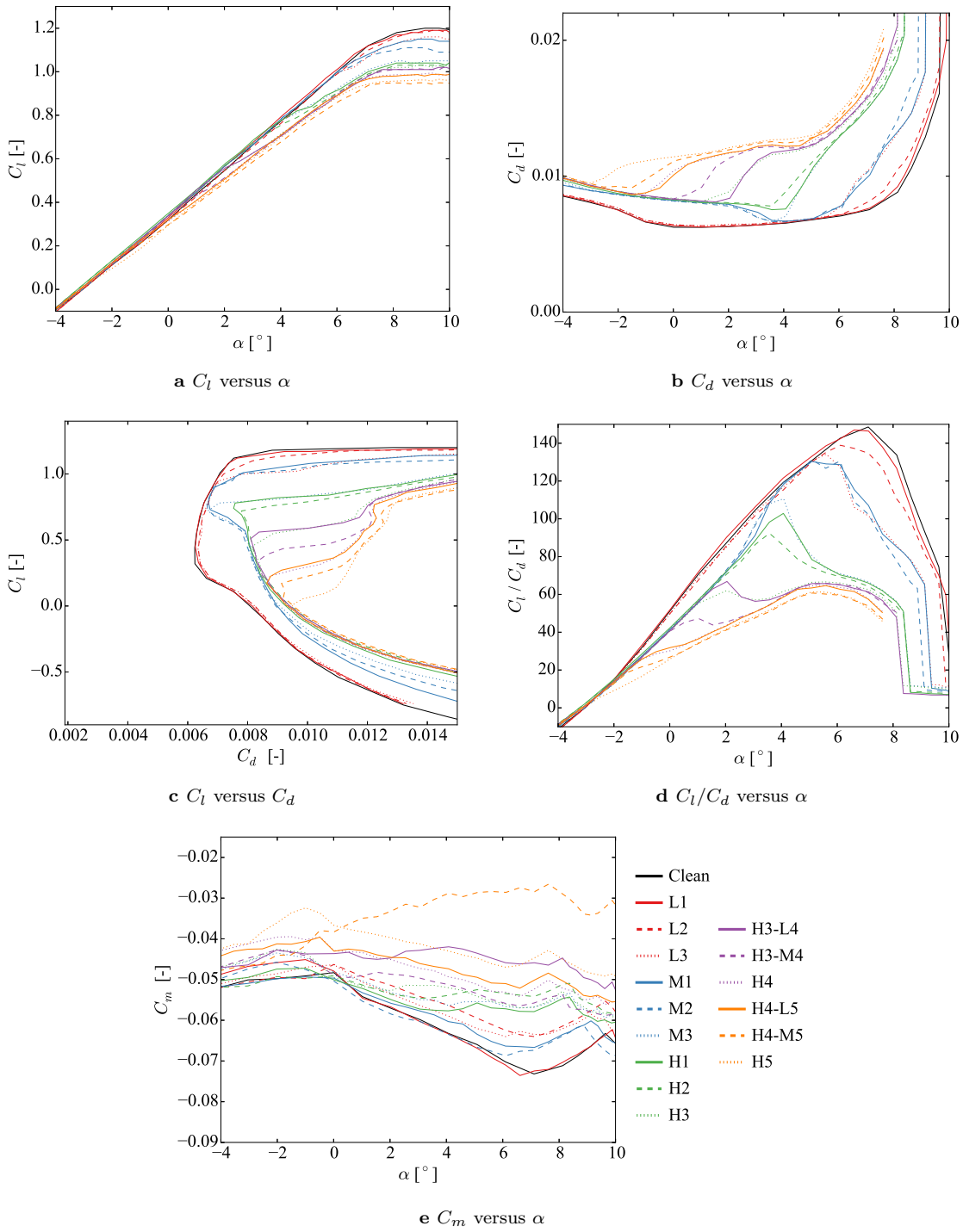

a C_l versus α

b C_d versus α

c C_l versus C_d

d C_l/C_d versus α

e C_m versus α

Figure 5.13: Aerodynamic performance for quick erosion and $Re = 3 \cdot 10^6$.

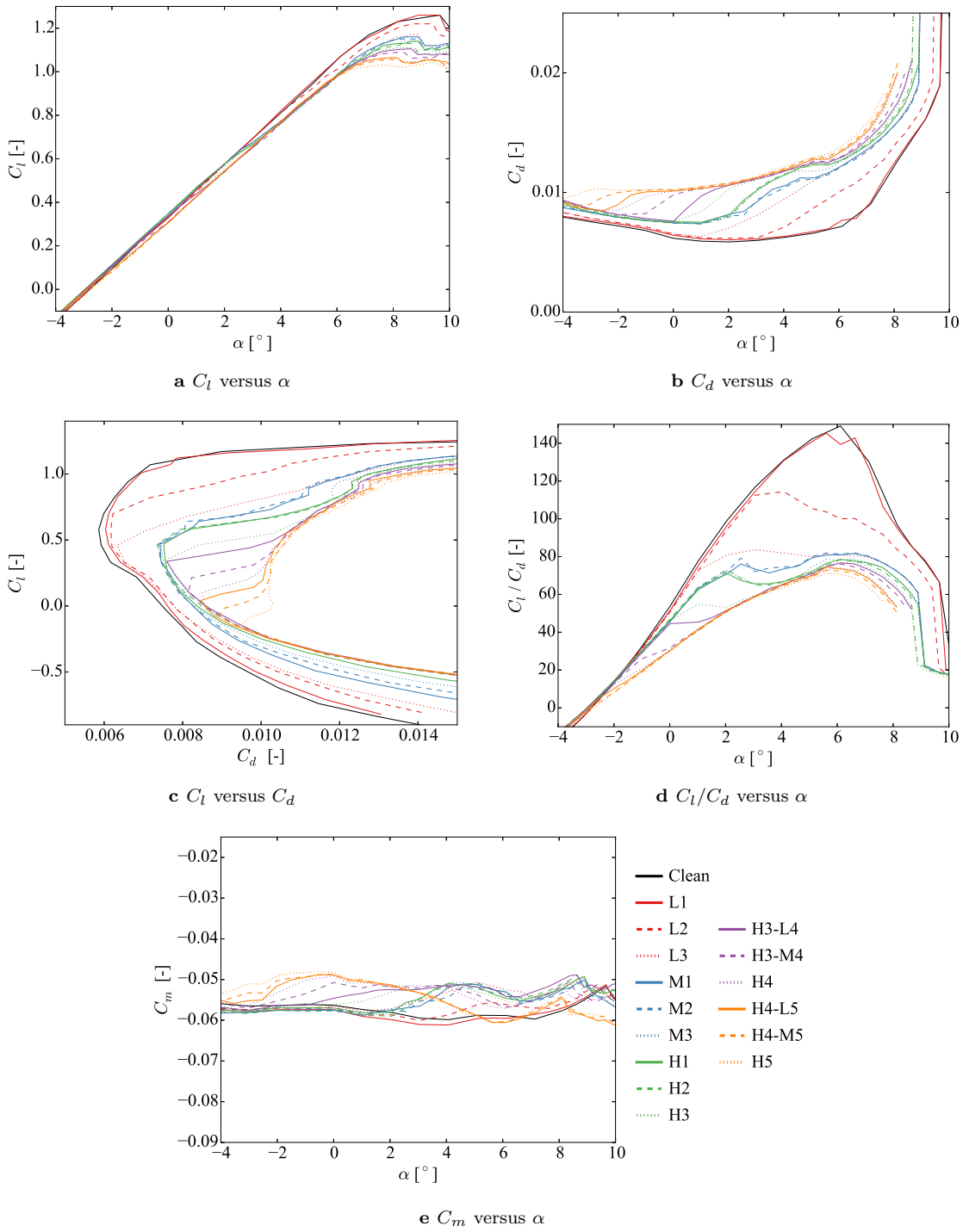

a C_l versus α

b C_d versus α

c C_l versus C_d

d C_l/C_d versus α

e C_m versus α

Figure 5.14: Aerodynamic performance for quick erosion and $Re = 6 \cdot 10^6$.

CHAPTER 6

Detachable leading edge

An airfoil was designed with a detachable leading edge (DLE), where the DLE was 3D printed to enable controlled surface shape modifications. The DLE model therefore was designed to incorporate three erosion levels, based upon the characteristics and statistical parameters from the RET specimens in Chapter 3. These three modelled erosion levels are called the light, medium and heavy DLE erosion. Furthermore a fourth erosion level was included to simulate delaminations in the glass lay-up (located in the random part of the mass loss curve). The airfoil profile itself was designed and manufactured by Rival.

The airfoil is a *DU-00-W212* profile, with 21.2 % thickness. A coupling mechanism was designed to attach the DLE to the airfoil model. The coupling of the DLE to the airfoil model results in a gap in spanwise direction, which should be as smooth as possible to avoid tripping of the flow.

In this chapter the design of the DLE, including the gap solution, 3D print material and pressure taps are explained. Subsequently the process of modelling the erosion at the leading edge surface is described, which is based upon the results of the RET erosion specimens. For each erosion level, this led to a coverage analysis and erosion generation based upon a Gaussian valley pattern. A statistical validation of the erosion patterns was performed using GOM Inspect, comparing the created erosion levels to the RET specimens. Finally the aerodynamic performance results for lift and drag are discussed.

6.1 Detachable leading edge design

The DLE model required initial dimensions in an early stage of the project, to facilitate the design and manufacturing of the airfoil from the very beginning. Therefore initial DLE dimensions were based upon an impact force study. A description of the coupling mechanism is given, including a solution to prevent a gap between the DLE and the airfoil itself. Also different 3D print materials were tested, to investigate which material and printing method would be sufficiently smooth and accurate to use for 3D erosion prints.

6.1.1 DLE dimensions

The dimensions of the DLE model should comply with the erosion coverage as determined in Section 3.4, ensuring that this coverage can actually be applied and therefore should have a leading edge surface larger than the erosion coverage. The erosion coverage study was performed at a later stage than the initial design of the DLE model and the airfoil, therefore an initial guess of coverage could not be determined from the RET specimens. To make an initial valid estimate of erosion coverage, an impact force study was performed.

The method is based upon estimating the impact force on the leading edge surface, which is given by (6.1) and also applied in the erosion studies by Keegan et al. (2013) [1] and Fiore et al. (2015) [22], to make an instantaneous approximation of the impact force. This estimation considers a rain droplet mass m_R and diameter d_R, the impact velocity on the surface U_R and the impingement angle between droplet and surface θ_R. It is assumed that impact velocity is equal to the rotational velocity in the tip section of the blade, as the terminal velocity of rain falling down is expected to be small compared to the rotational velocity of the blade. The impingement angle can be calculated from the tangent of the airfoil surface and assuming a uniform initial velocity of rain droplets, in x-direction

of the airfoil. With the impact distribution along the blade surface known, it can be concluded which area at the leading edge will be most critically affected by erosion.

An impact velocity of 100 $^{\mathrm{m}}/_{\mathrm{s}}$ was considered, resembling operational conditions in the tip section of a wind turbine blade. The mass of rain droplets is calculated following (6.2), taking the volume of a sphere and multiplying with the density of water at 1000 $^{\mathrm{kg}}/_{\mathrm{m}^3}$. The diameter of a rain droplet was set to be 3 mm. The impingement angle was computed from the tangent of airfoil profile coordinates and the set angle of attack.

$$F = m_R \cdot \frac{(U_R \cdot \sin\theta_R)}{d_R} \tag{6.1}$$

$$m_R = \frac{4}{3}\pi \left(\frac{d_R}{2}\right)^3 \rho_R \tag{6.2}$$

In Figure 6.1a the resulting impact force between $x = -4\,\%\mathrm{c}$ and $4\,\%\mathrm{c}$ is shown, for $\alpha = [-5, 0, 5, 12]°$. Negative x is on pressure side of the airfoil, whereas positive x is on the suction side. This shows that for increasing angles of attack the maximum impact force shifts towards the pressure side. This also shows that approximately 50 % of the impact force is taken between $x = -2\,\%\mathrm{c}$ and $2\,\%\mathrm{c}$. Assuming now that erosion would only occur in regions where the impact force is higher than half of the maximum impact force, there was assumed that erosion would only occur in the first two percent of chord distance.

Resultantly, this gives the initial dimensions for the DLE design, making it possible to design and manufacture the airfoil from an early design stage. The resulting cross-section of the DLE model is shown in Figure 6.1b, where 2% chord distance gives $x = 18$ mm for a 900 mm chord length airfoil profile. Also the spanwise length of the DLE models were determined, as one centre section of 100 mm and six side sections of 207 mm each to cover the full spanwise width of the airfoil model (which is 1350 mm in total). This results in a 4 mm gap on each side at the walls, to include a tolerance for placement of the DLE model to the airfoil.

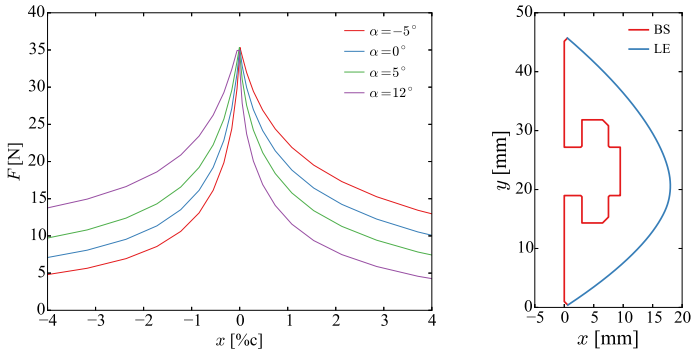

a Impact force **b** Cross-section DLE

Figure 6.1: Impact force on LE *DU-00-W212* airfoil, leading to sizing of DLE model.

6.1.2 Coupling and gap design

A coupling mechanism between DLE and airfoil was designed to enable interchanging of the DLE (for different erosion levels) while the airfoil profile itself remained installed inside the wind tunnel. In case the airfoil itself needed to be removed from the wind tunnel for changing the DLE, this would have led to increased testing time. The main feature of the coupling mechanism is a T-bar, where the different DLE sections can be slid onto. The T-bar includes different bolts which subsequently fit into the airfoil. These bolts can be tightened through holes which are located on the pressure side of the airfoil. Finally

the chamfered gap between DLE and airfoil, as well as the holes on pressure side, were filled with a two component plastic filler. A schematic drawing of the coupling mechanism is shown in Figure 6.2.

The chamfered gap was introduced between the DLE and airfoil, to make it possible to fully fill the gap with filler paste. This gap is 1 mm in x and in y direction. Dimensions of the backside (BS) of the DLE model to couple the T-bar, including the chamfered gap, are shown in Figure 6.1b.

Validation of this coupling system was performed as a coupling test in an early stage of the design phase. A symmetrical leading edge was 3D printed in different materials, to compare different 3D print materials as explained in Section 6.1.3. Also an aluminium block was manufactured with sides following the shape of the 3D prints. Subsequently the 3D print was coupled to this model and filled with filler paste. A surface scan was performed using a profilometer to measure the deviation between the CAD drawing and the model. This showed that the gap was negligible with deviations less than 10 μm. The profilometer scan is included in Appendix B.

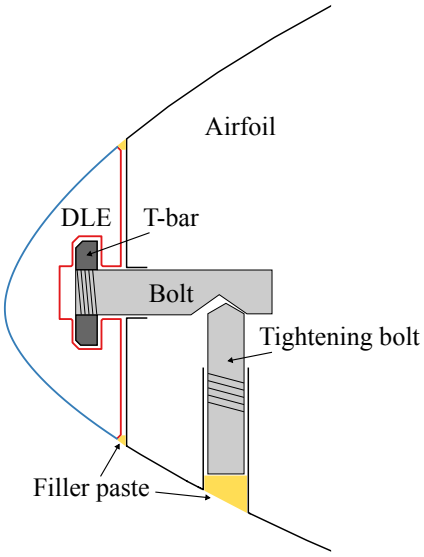

Figure 6.2: Schematic drawing of DLE coupling to airfoil profile.

6.1.3 DLE 3D print method

The DLE models were printed at Damvig. Together with the coupling test, different 3D printing technologies were tested, to investigate which solution would be best suited for printing of the erosion DLE models. Therefore the symmetrical DLE section as specified for the coupling tests, was printed using the following 3D printing methods. In total four DLE test prints with different technologies were tried, namely poly-jet lying down, selective laser sintering (SLS) standing up, stereolithography (SLA) lying down and SLA standing up. Prices followed the same order, where poly-jet is the cheapest and SLA standing up the most expensive. Requirements for the 3D prints were high accuracy and smooth surfaces. A rough surface would result in a disturbed flow and resultantly detrimental effect to aerodynamic performance.

The prints could either be printed standing up or lying down, where for poly-jet and SLS only standing up was possible due to printer dimension restrictions. Standing up builds layers in spanwise z-direction whereas lying down builds layers in x-direction, with the backside of the DLE model being the first layer.

Poly-jet uses multiple print heads to add liquid material layer by layer, where the material is cured while it is deposited. For the DLE models, only lying down printing possible. This resulted in clearly visible and touchable layers in spanwise direction, which would have a detrimental effect on the aerody-

namic performance. Standing up was not possible due to dimension restrictions of the poly-jet printer. Therefore this technology could not be used for the final DLE models.

Selective laser sintering (SLS) adds layers of powder material, where a laser sinters (without melting) the material. Here only standing up was tested, as lying down was expected to give poor results considering the layers in spanwise direction. The SLS technology resulted in a rough surface, probably caused due to the addition of powder material instead of using a liquid. Also the final manufacturing process of the print is applying a strong vibration, resulting in the surface to be smoothed. This smoothing of surface cannot be applied to modelled erosion surfaces, as the modelled erosion surface should be printed as accurate as possible and no smoothing is allowed.

Finally stereolithography (SLA) adds a liquid polymer, where an ultraviolet laser solidifies the material layer by layer. Expected to be the most accurate solution, both a test print was done standing up and lying down. This because printing standing up was more expensive than printing lying down. In the end no differences were observed in touch and feel. The surface was smooth and no spanwise layers were visible. Therefore it was concluded that SLA standing up is the most suitable and accurate solution for printing the erosion DLE models.

Also the surface roughness impact of the material to aerodynamic performance was validated by performing wind tunnel tests on a clean printed DLE model, as described in Section 6.4.1.

6.1.4 Pressure taps

To enable lift measurements from the pressure distribution, pressure taps were included in the design of the airfoil and the DLE model. The pressure taps in the DLE model were designed and manufactured in a DLE aluminium centre section of 100 mm in spanwise direction. While performing the erosion DLE experiments, the uneroded aluminium centre piece (with pressure taps) would need to be placed instead of an eroded 3D printed centre section. The pressure tap distribution in the DLE airfoil model is shown in Figure 6.3, where the taps in the first 2 %c are located in the DLE. Lift measurements from pressure taps were validated as explained in Section 6.4.1. Based upon this validation a choice was made if lift would be measured from pressure taps or by using the load cells.

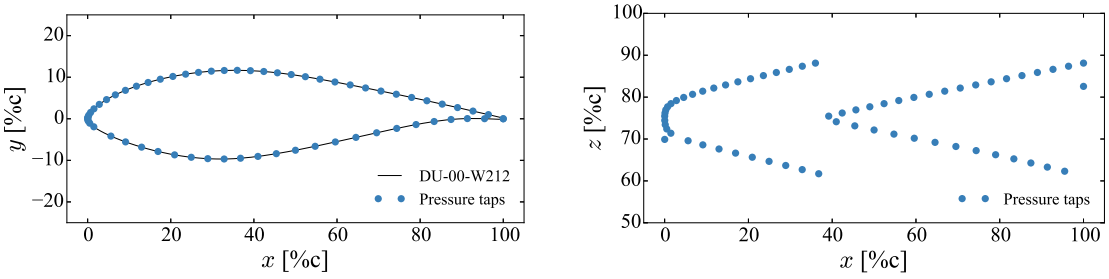

a x versus y coordinates

b x versus z coordinates

Figure 6.3: Pressure tap distribution DLE airfoil model.

6.2 DLE erosion model

In this section the modelling of the erosion pattern in the DLE is described. Three different erosion levels were modelled, based upon the statistics and characteristics of the RET specimens. Therefore, these three modelled erosion patterns are light, medium and heavy erosion, corresponding to Phase 1, Phase 2 and Phase 3 eroded RET specimens. Furthermore, a fourth pattern was created, simulating breakthrough and delaminations of the glass lay-up. This heavy-delamination pattern initially is the same as the heavy erosion pattern, only relatively deeper and wider valleys are added on top of the heavy erosion pattern directly at the leading edge.

Since it is assumed that testing conditions in the LSWT at $Re = 6 \cdot 10^6$ are similar to operating conditions, and characteristics derived from the RET specimens are resembling erosion patterns as seen on operating wind turbine blades, there is no need for scaling of erosion depths. In previous erosion studies such as by White et al. (2011) [6], Sareen et al. (2013) [9], Ehrmann et al. (2013) [10] and Gaudern (2014) [5], erosion depth or height was scaled down based upon boundary layer roughness theorem. As this scaling method introduces uncertainties and assumptions, whereas valley depth is considered to be a main parameter characterizing the erosion patterns, it is expected that modelling and testing erosion depths at operating conditions without any necessary scaling will give more realistic results.

Modelling of the erosion pattern follows the method of creating overlapping 3D Gaussian valleys, where the location of valleys is based upon valley distance parameters from the RET specimens, the width of valleys is based upon the width parameters and a resulting depth should match the valley depth parameters. Erosion generation led to the creation of a point cloud, where the eroded leading edge surface of the DLE model is described in (X, Y, Z) coordinates. Using Meshlab the point cloud could be triangulated resulting in a surface reconstruction, which could be inserted into Blender to create the final printable DLE model.

A flowchart of the modelling process for the complete DLE model is shown in Figure 6.4, where each step is described in this section. The flowchart also includes a summary of the statistical analysis on the RET specimens as well as how these act as an input to the DLE erosion model.

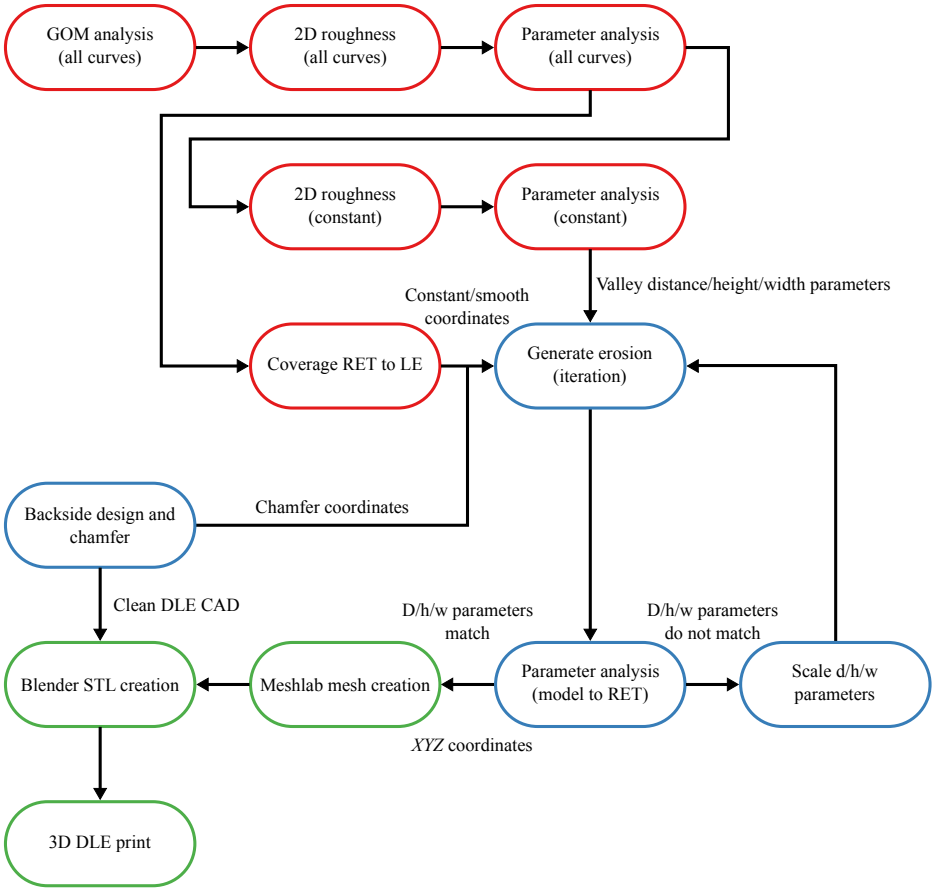

Figure 6.4: Flowchart of DLE model as based upon RET erosion specimens. In red the statistical analysis of the RET specimens is summarized, leading to erosion generation in blue and finalizing the DLE model in green.

6.2.1 Coverage

Coverage and smoothing areas were based upon the angle study for the RET specimens as explained in Section 3.4. Constant and smoothed erosion areas should be located between the points where the DLE surface matches angles as found for the RET specimens. This method is based upon the geometric impact angle of the rain droplets compared to the leading edge surface, assuming that droplets would hit the airfoil parallel with x-direction. The coverage therefore will also depend on the angle of attack of the airfoil. A conservative assumption was taken stating that during the lifetime of a wind turbine, the blade is operating between zero and twelve degrees. Now combining the coverage areas for these two angles of attack, led to the erosion coverage as applied to the DLE model.

The modelled coverage for constant and smoothed erosion for light, medium and heavy erosion is shown in Figure 6.5. This is also shown for $\alpha = 0°$ and 12°, resulting in the combined erosion coverage. Light and medium erosion show the same coverage, since their coverage angles are the same as stated in Table 3.3. Also there can be seen that the constant area for heavy erosion is smaller than for light and medium erosion, which complies with the RET Phase 3 erosion pattern. The heavy-delamination coverage is not shown as this will be the same coverage as for the heavy erosion pattern in Figure 6.5c.

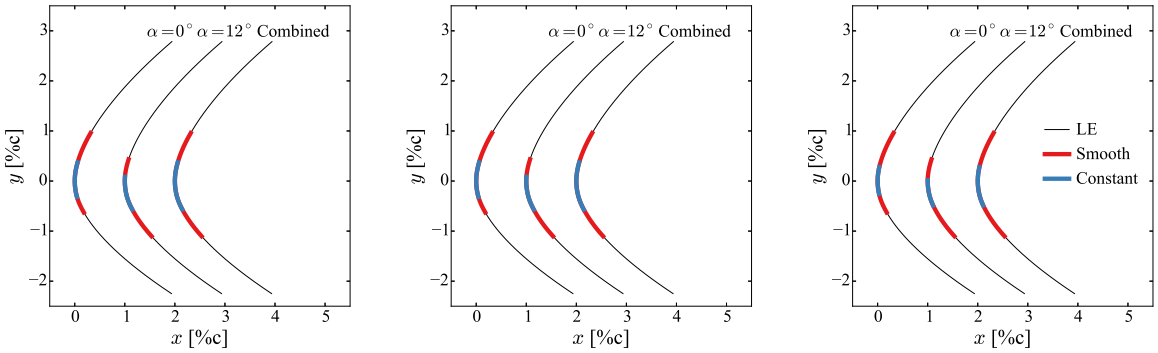

a Light **b** Medium **c** Heavy

Figure 6.5: Coverage of light, medium and heavy erosion for the DLE model, at $\alpha = [0, 12]°$ and combined.

6.2.2 Generate erosion

In this section the modelling of the erosion pattern is described, based upon the generation of overlapping 3D Gaussian valleys. At first, valley coordinates were created, describing the origins of the Gaussian valleys. These valley coordinates were based upon the average and standard deviation of valley distances as found for the Phase 1 (light), Phase 2 (medium) and Phase 3 (heavy) eroded RET specimens. For each coordinate, a 3D Gaussian valley was modelled having its origin at this particular coordinate. Creation of the 3D Gaussian valleys was based upon the average and standard deviation of valley widths as taken from the RET specimens. Neighbouring Gaussian valleys potentially overlap each other, therefore in the end the minimum value for depth of all the overlapping Gaussian valleys was taken to create the eroded pattern.

After creation of an erosion pattern, a statistical analysis was performed to find the average and standard deviation for valley depth, distance and width parameters. An initial creation of the erosion pattern was based upon valley distance and width parameters. This resulted in an output for erosion depths, which needed to be scaled to comply with the depth parameters as found for the RET specimens. Also the valley distance input parameter required additional scaling to match with the RET specimens. An explanation is included of how this scaling and iteration of the valley distance input parameter and valley depth output was performed.

With light, medium and heavy erosion patterns created, the correct DLE surface dimensions were extracted from the erosion pattern. This would result in the leading edge being completely eroded, therefore coverage area of constant and smoothed erosion as found in Section 6.2.1 needed to be applied. The final step of the erosion generation is the folding of the erosion pattern coordinates to the DLE (X, Y, Z) coordinates.

The flowchart of erosion generation is shown in Figure 6.6, where each step is described in this section. This erosion generation flowchart therefore describes the blue erosion generation block in Figure 6.4.

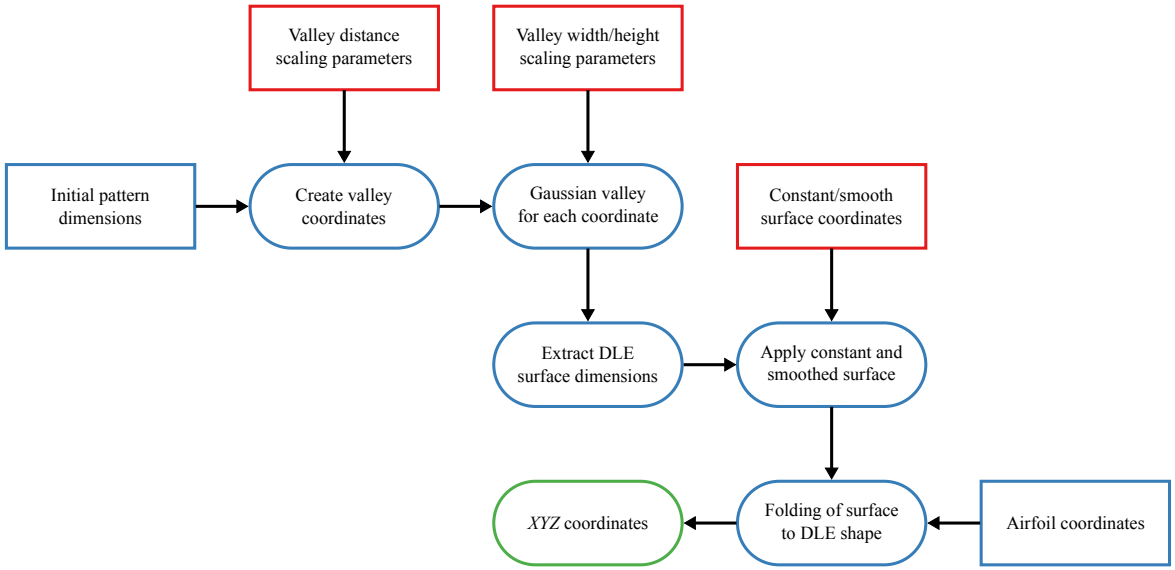

Figure 6.6: Flowchart of erosion generation. Inputs are shown as squared boxes, with in red the parameters from the RET specimens, leading to erosion generation in blue and finalizing the DLE model in green.

6.2.2.1 Coordinates of valleys

The first step for erosion generation is the creation of random valley coordinates, where the coordinates have certain z and y distances in between. These distances in z and y direction follow from a random normal distribution, which requires an inout for average and standard deviation. Using PYTHON the NUMPY RANDOM NORMAL tool computed random distances from a normal (Guassian) distribution.

As an input to compute the distance in z and y direction, the average and standard deviation distance parameters μ_{z_μ} and σ_{z_μ} were taken from the RET specimens as stated in Table 3.4. Light erosion used the Phase 1 parameters, medium used Phase 2 and heavy erosion used the Phase 3 parameters.

For heavy-delamination, coordinates were taken with distance parameters only in z-direction with an average of 15 mm and a standard deviation of 0.1 mm. This because only one row of deep valleys was created in z-direction at the leading edge. Subsequently the valleys created at these coordinates were placed on top of the heavy erosion pattern.

In Figure 6.7 the initial valley coordinates are shown for light, medium and heavy erosion. This shows a close-up of 20 mm by 10 mm, whereas the original pattern measured 220 mm by 75 mm. Here distances were not scaled and followed directly from the input parameters from the RET specimens. As now distances in two directions were given (both in z and y-direction), distances in only z-direction become larger compared to the average valley distance (in z-direction) for the RET specimens. Therefore downscaling of distance parameters was required.

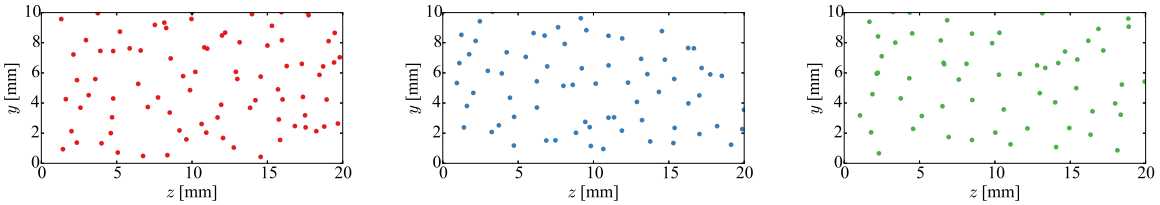

a Light **b** Medium **c** Heavy

Figure 6.7: Initial coordinates light, medium and heavy erosion, before scaling. Close-up of 20 mm by 10 mm.

6.2.2.2 Gaussian valley creation

The next step is to create a 3D Gaussian valley in each coordinate. Now in PYTHON the MATPLOTLIB BIVARIATE NORMAL tool was used, which fits a bivariate Gaussian distribution in a coordinate field. Therefore for each valley coordinate a coordinate field (Z, Y) was created having the initial pattern dimensions, and having a Gaussian valley originated at this valley coordinate.

The function for the bivariate normal distribution is shown in (6.3), where $\rho_{Z,Y}$ is the correlation coefficient between Z and Y as shown in (6.4). This function leads to a distribution for two jointly normal distributions, where z and y describe the coordinate field (Z, Y). For each valley coordinate from Section 6.2.2.1 a different coordinate field was created, with shifts in z and y depending on the valley coordinates.

Other inputs are the mean values of the bivariate Gaussian distribution, namely μ_Z and μ_Y. As these values describe the origin of the Gaussian valley, these values were set to zero. This because each valley should originate in its valley coordinate, and should not be shifted from this location. The location of the valleys is already included in the creation of the coordinate field (Z, Y).

Final input parameters to the bivariate distribution are the standard deviations in z and y-direction. These values describe the width of the Gaussian valley created, in corresponding z and y-direction. Assumed is that the erosion valleys in the RET specimens are circular shaped, and therefore the width parameters of the RET specimens were taken to describe the widths (standard deviations) of the created Gaussian valleys in both z and y-direction. Therefore for σ_Z and σ_Y random values were computed from a normal distribution using the NUMPY RANDOM NORMAL tool, having as an input the average and standard deviation of sigma Gaussian fits of the RET specimens as stated in Table 3.4. As Gaussian valleys are circular, for each individual valley σ_Z and σ_Y were set to be equal.

$$x(z,y) = \frac{1}{2\pi\sigma_Z\sigma_Y\sqrt{1-\rho_{Z,Y}^2}} \exp\left(-\frac{1}{2\left(1-\rho_{Z,Y}^2\right)}\left[\frac{(z-\mu_Z)^2}{\sigma_Z^2} + \frac{\left(y-\mu_Y^2\right)}{\sigma_Y^2} - \frac{2\rho\,(z-\mu_Z)\,(y-\mu_Y)}{\sigma_Z\sigma_Y}\right]\right) \tag{6.3}$$

$$\rho_{Z,Y} = \mathrm{cor}\,(Z,Y) = \frac{\mathrm{cov}\,(Z,Y)}{\sigma_Z\sigma_Y} \tag{6.4}$$

As a Gaussian valley is created at each coordinate, neighbouring valleys potentially overlap. Therefore the minimum x values of overlapping Gaussian valleys were taken, leading to the final erosion pattern. A close-up of the initial unscaled erosion patterns for light, medium and heavy erosion is shown as a contour plot in Figure 6.8. This shows that distances between valleys should decrease to better resemble an eroded surface.

The erosion pattern now could be created directly based upon valley distance and width parameters from the RET specimens. The height is the output of (6.3), and should be scaled accordingly to match with the height parameters of the RET specimens. This also follows from Figure 6.8, where valley depths exceed 1 mm and do not match with RET depth parameters from Table 3.4.

A statistical analysis was performed on the erosion patterns by extracting 2D roughness curves in z-direction. This led to an output for average and standard deviations of valley depth, distance and width parameters. These subsequently could be compared to the parameters of the RET specimens in Table 3.4, also showing that depth and distance parameters are too high for generated erosion patterns compared to the RET specimens. Therefore in Section 6.2.2.3 a scaling method is described how the depths and distances were downscaled. Valley width parameters appear to be in the same range of RET specimens, and therefore scaling for valley width was not necessary.

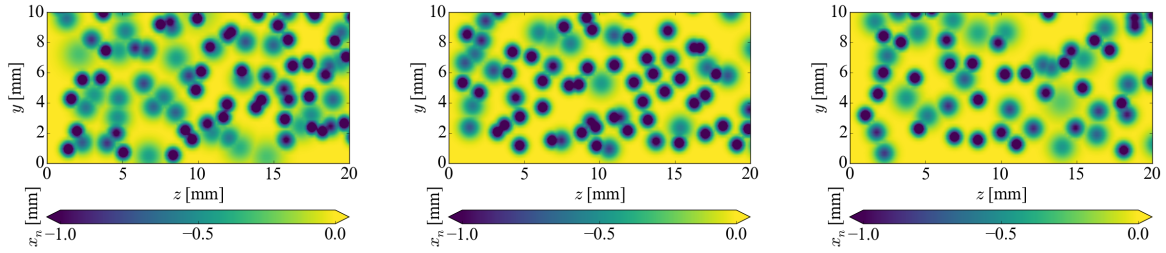

a Light **b** Medium **c** Heavy

Figure 6.8: Initial Gaussian valleys pattern light, medium and heavy erosion, before scaling. Close-up of 20 mm by 10 mm.

Table 6.1: Average and standard deviation of valley depth, distance and width parameters, for DLE erosion before scaling.

	Valley depth		Valley distance		Valley width	
Level	$\mu_{x_{n,\mu}}$ [mm]	$\sigma_{x_{n,\mu}}$ [mm]	μ_{z_μ} [mm]	σ_{z_μ} [mm]	μ_{z_σ} [mm]	σ_{z_σ} [mm]
Light	-0.727	0.476	2.53	1.24	0.360	0.151
Medium	-0.835	0.517	2.66	1.15	0.538	0.450
Heavy	-0.708	0.469	2.72	1.25	0.443	0.149

6.2.2.3 Scaling of input parameters

When the initial erosion patterns were created, it was clear that the distance and height needed to be scaled to ensure these two main parameters also matched with the RET parameters. Therefore the average distance parameters as an input was scaled down, as well as the output for height x_n of the Gaussian valleys following from the bivariate normal equation (6.3). An iteration of downscaling was performed until the average of valley depth and average distance parameters were in the same range as for the RET specimens in Table 3.4. To obtain these statistical parameters, 2D roughness curves were extracted from the DLE erosion patterns and a statistical analysis as explain in Section 3.3.3 was applied. The input parameter for valley width did not require scaling, as for the initial erosion patterns the average valley width following from the statistical analysis already matched with the RET specimens.

In Table 6.2 the scaling parameters are shown for the output of depth and the inputs for average distance and average width. This led to the final statistical parameters (after scaling) for light, medium and heavy erosion as stated in Table 6.3. Now the average for valley depth is close to the values of the RET specimens. For medium and heavy erosion, the average depth is approximately 30 % higher than for Phase 2 and Phase 3 RET erosion. Still a distinct increase in depth between light, medium and heavy erosion is created, expected to give significant differences while tested for aerodynamic performance. Also erosion depth for light and medium erosion still perturbs only into the gel-coat (assuming the 400 μm gel-coat thickness). Heavy erosion therefore resembles erosion perturbing into

the glass lay-up. The heavy-delamination pattern up-scaled the depth output with 130, to reach erosion depths of approximately 3 mm perturbing deep into the glass lay-up.

The valley distance parameters following from the statistical analysis are also approximately 30 % higher for the DLE erosion patterns compared to the RET specimens. To save computational time there was decided to not further decrease the valley distance. Smaller distances between valleys requires more valleys to be computed in total, increasing the computational time significantly. Also it is expected that valley distance is less critical than reached valley depths, where valley depth compared to boundary layer thickness is likely to cause more harm. Also valley distances are influenced by threshold settings while finding the individual valleys as explain in Section 5.3, leading to a difference.

The resulting contour plots for light, medium, heavy and delamination after scaling are shown in Figure 6.9, clearly showing the valley distance being decreased from the initial patterns as shown in Figure 6.7. The heavy-delamination pattern in Figure 6.9d only shows the valleys for the delamination, which for the final pattern were added to the heavy erosion pattern. Finally 2D roughness curves for light, medium, heavy and heavy-delamination DLE erosion are shown in Figure 6.10. On these curves a statistical analysis could be performed leading to the valley depth, distance and width parameters. In Figure 6.9d the combination of the delamination valleys with the heavy erosion pattern can be seen, leading to the heavy-delamination pattern.

Table 6.2: Scaling parameters for depth output and distance input to create light, medium and heavy erosion patterns.

	Depth (output)	Distance (input)	Width (input)
Level	x_n	μ_{z_μ}	μ_{z_σ}
Light	0.05	0.25	1
Medium	0.25	0.25	1
Heavy	0.50	0.25	1
Heavy-delam	130	1	1

Table 6.3: Average and standard deviation of valley depth, distance and width parameters, for DLE erosion after scaling.

	Valley depth		Valley distance		Valley width	
Level	$\mu_{x_{n,\mu}}$ [mm]	$\sigma_{x_{n,\mu}}$ [mm]	μ_{z_μ} [mm]	σ_{z_μ} [mm]	μ_{z_σ} [mm]	σ_{z_σ} [mm]
Light	-0.0822	0.007	1.97	0.546	0.385	0.173
Medium	-0.389	0.0624	1.96	0.441	0.569	0.235
Heavy	-0.716	0.163	1.65	0.594	0.609	0.202

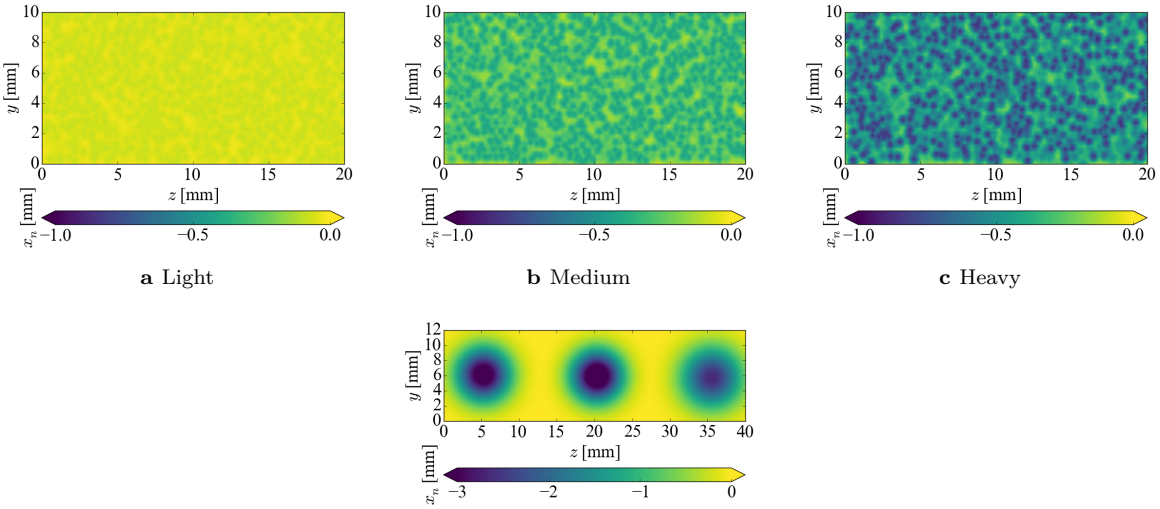

a Light **b** Medium **c** Heavy

d Heavy-delamination

Figure 6.9: Scaled Gaussian valleys pattern for light, medium, heavy and delamination erosion, after scaling. Delamination only shows the delamination valleys, the final heavy-delamination pattern is a combination of heavy and delamination. Close-up of 20 mm by 10 mm.

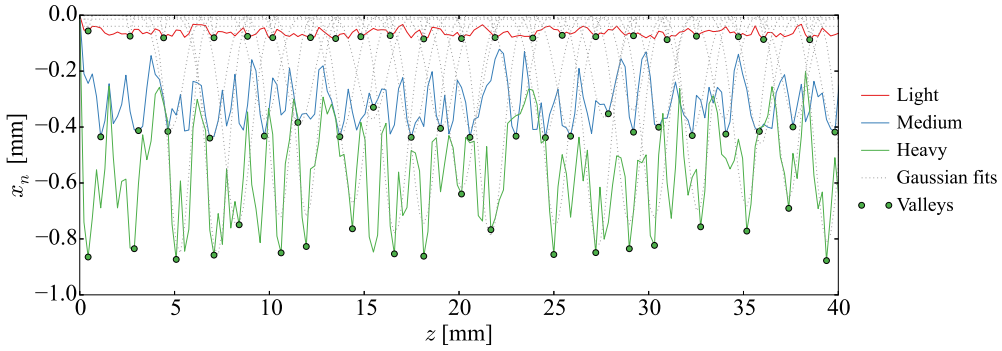

a Light, medium and heavy erosion. Includes the Gaussian fits required for statistical analysis.

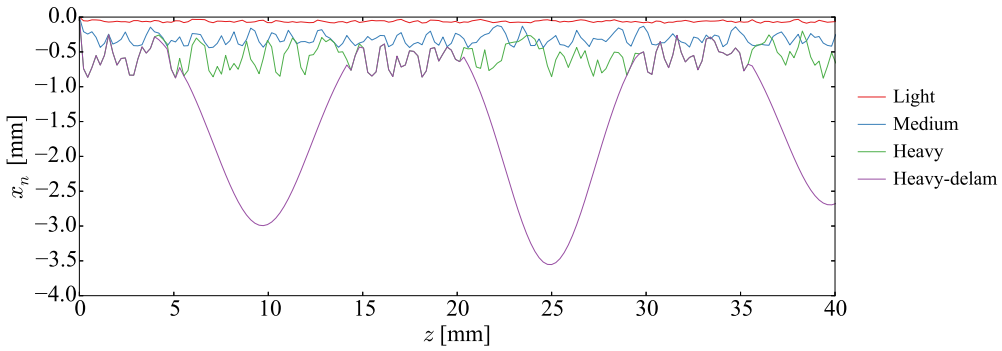

b Light, medium, heavy and heavy-delamination erosion.

Figure 6.10: 2D roughness curves of scaled Gaussian valleys pattern for light, medium, heavy and heavy-delamination erosion, after scaling.

6.2.2.4 Extract DLE surface dimensions

The scaled erosion patterns measure 220 mm in z-direction and 75 mm in y-direction. The DLE sections measure $z = 204\,\text{mm}$ (or 100 mm for the centre section) and have a leading edge surface length of $y_s = 58.9\,\text{mm}$. Therefore these dimensions were extracted from the scaled roughness patterns. This led to erosion patterns in x_n as normal to surface distance, y_s as surface distance and z as distance in spanwise direction, where the erosion covered the entire leading edge surface of the DLE model.

6.2.2.5 Application of coverage and smoothing

The erosion pattern now covers the complete leading edge surface. Therefore the next step is to apply the smoothed and constant erosion coverage regions as stated in Figure 6.5. As the surface distance y_s is equal of the erosion patterns to the surface distance of the DLE model, distances (originating at zero, therefore at the bottom of the DLE model) for constant and smoothed erosion areas were the same. The constant area keeps the original x_n values, whereas in the smoothed area the erosion depth x_n linearly decreases to zero. Outside of the constant and smoothed areas, x_n was set to zero (no erosion). The result of the coverage and smoothing application is shown as contour plots in Figure 6.11, for light, medium and heavy erosion. This is the final erosion pattern, in (x_n, y_s, z) coordinates.

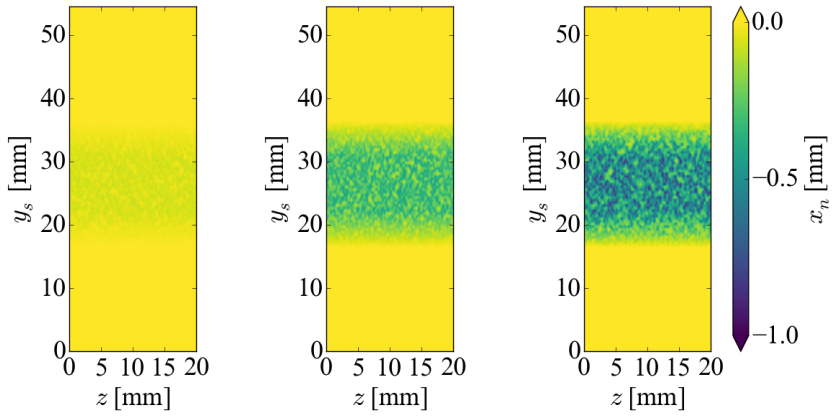

a Light **b** Medium **c** Heavy

Figure 6.11: Final Gaussian valleys pattern for light, medium and heavy erosion, after smoothing.

6.2.2.6 Folding to DLE and transformation to XYZ coordinates

Erosion patterns are now described as (x_n, y_s, z) coordinates and should be folded to the shape of the leading edge of the DLE model, as the (x_n, y_s, z) coordinates does not follow this shape. The shape of the DLE leading edge is governed by the first 2 %c of the airfoil profile coordinates, as well as the DLE dimensions and the gap chamfer as described in Section 6.1.2. In this section is explained how the erosion pattern coordinates were transformed and folded to the DLE leading edge coordinates. In Figure 6.12 a schematic drawing of the erosion pattern coordinates (x_n, y_s, z) and the DLE coordinates (X, Y, Z) is shown, where x_n is the normal to surface height, y_s is the surface distance and z is the spanwise distance.

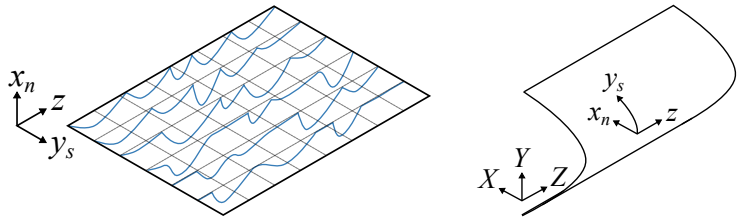

a Erosion pattern (unfolded) **b** DLE coordinates (folded)

Figure 6.12: Transformation of coordinate systems of erosion pattern in (x_n, y_s, z) to DLE (X, Y, Z) coordinates.

The x_n, y_s and z pattern coordinates need to be transformed to X, Y and Z coordinates. First of all the spanwise distance coordinates are equal and should not be transformed, therefore Z is set to z (6.5).

$$Z = z \tag{6.5}$$

The coordinate transformation was performed in three steps. In the first step the normal to surface directions of the airfoil coordinates φ_{af} were computed. Therefore the normal to surface direction φ_{af} from the airfoil coordinates x_{af} and y_{af} were computed, as shown in Figure 6.13a and leading to (6.6). This led to a normal to surface direction φ_{af} corresponding to an airfoil surface length $y_{s,af}$.

$$\varphi_{af_i} = 90° - \arctan\left(\frac{y_{af_{i+1}} - y_{af_{i-1}}}{x_{af_{i+1}} - x_{af_{i-1}}}\right) \tag{6.6}$$

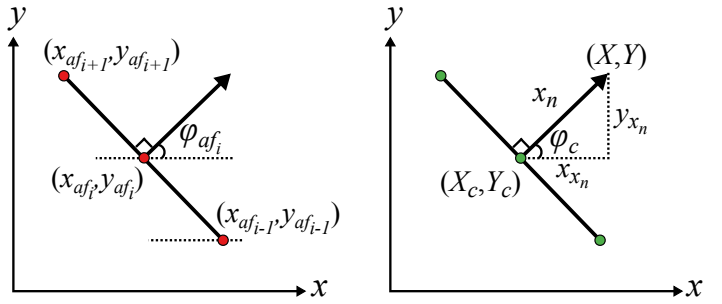

a Airfoil normal to surface direction **b** Clean to eroded DLE transformation

Figure 6.13: Computation of airfoil normal to surface direction, leading to transformation from clean (X_c, Y_c) to eroded (X, Y) DLE coordinates.

Second step is the interpolation between airfoil surface lengths $(y_{s,af})$ and corresponding normal to surface directions φ_{af} and airfoil coordinates (x_{af}, y_{af}), resulting in intermediate normal to surface directions φ_c and clean DLE coordinates (X_c, Y_c) corresponding to the clean DLE surface lengths $(y_{s,c})$.

The total surface length of the modelled erosion pattern $y_{s,p}$ and the total surface length of leading edge of the airfoil are the same $y_{s,af}$. Still modelling the erosion pattern led to a higher number of points in surface length for the erosion pattern $y_{s,p}$ than for the surface length of the airfoil leading edge $y_{s,af}$. This because a higher resolution for the modelled erosion resulted in a more detailed pattern, describing the erosion features accurately. A different resolution for $y_{s,p}$ and $y_{s,af}$ required an interpolation between surface lengths to compute intermediate values for normal to surface direction φ_c and clean DLE coordinates (X_c, Y_c).

The interpolations to compute X_c, Y_c and φ_c were computed as linear interpolations using the Python Scipy interpolate interp1d function and its inputs and outputs are shown in Figure 6.14. The sample points are the airfoil surface distances $y_{s,af}$ and have corresponding values for either x_{af}, y_{af} and φ_c. Intermediate values are the query points for eroded pattern or clean DLE surface lengths as $y_{s,p} = y_{s,c}$. This led to an output for corresponding clean uneroded DLE coordinates X_c and Y_c as well as normal to surface directions φ_c.

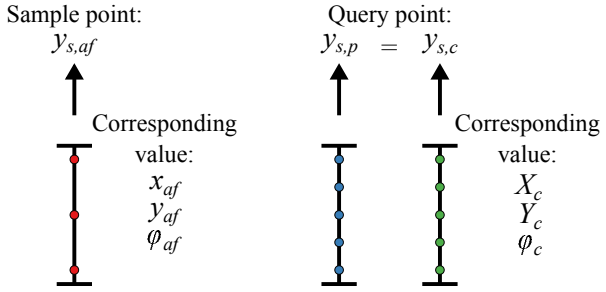

Figure 6.14: Linear interpolation leading to (X_c, Y_c) coordinates and normal to surface direction φ_c for the uneroded (clean) LE. Inputs are the airfoil coordinates (x_{af}, y_{af}) and airfoil normal to surface direction φ_{af}, as well as the DLE surface distances $Y_{s,c}$.

In the third and final step, the normal to surface erosion depth x_n was applied, leading to eroded DLE coordinates (X, Y). This required the normal to surface direction φ_c of the clean DLE coordinates (corresponding to clean DLE surface lengths $y_{s,c}$). This final transformation of clean to eroded DLE coordinates is also shown in Figure 6.13b, where the erosion depth x_n is composed of an x and y component that together with surface direction φ_c resulted in the eroded DLE coordinates. These x and y components are stated as x_{x_n} and y_{x_n} in (6.7) and (6.8). Adding these components to the clean DLE coordinates as shown in (6.9) and (6.10), together with (6.5), led to the final eroded DLE coordinates (X, Y, Z). The result of the folding process is shown as eroded DLE (X, Y, Z) coordinates for medium erosion in Figure 6.15. Subsequently coordinates were saved as an XYZ-file, making it possible to load these coordinates into Meshlab.

$$x_{x_n} = x_n \cos(\varphi_c) \tag{6.7}$$

$$y_{x_n} = x_n \sin(\varphi_c) \tag{6.8}$$

$$X = X_c + x_{x_n} \tag{6.9}$$

$$Y = Y_c + y_{x_n} \tag{6.10}$$

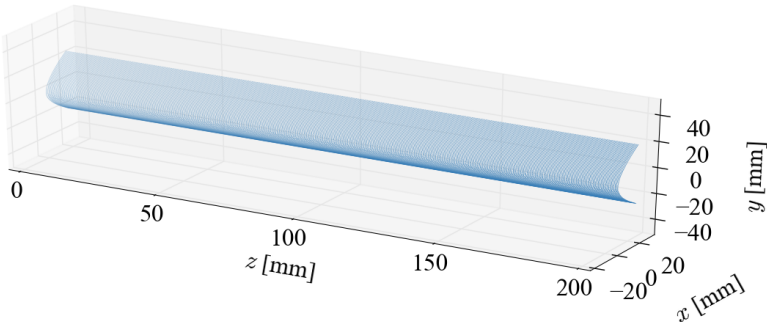

Figure 6.15: Coordinates of LE for medium erosion, after folding.

6.2.3 3D STL model

Finalizing the 3D DLE model was done using two open-source software systems. Using MESHLAB the (XYZ) coordinates of the eroded DLE leading edge surface could be processed to a 3D triangular mesh. After creating the mesh, the 3D STL model could be created using BLENDER.

6.2.3.1 Mesh generation: MESHLAB

In MESHLAB first the point cloud was oriented by computing the normals for the (XYZ) coordinates. After computing the normals, a remeshing tool was used to create a triangular mesh. This remeshing tool is called the screened Poisson surface reconstruction tool, creating a watertight surface from an orientated point set [23]. The result of this surface reconstruction is shown for heavy erosion in Figure 6.16. This shows that the triangular mesh is larger than the original point cloud surface (visible as the grey extruded boundaries versus the green original surface). The original coordinate point cloud is not closed, whereas the Poisson surface reconstruction tool tries to close the surface. This leads to extruded borders, which do not cause any problems as the mesh will be modified in BLENDER. Finally the mesh was saved as a Stanford Polygon File (PLY) file .

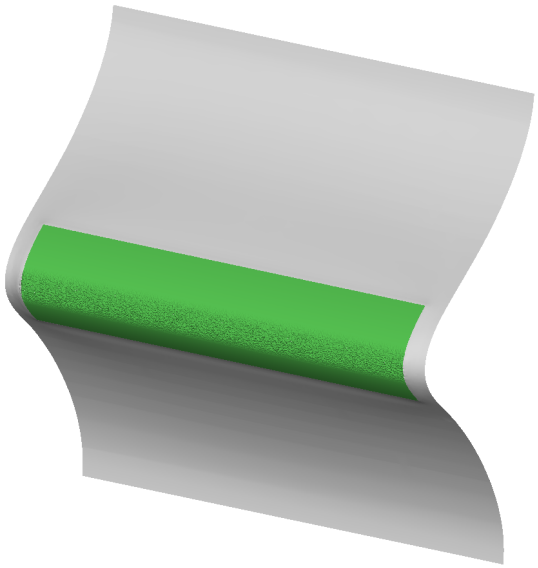

Figure 6.16: Mesh of DLE for heavy erosion, after Poisson surface reconstruction in MESHLAB.

6.2.3.2 STL generation: BLENDER

In BLENDER the triangulated mesh was imported (as created in MESHLAB). The mesh was extruded for 5 mm in x-direction, this to solidify the mesh. A solid mesh was required to apply Boolean operators to two different meshes.

Secondly the cross-section of the clean DLE model was imported, and extruded in z-direction (either 204 mm or 100 mm depending on a normal or centre DLE section). This led to a solid uneroded clean DLE mesh. As the eroded mesh and clean DLE model were created in the same coordinate system, no further transformation was required.

Therefore the solid clean DLE model and the solid eroded mesh overlap each other. By applying a Boolean modifier as a difference operation, the difference between the clean DLE model and the eroded mesh was computed. This resulted in a solid DLE model including the eroded surface at the leading edge. Also the difference operation automatically resulted in a removal of the extruded boundaries of the erosion mesh (resulting from the surface reconstruction).

To become a 3D printable stereolithography (STL) file, the model should be a manifold, which in theory means it should be water tight. Therefore in Blender the geometry was inspected for being a solid, ensuring no gaps in the mesh were present. The final results of STL model creation are shown in Figure 6.17, for light, medium, heavy and heavy-delamination erosion, as 30 mm sections in z-direction.

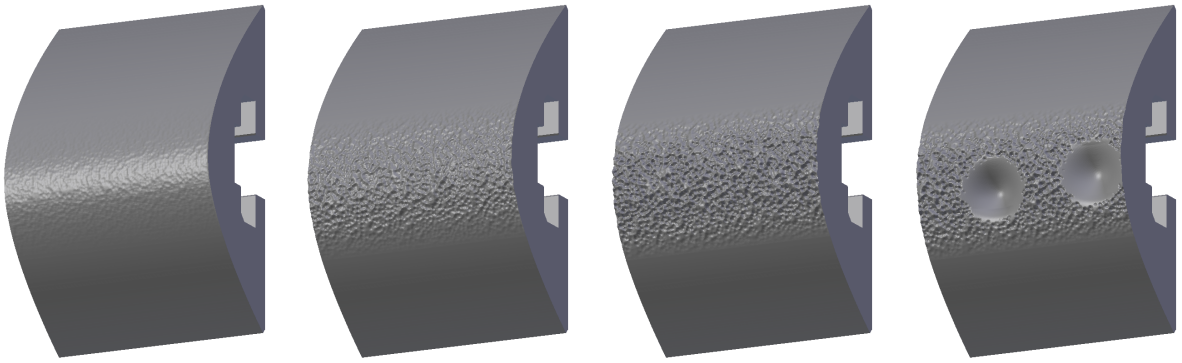

a Light **b** Medium **c** Heavy **d** Heavy-delamination

Figure 6.17: Final DLE models for light, medium, heavy and delamination erosion, as constructed in Blender. For visualisation each section is 30 mm in spanwise z-direction.

6.3 Statistical validation erosion DLE to RET

After the folding process, the surface construction in Meshlab and STL model creation in Blender, a validation was performed to analyse of the statistical parameters for the three modelled erosion levels were still matching the parameters of the RET specimens. Therefore the 3D STL models were imported into the GOM Inspect software, as well as a clean uneroded DLE model. Following the same process as in Section 3.3, 2D roughness curves could be extracted and a statistical analysis was applied to these curves. This led to the statistical parameters for valley depth, distance and width, which were compared with the RET parameters.

No statistical analysis was performed on the heavy-delamination level, as this consists of the heavy erosion pattern and delamination features itself cannot be compared to the RET specimens.

6.3.1 Surface inspection

After importing the eroded and uneroded DLE models into GOM Inspect, no alignment was required as both were modelled in the same coordinate system. The surface inspections on the eroded DLE models are shown in Figure 6.18, including highlighted location where 2D roughness curves were extracted.

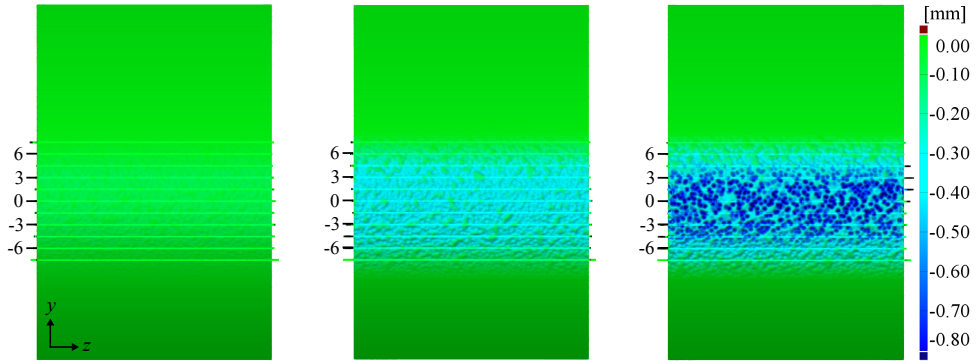

a Light **b** Medium **c** Heavy

Figure 6.18: Surface inspection of light, medium and heavy DLE erosion, with eleven sections for extracted 2D curves highlighted (spacing between sections is 1.5 mm).

6.3.2 Surface roughness parameters

From the surface inspection maps, 2D roughness curves were extracted. In contrast to the RET specimens in Section 3.3.2.3, the 2D roughness curves were not shifted with highest peaks to zero, as erosion was modelled without any normal to surface height pointing outwards of the model. Subsequently on these 2D roughness curves a statistical analysis was performed to compute the statistical parameters for valley depth, distance and width.

In Figure 6.19 the average of valley depth, distance and width parameters is shown for each extracted 2D roughness curve. All other statistical parameters are included in Appendix C. From Figure 6.19a constant and smoothed areas are visible for valley depths. The results for the main three statistical parameters within the constant region are stated in Table 6.4. Maximum deviations for valley depths and width are within 20 % compared to the parameters extracted from the erosion patterns in Table 6.3 and therefore are assumed to still match well with the RET specimen parameters, with medium erosion depth at 0.340 μm still considered to be perturbing only into the gel-coat. Only the valley distances are up to 60 % smaller as compared to the erosion pattern parameters in Table 6.3. This could again be a result of difference in threshold setting for minimum distance between valleys.

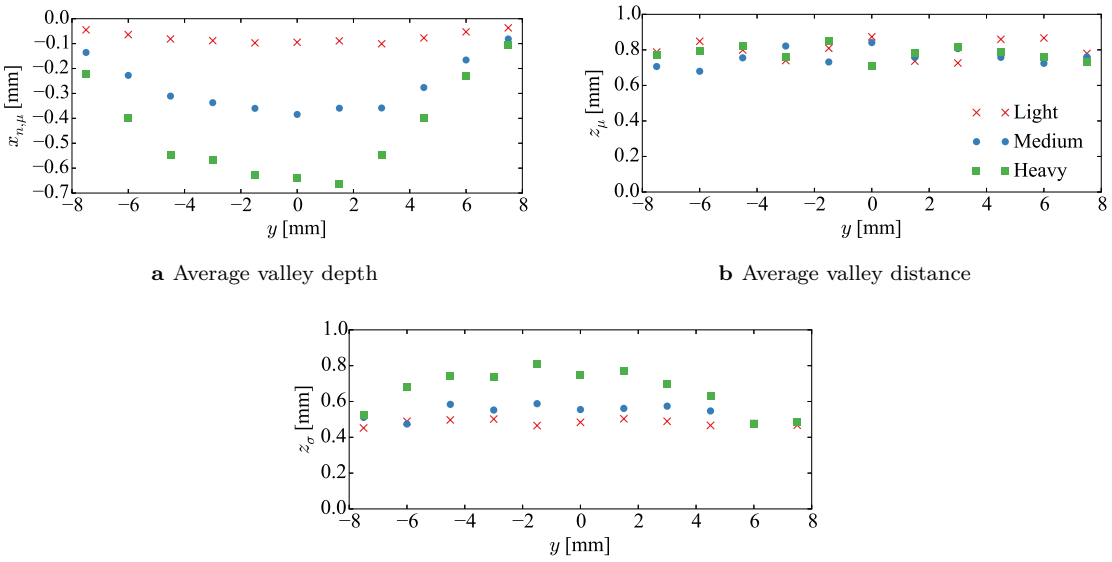

a Average valley depth

b Average valley distance

c Average of sigma Gaussian fits (width)

Figure 6.19: Valley depth, distance and width parameters along y, for light, medium and heavy DLE erosion.

Table 6.4: Average and standard deviation of valley depth, distance and width parameters, for DLE erosion obtained from surface inspection using GOM INSPECT.

	Valley depth		Valley distance		Valley width	
Level	$\mu_{x_{n,\mu}}$ [mm]	$\sigma_{x_{n,\mu}}$ [mm]	μ_{z_μ} [mm]	σ_{z_μ} [mm]	μ_{z_σ} [mm]	σ_{z_σ} [mm]
Light	-0.0898	0.0158	0.788	0.307	0.480	0.186
Medium	-0.340	0.0802	0.759	0.297	0.577	0.180
Heavy	-0.574	0.185	0.781	0.350	0.729	0.268

6.4 Aerodynamic performance results

The aerodynamic performance was established in terms of lift and drag. When adding the clean aluminium centre DLE section, pressure taps could be used to measure the lift. For all experiments lift was also measured using the load cells. Drag was measured using the wake rake. These measurements led to lift and drag polars at $Re = 3 \cdot 10^6$ and $Re = 6 \cdot 10^6$. These lift and drag polars with reduced aerodynamic performance were not applied to a BEM as for the quick erosion model, as no similar airfoils to the *DU-00-W212* are currently being used in LMWP blades.

6.4.1 Validation DLE model to AVATAR model

To validate the DLE airfoil model, a clean DLE model was applied, experiments were done at $Re = 3{\cdot}10^6$ and $Re = 6{\cdot}10^6$ and lift and drag polars were compared to the clean *DU-00-W212* AVATAR airfoil profile. Lift was measured both by pressure taps (using the aluminium centre section) and by load cells. Drag was measured using the wake rake. This validation showed if pressure taps could be used in the DLE model to measure the lift, as well as if the DLE airfoil model, due to its coupling mechanism and a filled gap between DLE and airfoil, would have an impact on aerodynamic performance.

6.4.1.1 Pressure taps

In Figure 6.20a the pressure distribution at $\alpha = 5°$ measured by the pressure taps, for both the AVATAR profile and the DLE airfoil model. This shows that for the DLE model, one pressure tap gives a pressure deviating from the *Avatar* value. This pressure tap is located at 1.5 %c on the pressure side, directly at the edge of the DLE model (near the gap between DLE model and airfoil). A possible cause for this deviation is that the tap is not sealed correctly between DLE model and airfoil, leading to a pressure drop.

This deviating pressure leads to decreased lift results, as can be seen in Figure 6.20b. Therefore there was decided to not use the pressure taps for lift measurements, and instead use the load cells. In addition, using the load cells makes it possible to add the eroded DLE centre section, instead of having a clean aluminium DLE centre section with pressure taps. This would also give more realistic results as now the DLE model is fully eroded in spanwise direction.

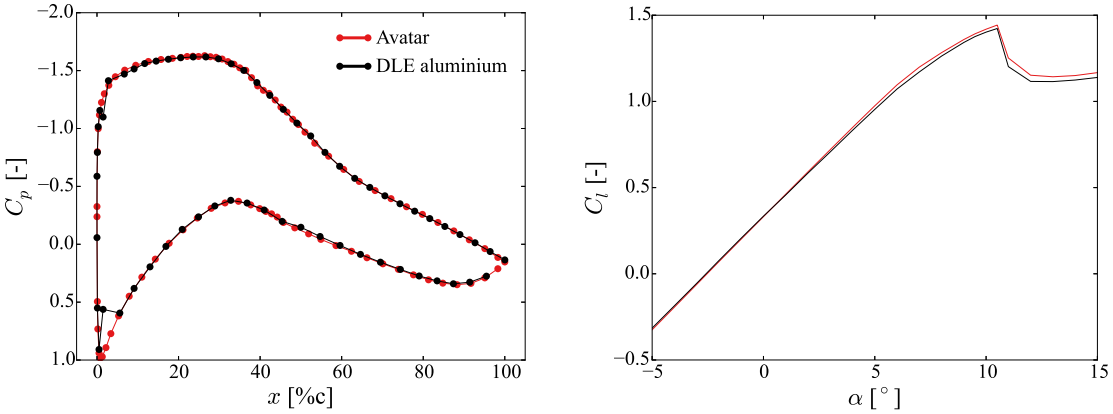

a C_p versus x **b** C_l versus α

Figure 6.20: Airfoil pressure distribution and resulting lift coefficient for clean *DU-00-W212* airfoil; comparing the pressure taps between the *Avatar* and aluminium-DLE model at $Re = 6 \cdot 10^6$.

6.4.1.2 Load cells

Lift polars measured by the load cells for the clean DLE model were compared to the *Avatar* model. As a clean DLE model both 3D printed sections were used as well as clean aluminium sections. This was done to also investigate the influence of the printing of DLE sections. In Figure 6.21a the lift polar is shown for the clean *Avatar* model, the clean aluminium DLE and the clean 3D printed DLE. This shows a decrease in lift for the 3D printed DLE above $\alpha = 5°$.

When investigating the clean 3D printed DLE model, there appeared to be steps in leading edge surface, as can be seen in Figure 6.22. These flattened steps originate from extruding the DLE cross-section in spanwise direction in BLENDER, where the cross-section taken from a CAD drawing showed flattened leading edge surface steps. This flattened surface was only present for the clean DLE model, as the Boolean operation required for the eroded models changed the clean leading edge (flattened) mesh to a correctly eroded mesh. Therefore no flattened surfaces were visible in the leading edge of the eroded models, as can be seen in Figure 6.17.

Also the flattening of the 3D printed DLE model could be compared to surface treatment during production on a real blade, where the leading edge potentially gets flattened in steps due to the grinding finishing of the coating. This flattening therefore would have a negative effect on the lift, leading to a decrease in aerodynamic performance. As this is not an erosion feature, no further investigation into the performance results of this model is included.

Finally for the lift results the clean DLE aluminium results were taken as the baseline values for aerodynamic performance, as these compare well to the clean *Avatar* model.

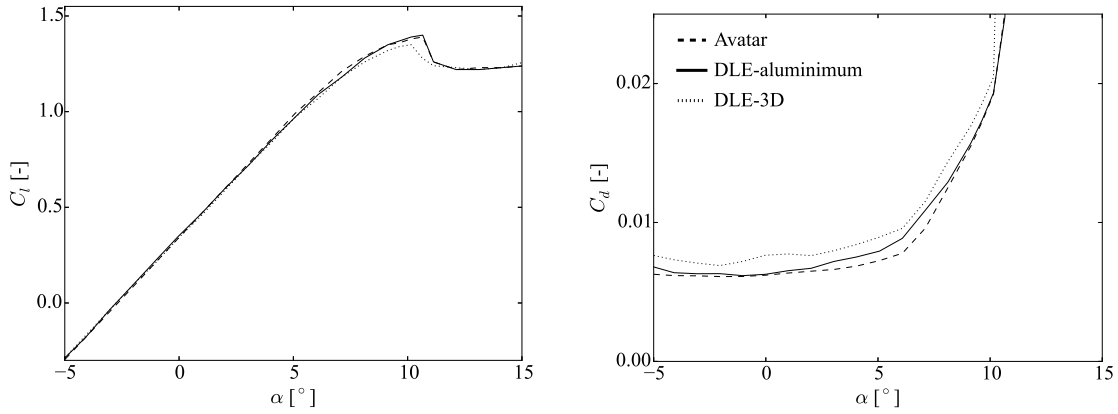

a C_l versus α **b** C_d versus α

Figure 6.21: Lift and drag polars for clean *DU-00-W212* airfoil; *Avatar* versus DLE model at $Re = 6{\cdot}10^6$.

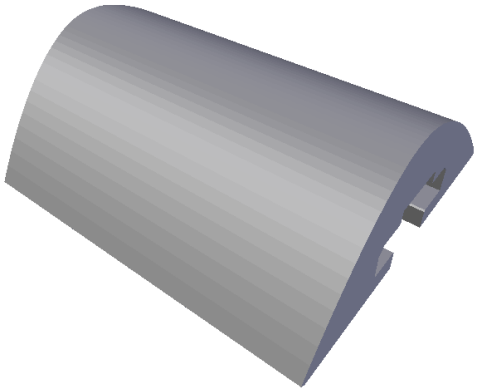

Figure 6.22: Render of clean DLE model, as constructed in BLENDER from the DLE cross-section, showing the flattened leading edge surface steps. Spanwise length is 30 mm.

6.4.1.3 Wake rake

The drag results from the wake rake of the *Avatar* model, the clean DLE aluminium and the 3D printed DLE are shown in Figure 6.21b. A slight drag increase can be seen for the DLE-aluminium model compared to the *Avatar* model between $\alpha = 3°$ and 8°. The largest drag increase occurs for the 3D printed DLE model, caused by the flattened leading edge steps. Therefore also for drag the results of the DLE-aluminium model were taken as the baseline values, where eroded DLE models were compared to.

6.4.2 Polar data

6.4.2.1 $Re = 3 \cdot 10^6$

Lift, drag and moment polars are shown for $Re = 3 \cdot 10^6$ in Figure 6.23. As baseline values, the clean aluminium DLE data were used. Also the decrease in lift, drag and lift over drag coefficient compared

to the clean values are shown in Table 6.5, at $\alpha_d = 6°$ where C_l/C_d is maximum for the clean DLE. For increasing erosion levels, the lift decreases and drag increases. For both lift and drag curves, the light erosion is still relatively close to the clean curve, whereas to medium erosion the largest jump occurs in lift decrease and drag increase.

Section 5.4.2.1 shows that the eroded lift curves for medium, heavy and heavy-delamination follow the clean curve until approximately $\alpha = 1\,°$, where for increasing angle of attack the lift curves deviate from the clean curve. At this angle of attack probably early flow transition occurs, leading to a lift reduction as seen from IR inspection and lift results for the quick erosion model in Section 5.4.2.1.

The coverage between the erosion levels is approximately constant, therefore the results for aerodynamic performance mainly show the effect of increasing erosion depth. Above the medium erosion level the lift and drag polars are fairly similar and the C_l/C_d reduction does not show any significant steps. Even for heavy-delamination with erosion depths over 3 mm the results are similar to the heavy erosion curves. From this it can be concluded that above certain erosion depths, in this case above medium erosion depth which is -0.389 mm), the detrimental impact on aerodynamic performance is relatively small. This indicates that for erosion located at the leading edge, which would perturb deeper than the coating and into the glass lay-up (-0.400 mm), only slightly decreases the aerodynamic performance. Erosion within the coating itself results in the largest detrimental effect to aerodynamic performance.

Table 6.5: Lift and drag results at $\alpha_d = 6°$ for DLE erosion ($Re = 3 \cdot 10^6$).

Phase	C_l-decrease [%]	C_d-increase [%]	C_l/C_d-decrease [%]
Clean (DLE-aluminium)	0	0	0
Light	1.98	17.4	16.5
Medium	6.93	64.7	43.5
Heavy	7.92	69.1	45.6
Heavy-delamination	8.91	71.1	46.8

6.4.2.2 $Re = 6 \cdot 10^6$

In Figure 6.24 the lift, drag and moment polars are shown for $Re = 6 \cdot 10^6$. The decrease in lift, drag and lift over drag coefficient compared to the clean values are shown in Table 6.6, at $\alpha_d = 6°$ where C_l/C_d is maximum for the clean DLE. The results show a similar trend as for $Re = 3 \cdot 10^6$, with light erosion closer to the clean tests, whereas the largest jump occurs to medium erosion with similar results for heavy and heavy-delamination erosion. This again shows that increasing the erosion from the medium level, the impact on aerodynamic performance remains constant.

For all erosion levels the aerodynamic performance loss at $Re = 6 \cdot 10^6$ is less than for $Re = 3 \cdot 10^6$, when comparing the results of Table 6.6 with Table 6.5. This difference, as was the case for the zigzag and quick model, was caused by a higher amount of energy added to the flow at higher Reynolds number, leading to a lower relative performance loss.

Table 6.6: Lift and drag results at $\alpha_d = 6°$ for DLE erosion ($Re = 6 \cdot 10^6$).

Phase	C_l-decrease [%]	C_d-increase [%]	C_l/C_d-decrease [%]
Clean (DLE-aluminium)	0	0	0
Light	0.00	15.1	13.1
Medium	4.59	46.5	34.9
Heavy	5.50	49.3	36.7
Heavy-delamination	6.42	50.3	37.7

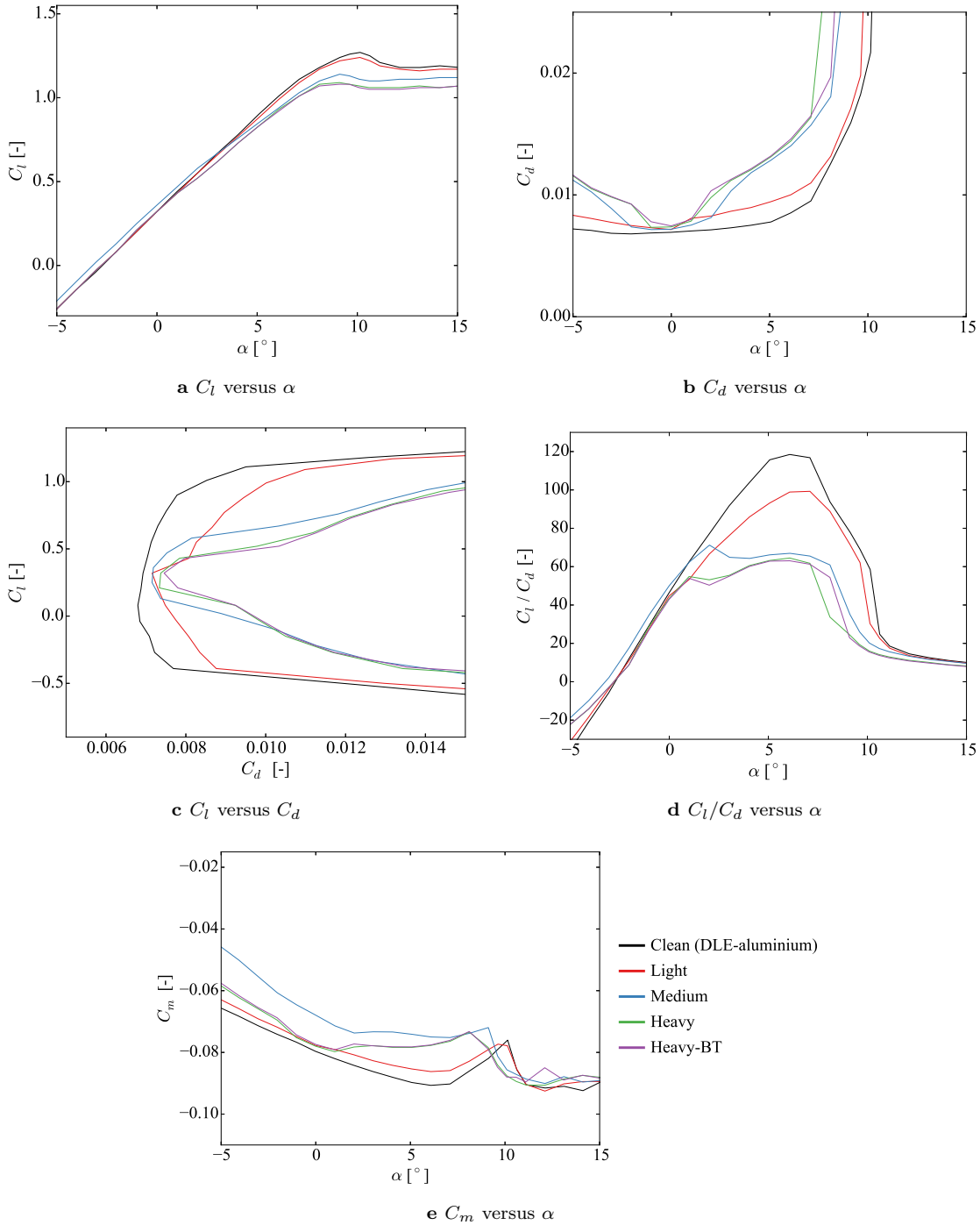

a C_l versus α

b C_d versus α

c C_l versus C_d

d C_l/C_d versus α

e C_m versus α

Figure 6.23: Aerodynamic performance for DLE model and $Re = 3 \cdot 10^6$.

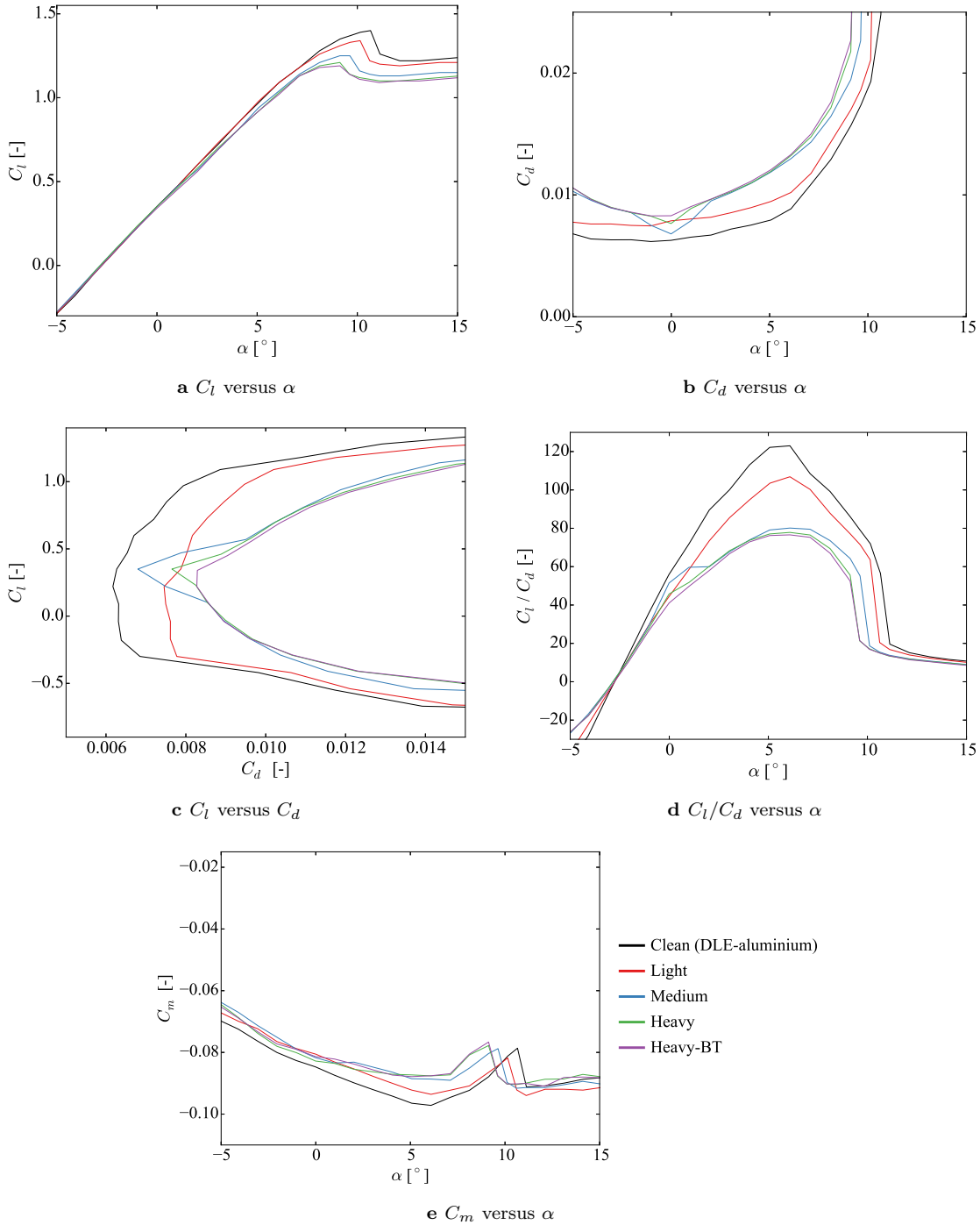

a C_l versus α

b C_d versus α

c C_l versus C_d

d C_l/C_d versus α

e C_m versus α

Figure 6.24: Aerodynamic performance for DLE model and $Re = 6 \cdot 10^6$.

CHAPTER 7

Discussion & conclusions

The first question posed in this research was how different erosion levels could be characterized by analysing specimens from the Rain Erosion Tester. Reasoning from the mass loss curve, it was assumed that in the linear part of the mass loss curve erosion perturbs only into the coating. Based on this assumption, three RET specimens were selected at different places on the mass loss curve:

- At the start of the linear curve (right after incubation)
- Further up the linear mass loss curve
- At the start of the random part of the curve (where erosion perturbs into the glass lay-up)

These specimens were analysed following a statistical analysis, where 2D roughness curves were assumed to be build up out of overlapping 2D Gaussian functions, having averages and standard deviations in depths, distances and widths. Erosion coverage followed from the impact angle of rain droplets at locations where the erosion pattern was constant or smoothed out.

The second step was to apply these characterized erosion levels to an airfoil leading edge. Three different methods were used to simulate these erosion patterns, namely:

1. The standardized roughness model using zigzag tapes
2. The quick erosion model where the surface was modified by means of hand tooling
3. The DLE model where erosion patterns were modelled and leading edges were 3D printed

A discussion of these three models, including its main features, advantages and limitations is included in Section 7.1.

These three models were tested in the LSWT, where the aerodynamic performance in terms of lift and drag was measured. Lift was measured either using pressure taps (zigzag model) or load cells (quick and DLE model), whereas drag was measured using the wake rake. In Section 7.2 the major outcomes and trends of the three models are discussed, showing similarities and differences, resulting from their different modelling methods.

Contributions to the rain erosion research are included, concluding on why this research was important. Finally recommendations for future work are stated, as this study revealed many new questions and suggestions for future research.

7.1 Discussion of models: zigzag, quick and DLE model versus RET specimens

The zigzag model, quick model and DLE model were compared to the RET specimens. For the quick and DLE model, the erosion patterns were analysed using the same method as the RET specimens were analysed, by fitting 2D Gaussian functions through the valleys, leading to the valley depth, distance and width parameters. Also coverages of the three methods were compared, as both erosion pattern and coverage affect the aerodynamic performance.

7.1.1 Zigzag model

A zigzag tape study was performed, to investigate the impact of thickness and coverage of zigzag tapes to aerodynamic performance. A key limitation of this model is that by placing tapes, material is added to the surface showing its main limit to model an erosion surface. As this method is used by the industry to validate airfoil profiles for sensitivity to roughness, it was important to compare this method to the quick and DLE erosion models.

Coverage as determined from the RET specimens does not exceed 0.5 %c. The zigzag model had a second tape applied towards suction side at approximately 0 %c, considered to be in the same range as for the RET specimens. Thicknesses of tapes used were 0.2 mm and 0.4 mm, being similar to medium and heavy RET erosion depths.

7.1.2 Quick model

The quick model simulated RET erosion patterns by hand tooling with hammering a steel brush (light erosion) or aluminium RET specimens (medium and heavy erosion) into the surface. This method removes material from the surface, being more comparable to RET erosion patterns and therefore to early erosion stages on the mass loss curve. Still the application is difficult to control and therefore the quick model is considered to be a qualitative study. Final coverage reached up to 3 &c towards pressure and suction side, which is six times further than coverage estimated from the RET specimens, being up to 0.5 %c.

After creating the pattern, the surface was 3D scanned and was analysed in same way as the RET specimens. This validation showed that for medium and heavy erosion, similar valley depth parameters were observed as for the RET specimens. At two locations the heavy erosion pattern was measured, which showed a significant difference between the depths, confirming the limitations of applying pattern by hand tooling.

7.1.3 DLE model

Erosion was modelled by creating overlapping 3D Gaussian valleys in a coordinate field, directly based upon valley depth, distance and width parameters that followed from the RET specimens. This also resulted in a material removal from the leading edge. A statistical analysis was performed on the 3D models which confirmed that the depth and width parameters matched with the RET specimens. Therefore the DLE model describes early erosion stages, whereas the light and medium model are located on the linear part of the mass loss curve.

Distance parameters between the DLE model and the RET specimens were different, which potentially resulted from using different threshold settings while finding the peaks. The models could be further optimized leading to matching parameters for distance as well. Still the distance parameter was assumed to be less critical than the depth for its impact on aerodynamic performance, as concluded in the roughness height and density study by Maniaci et al. (2016) [7].

When observing the extracted 2D roughness curves, the light DLE model lacks some sharp valleys and only models the less deep but more occurring valleys. Therefore the light DLE model resembles an erosion stage closer to incubation than the RET specimens (where additional deeper valleys were observed). This also shows a limitation of the modelling process, which filters out the extreme values.

7.1.4 Previous studies

Six previous erosion studies applied similar, but simplified methods to investigate erosion, which were compared to the zigzag model, the quick model and the DLE model. None of these methods resemble early erosion phases both in terms of shape modification and erosion coverage.

Bak et al. (2016) [15] investigated the critical leading edge roughness height for aerodynamic performance by applying bump tape of 0.1 mm or zigzag tape of 0.4 mm, at 2 %c towards suction side.

This chordwise distance is significantly further aft than for coverage determined from RET specimens or as applied to the zigzag model. As impact on aerodynamic performance increases when tapes were applied further towards suction side, the critical roughness height study did not simulate RET erosion patterns and coverage.

Gaudern (2014) [5] simulated erosion by means of self-adhesive foils, where different patterns were cut into the foil. Here pattern coverage was up to 8 %c on both suction and pressure side and therefore not resembling early erosion coverage as estimated from the RET specimens. The depths of the patterns needed to be scaled based upon roughness Reynolds number, as experiments were performed at lower Reynolds number than operating conditions. Estimations from XFOIL were required and therefore this method cannot be as accurate as testing unscaled erosion features at operating conditions. Also the cut pattern did not capture erosion features of high spatial frequency, such as the Gaussian valleys considered by the DLE model.

Sareen et al. (2013) [9] applied locations of erosion features based upon a normal distribution, similar to the valley coordinates creation as for the DLE model. In this study highest coverage was up to 10 %c on suction side, not resembling an early erosion stage. Also erosion features were hand tooled into the surface, having the same controllability limitations as the quick erosion model. Depths were estimated from photographs, resulting in an initial observed depth of 0.51 mm. This depth of 0.51 mm is similar to the phase 3 RET specimen, which would already perturb into the glass lay-up.

White et al. (2011) [6] modelled erosion by means of sand-blasting and 3D printing. Sand-blasting is considered to be difficult to control, whereas the 3D printed detachable leading edge is similar to the DLE model. Only erosion coverage reached 15 %c both to suction and pressure side, which is the highest erosion coverage applied compared to the other erosion studies. The 3D printed model computed heights in coordinates based upon a 3D cosine function. This resulted in a pattern with continuous non-overlapping peaks and valleys up to 1.2 mm. The peaks resulted in a positive shape deformation (outwards of the surface), which is different than observed for the RET specimens and more accurately modelled by 3D Gaussian valley patterns of the DLE model.

Langel et al (2015) [8] and Maniaci et al. (2016) [7] simulated erosion by applying randomly distributed circles as vinyl stickers to the leading edge, with coverage till 2%c on suction side. Vinyl sticker heights were 0.10 mm, 0.14 mm and 0.20 mm, which can be compared to depths in between stage 1 and 2 erosion of the RET specimens (presumably in the linear part of the mass loss curve).

7.2 Discussion of performance: quick and DLE model versus zigzag model

The zigzag, quick and DLE models led to different results in aerodynamic performance. It is essential to compare the quick and DLE results to the zigzag model, as zigzag tapes are being used to validate airfoil performance in case of an eroded surface. Aerodynamic performance was measured at $Re = 3 \cdot 10^6$ and $Re = 6 \cdot 10^6$, which are similar to operating conditions in the outer regions of a wind turbine blade. Testing at high Reynolds numbers resulted that no Reynolds scaling for depths was required for the quick and DLE model, in contrast to previous erosion studies.

A comparison of performance losses of the zigzag, quick and erosion model to previous erosion studies is not included, due to different testing conditions at lower Reynolds number for previous erosion studies, as well as significant difference in erosion coverages applied. The quick and DLE model resemble early erosion stages with relatively low coverage, whereas previous erosion studies were focused on larger coverage as discussed in Section 7.1.

7.2.1 Zigzag model

The zigzag model revealed different trends that were also observed in the results of the quick and the DLE model. First of all, applying a tape at the stagnation point did not result in a performance loss; lift and drag polars were similar to the clean case. Applying tapes towards suction side gave the highest

impact on the positive lift, decreasing the aerodynamic performance. This in contract to placing tapes towards pressure side, where no impact on positive lift was observed. From this it could be assumed that erosion would have highest impact at the leading edge, when its coverage is shifted towards suction side.

In general no gradual performance loss could be established using the zigzag tapes. Only at $Re = 6 \cdot 10^6$ when zigzag tape of 0.2 mm was applied at the stagnation point and towards the suction side, a performance loss of 7 % was measured at the design angle of attack. All other performance losses measured were higher than 30 %. Also as soon as two tapes were applied towards suction side, increasing the thickness of the tape did not further increase the performance loss. This shows the limits of using zigzag tapes for roughness validation, where applying a single tape towards suction side gives abrupt performance losses. For early erosion stages, more gradual performance losses were expected, as the erosion progression on itself is a gradual process.

The zigzag tape study showed that at a higher Reynolds number, the performance loss initiates at a lower angle of attack. At a higher Reynolds number, the boundary layer thickness decreases, whereas the roughness height (of the tape) remains the same. Therefore the tape perturbs deeper into the boundary layer, causing flow transition at a lower angle of attack (as compared to testing at lower Reynolds number). In addition, it could be concluded that at the design angle of attack, as soon as the flow was fully disturbed (the cases where two zigzag tapes were placed towards suction side), the relative performance loss was lower for higher Reynolds number. This is most likely caused by the fact that at higher Reynolds number more energy is added to the flow, whereas the absolute performance loss due to the tapes remains similar between the two tested Reynolds numbers. Therefore the relative performance loss will be lower at higher Reynolds number.

7.2.2 Quick model

The quick model showed some similarities to the zigzag model, though in general a more gradual performance loss was observed. From the zigzag tape study was concluded that erosion towards pressure side would have a marginal impact, therefore the quick model only had an erosion progressing towards suction side.

At $Re = 3 \cdot 10^6$, applying erosion in the stagnation point (furthest down to pressure side), did not result in an impact on performance loss. The largest performance impact occurred when erosion was applied as second distance from the stagnation point, both for light and medium erosion. Heavy erosion did not result in an additional performance loss when the same coverage was applied. Only when the coverage further increased towards suction side, performance loss increased. Therefore it seemed that from the medium erosion level, the higher severity of the erosion has no additional impact. Increasing the coverage still increases the performance loss. This was also observed for the zigzag tapes, where having two tapes towards suction side decreased the performance. Increasing the thickness of the tapes had no additional effect.

At higher Reynolds number the early transition due to the eroded surface shifted to a lower angle of attack, which was clearly visible from the IR analysis. This again was likely caused by lower boundary layer thickness at higher Reynolds number. This shift in early transition to lower angle of attack, led to more abrupt performance losses, at the design angle of attack, already occurring for light erosion. From light erosion applied up to the second distance from the stagnation point, where increased severity of erosion had no additional impact. Maximum performance loss was already reached due to the light erosion. Increasing the coverage still increased the performance loss.

Final maximum performance losses at design angle of attack were similar to the zigzag tape model, with a maximum performance loss of approximately 60 % at $Re = 3 \cdot 10^6$ and approximately 50 % at $Re = 6 \cdot 10^6$. At these maximum performance losses, the severity of erosion has less influence than the coverage. Therefore this similarity could be caused by having a similar coverage up to suction side, where $y \approx 1$ %c band for the zigzag model and $y = 0.5$ %c for the quick erosion. Light erosion up to first or second distance (depending on the Reynolds number) led to a similar performance loss of having a tape at the stagnation point plus one tape towards suction side, which was a loss of approximately

30 %. As for the zigzag model, at the design angle of attack the higher Reynolds number resulted in a lower relative performance loss, in case of the heavy eroded patterns.

With the use of a BEM calculation, it was shown how this method could be applied to see the impact of erosion is to AEP. This was done by applying the quick model erosion polars to the tip region of the blade, going from light to medium to heavy erosion polars while going from inboard to tip sections of the blade. This resulted in an AEP loss of 1 & at an average wind speed of 7.5 m/s, showing that an significant power loss can be expected from erosion perturbing into the coating and only just reaching the glass lay-up.

7.2.3 DLE model

DLE erosion was expected to have a worse impact on aerodynamic performance than the first stages of light quick erosion. The reason for that was that DLE erosion coverage was shifted more towards the suction side (at the leading edge) compared to the location for early quick erosion, which is located more towards pressure side. At $Re = 3 \cdot 10^6$ for light DLE erosion, performance loss was approximately 17 %, whereas light quick erosion led to either 7 % or 30 % loss, depending on first (L2) or second location (L3) from stagnation point. DLE light erosion led to a performance loss in between the two values for quick erosion, mainly caused by coverage difference. The same was observed for DLE medium erosion, having a performance loss approximately between quick erosion M2 and M. This showed that the quick eroded medium level gave an aerodynamic performance loss similar to medium quick erosion, with differences mainly caused by coverage. It is important to note that two different airfoil profiles were used, where each airfoil has a different roughness sensitivity. This also played a role in the differences in performance loss.

The aerodynamic losses are lower for the heavy DLE model than for the heavy quick or zigzag model. This is expected to be caused by a combination of difference in coverage and usage of a different airfoil profile. Also, the modelled pattern of the DLE model is more smooth than the quick hand tooled surface, lacking sharp edges as each valley was modelled as a Gaussian function.

Furthermore, from medium DLE erosion, performance loss at the design angle of attack does not increase when going to heavy or heavy-delamination erosion. Coverage of light, medium and heavy DLE erosion was the same. Therefore the DLE model confirmed that from a certain erosion level, the severity of erosion has no additional impact on the performance loss, as flow already transitions directly at the leading edge (where the erosion is located). Only increasing the coverage will decrease the performance. This also proves that erosion perturbing deeper than the coating does not decrease aerodynamic performance to a higher extent than erosion just reaching the glass lay-up. Erosion within the coating itself would have the largest detrimental effect to aerodynamic performance. This also appears to be the same for quick erosion, where from medium 3 erosion the aerodynamic performance loss remains constant.

It was proven from analysing the valley depths that heavy and delamination erosion were on the right points on the mass loss curve. At the random part of mass loss curve the erosion perturbs into the glass lay-up. At that stage the flow will be disturbed to a level that the performance loss is maximum, as flow will transition directly at the leading edge. The heavy-delamination will be on the random curve as valleys up to 3 mm were reached, significantly deeper than the 0.4 mm coating thickness considered. Now polars at the five points (clean, light, medium, heavy and delamination) on the mass loss curve are available.

In the future, a study with the Rain Erosion Tester will be performed to find turbine operating times (depending on climate) corresponding to the different modelled erosion levels. An erosion polar is available after incubation at the start of the linear mass loss curve, at the end of the linear mass loss curve and inside the random mass loss curve. Inside the linear curve, between light and medium erosion, polars can potentially be interpolated leading to a full timespan of performance loss while erosion progresses inside the coating. The start of the random mass loss curve, at heavy erosion, shows the maximum performance loss which would still be of a concern to the AEP loss. Further delamination

of the leading edge requires a blade to be repaired for maintaining the structural performance (instead of aerodynamic performance).

A BEM calculation could not be performed to compute the AEP as no similar airfoil profile was used on an LMWP blade. The aerodynamic loss for heavy DLE erosion is less than for heavy quick erosion. This would result in an AEP loss that is lower than for the quick BEM. As stated before, this difference in performance loss is probably caused by a difference in coverage.

7.3 Final conclusions

Most importantly this study provided a method to characterize and model different erosion patterns, based upon realistic erosion patterns created by the Rain Erosion Tester. Modelling realistic erosion patterns required that material should be removed from the surface, whereas in previous erosion studies material was added to the surface. In addition these studies simulated erosion based upon inaccurate visual observations such as pictures, which cannot capture important erosion features such as depth in a systematic and scientific way, especially not for early erosion phases. In this study, RET specimens were available which resembled these early erosion phases. 3D scanning of the specimens provided surface maps of the erosion patterns where following an accurate statistical analysis important roughness parameters such as valley depth, distance and width were computed.

Ultimately, airfoil polars were established for the different characterized erosion patterns by testing the specimens in the wind tunnel. It was shown that these polars later can be used in BEM computations to find the power curves, to directly see what influence of erosion to the power loss is. As a result, a method is available to test for different erosion levels. This method proved to be more accurate than applying zigzag tapes. This because zigzag tapes have a violent effect to the flow, representing sudden stepwise disturbances while early erosion phases affect the flow more continuous.

For now, the actual modelling of the erosion patterns is more valuable than the final aerodynamic performance results. This study has proven that erosion can be analysed based upon RET specimens, following a scientific statistical approach, and subsequently can be experimentally tested in the LSWT. Further improvements of the modelled erosion surface are definitely possible, both with respect to the erosion features itself (such as Gaussian valleys) as for the erosion coverage applied. However, this study has proven that it is possible to analyse realistic RET erosion specimens, model an erosion pattern based upon the RET specimens and perform a validation between them.

7.4 Recommendations

The now available detachable leading edge model has opened up an infinite amount of possibilities to investigate the impact of erosion to aerodynamic performance, both to experimental and numerical studies. Therefore, this study is considered to be just a beginning of modelling rain erosion and applying this to numerical methods.

First of all, further investigations should be done on using of zigzag tapes for validation of airfoils to erosion surfaces. In this study the thinnest tape used was 0.2 mm, resulting to a violent impact on performance as compared to the quick and DLE erosion methods. Thinner tapes of 0.1 mm should have been included in the study such as by Bak et al. (2016) [15]. Besides using zigzag tapes, also flat tapes, trip strips or roughness tapes such as used by Standish et al. (2010) [4] could be investigated. An unlimited amount of possibilities is possible regarding using different tapes and coverages, where some configuration could result in similar performance losses as for modelled erosion.

It is assumed that the RET specimens show an erosion patterns which is similar to erosion patterns as seen on blades on operating turbines. In this project no analysis of how well RET erosion compares to real erosion is included. To confirm that the RET method results in realistic erosion patterns, it would be valuable to obtain 3D scans of early erosion stages as seen on real blades. The same statistical analysis on the real erosion patterns could be performed as on the RET specimens. These 3D scans could

be obtained by investigating blades which are taken down from a turbine for any other maintenance tasks.

In the DLE model, some erosion features such as sharp valley edges were not included. These sharp edges appeared to occur in the quick erosion surface. To investigate different impacts to the performance between the modelled and quick erosion patterns, the DLE sections could be created in the same material as the quick model. Applying the same erosion coverage as for the current DLE section for light, medium erosion, the quick and modelled pattern could be compared one to one on the same airfoil profile. This would eliminate the sensitivity to roughness difference between the quick and DLE airfoil profile, as now only the DLE airfoil profile would be used. The cost of quick material DLE sections would be relatively cheap, compared to the 3D printed DLE sections.

The current DLE models were mostly focused on reaching the erosion valley depths as seen for the RET specimens. Different analyses should also be performed to research what the influence is of valley width and distance. 3D printing of DLE sections enables to investigate each and every erosion feature.

It is possible to fold created coordinates to a leading edge. It would be interesting to see if the RET specimen scans (STL files) would be transferred to XYZ coordinates and folded directly to the leading edge. This would imply some coverage copying of the pattern, ensuring that coverage is the same as for the modelled DLE sections. By testing in the LSWT it could investigated what the difference to performance would be between modelled surfaces and direct RET erosion surfaces.

For the DLE model, coverage applied was the same for the different erosion levels, based upon an estimation of impact angles as seen on the RET specimens. As coverage is highly important to the performance loss, an additional study should investigate how well coverage of the RET specimens compares to early erosion on real blade.

Another potential study which would be more expensive but also interesting would be to build a detachable leading edge airfoil mode for the *LM18%* profile, with a larger sized DLE section to apply further coverage. This way, the impact of erosion coverage on aerodynamic performance could be further analysed. Also modelled erosion patterns in 3D printed DLE sections with same erosion coverage as for the quick eroded model could provide a one to one comparison of the quick hand tooled pattern versus the modelled pattern. This would require a new airfoil and larger 3D DLE prints, being a costly study.

Besides experimental studies, numerical analysis is also recommended. Now an experimental method is available to validate different erosion or roughness CFD methods. A 3D CFD simulation might be possible by including the erosion pattern coordinates to the leading edge. This would require significant computational costs. Both coordinates of the scan of the RET erosion pattern and the modelled pattern could be incorporated. This could be used to investigate differences in performance between the modelled pattern and a direct scan.

In the future, realistic times of different erosion phases will be available, depending on different rain climates. Combining a point in time with an erosion pattern, and therefore with a performance loss, together with a BEM model, will lead to power loss estimations as a direct function of time. These kind of methods have great potential in the wind power industry, where both suppliers (such as LMWP) and end customers (utility companies) are eager to find the optimal time to apply maintenance in a cost effective way.

APPENDIX A

Quick erosion statistical parameters

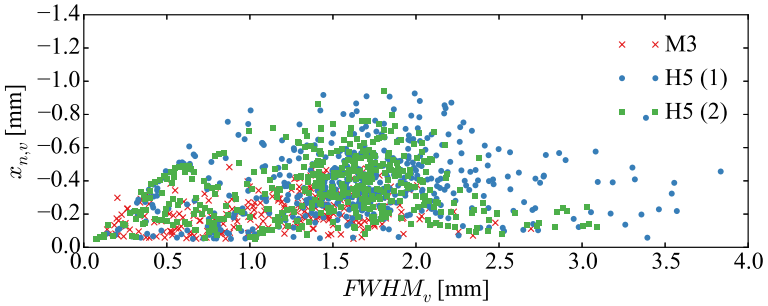

Figure A.1: Point cloud of all valleys with associated depths and widths for quick erosion M3 and H5.

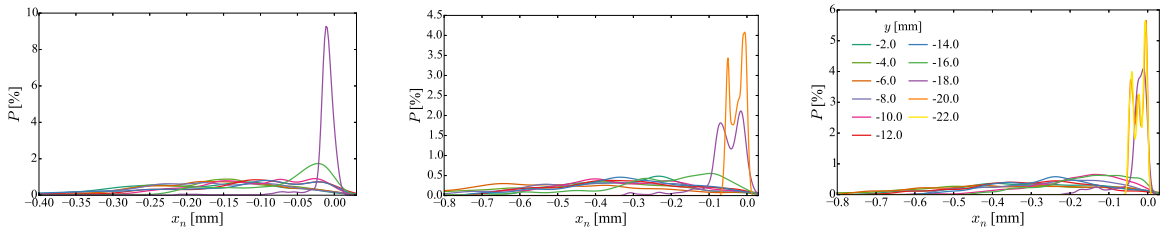

a Medium 3 **b** Heavy 5 (1) **c** Heavy 5 (2)

Figure A.2: Kernel density estimations for quick erosion, between $y = -2\,\text{mm}$ and $y = -20\,\text{mm}$.

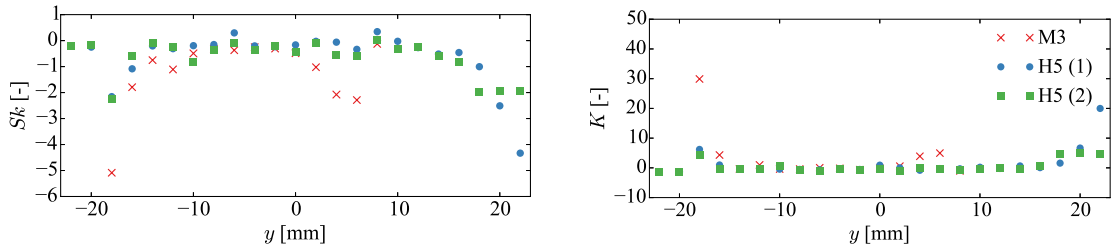

a Skewness **b** Kurtosis

Figure A.3: Surface height distribution parameters for quick erosion M3 and H5.

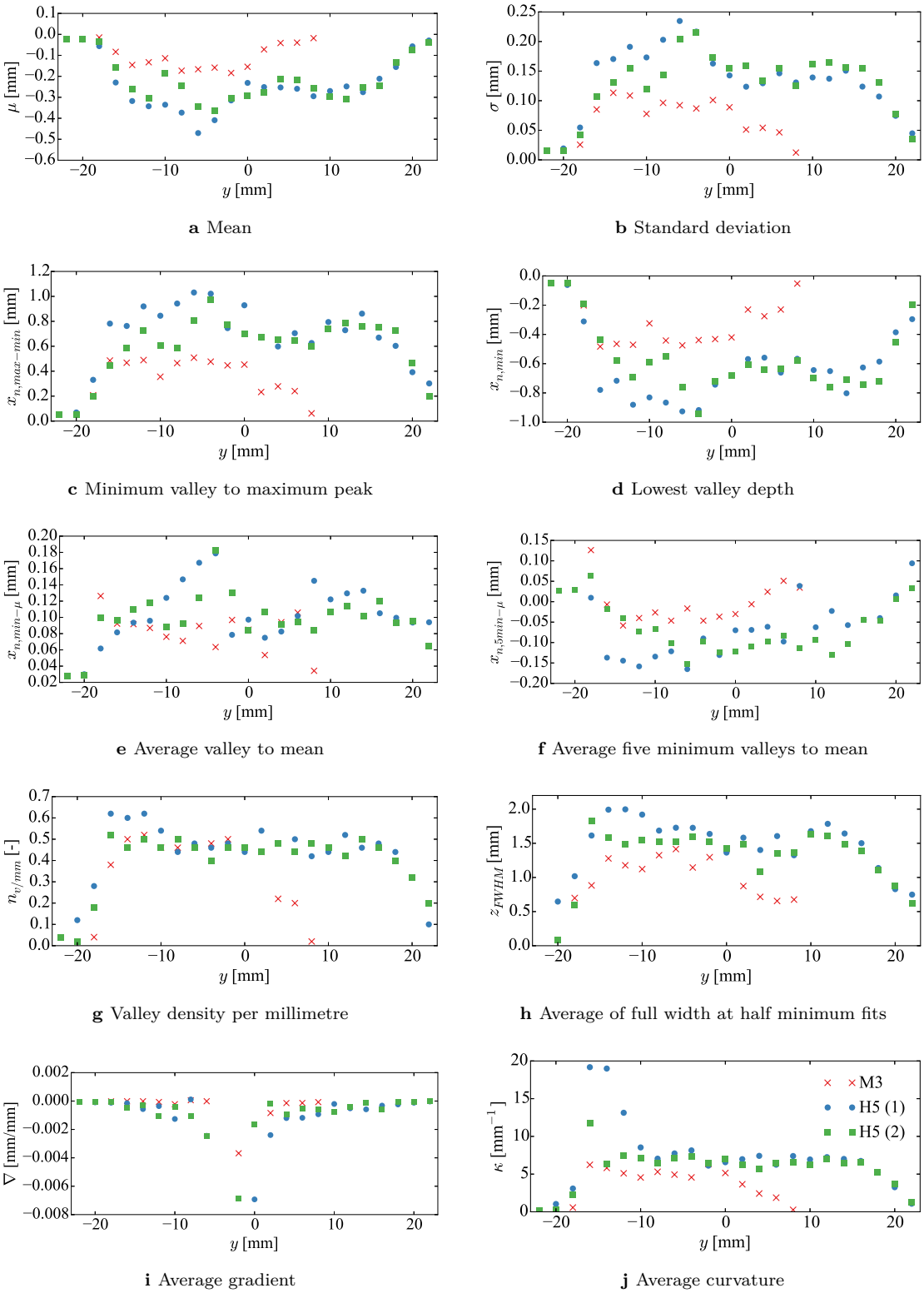

a Mean

b Standard deviation

c Minimum valley to maximum peak

d Lowest valley depth

e Average valley to mean

f Average five minimum valleys to mean

g Valley density per millimetre

h Average of full width at half minimum fits

i Average gradient

j Average curvature

Figure A.4: Average roughness, spatial and Gaussian parameters for quick erosion M3 and H5.

APPENDIX B

DLE coupling test

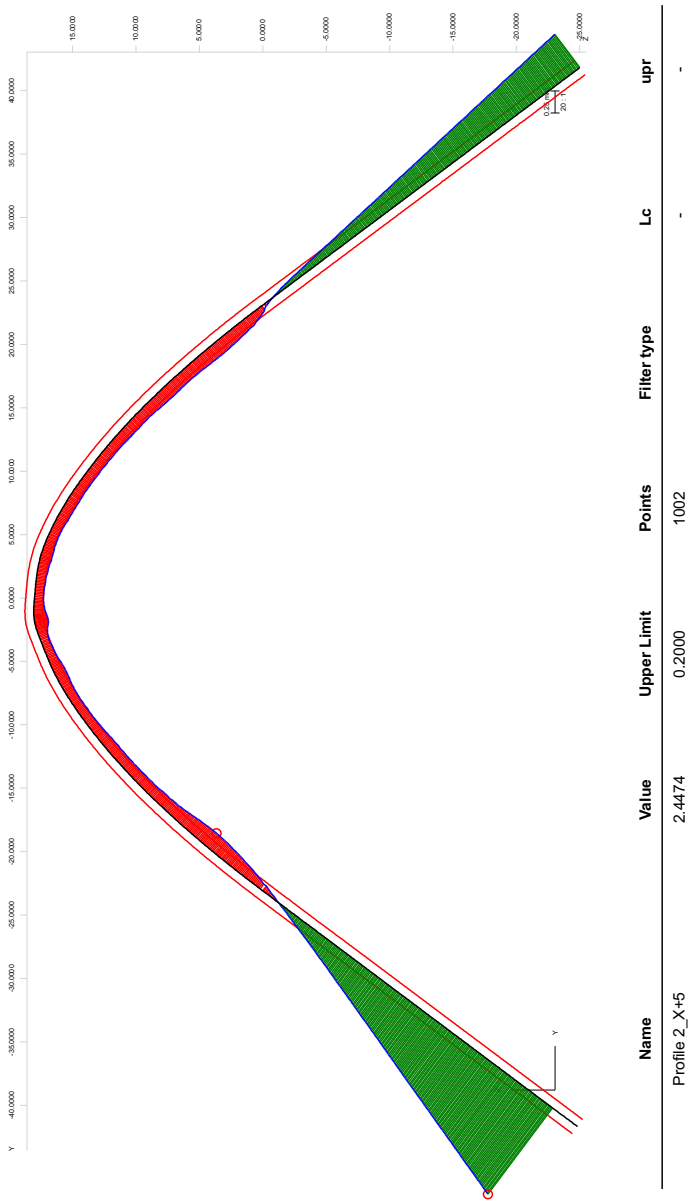

Figure B.1: Profilometer scan of initial DLE coupling test. At the gap between DLE and coupling model no substantial deviation is visible.

APPENDIX C

DLE erosion statistical parameters

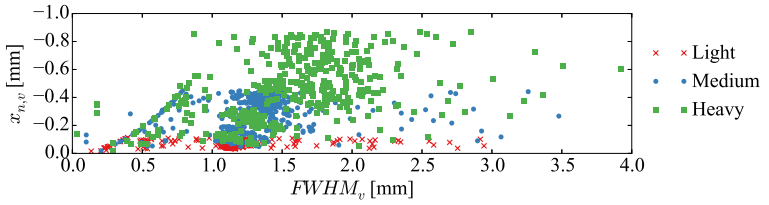

Figure C.1: Point cloud of all valleys with associated depths and widths for DLE erosion light, medium and heavy.

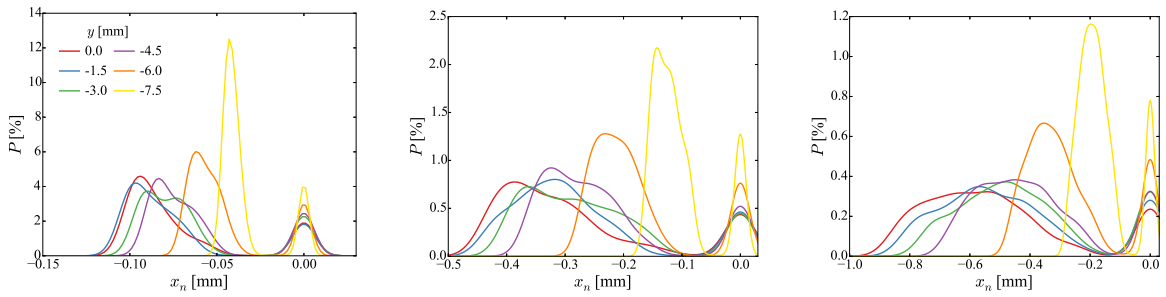

a Light **b** Medium **c** Heavy

Figure C.2: Kernel density estimations for DLE erosion, between $y = 0\,\text{mm}$ and $y = -7.5\,\text{mm}$.

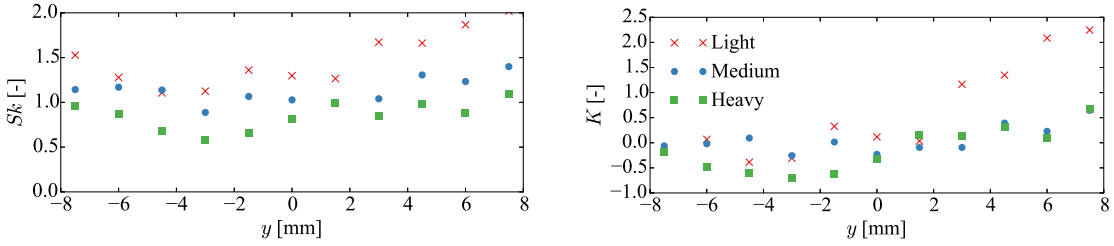

a Skewness **b** Kurtosis

Figure C.3: Surface height distribution parameters for DLE erosion light, medium and heavy.

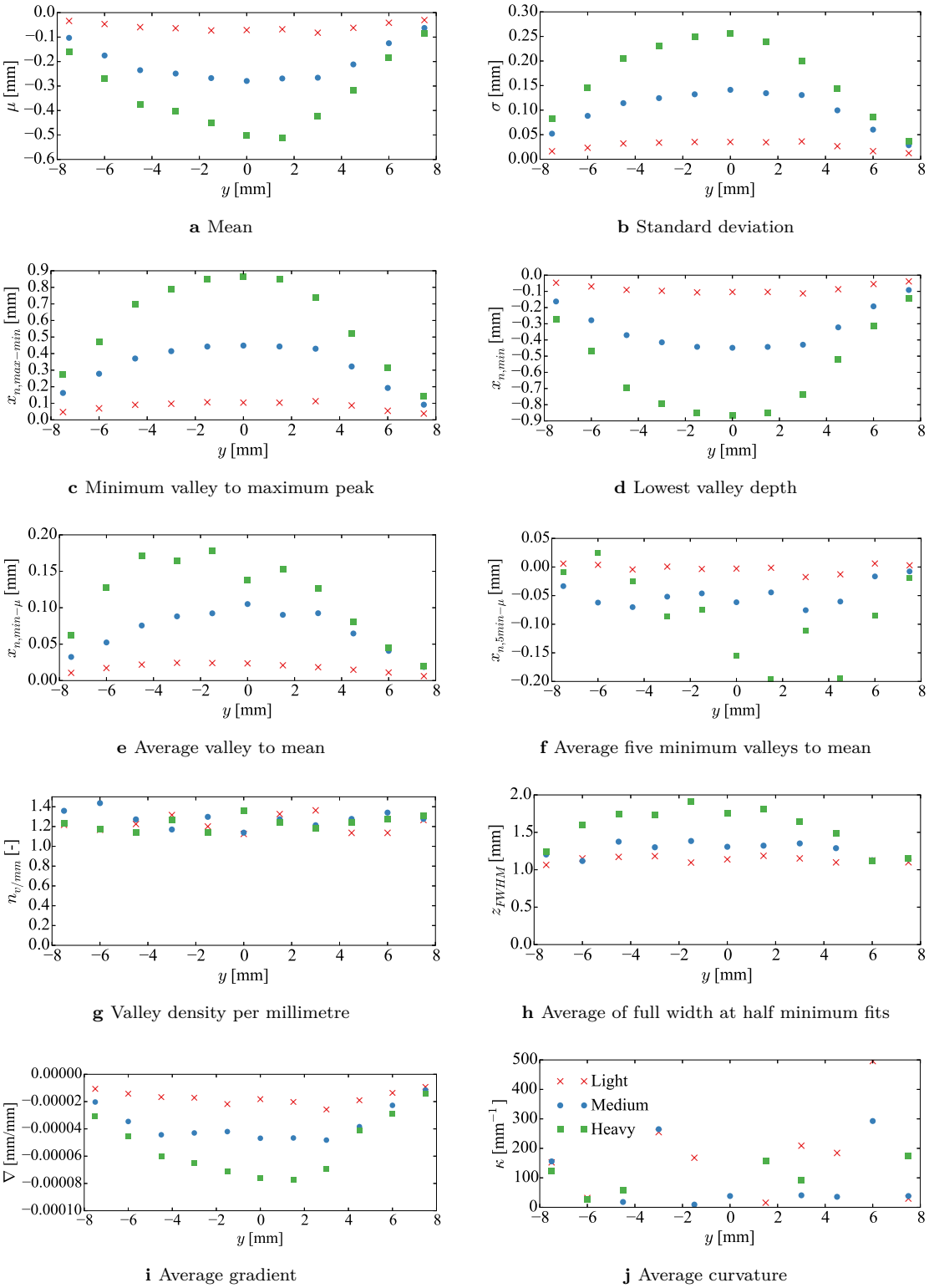

a Mean

b Standard deviation

c Minimum valley to maximum peak

d Lowest valley depth

e Average valley to mean

f Average five minimum valleys to mean

g Valley density per millimetre

h Average of full width at half minimum fits

i Average gradient

j Average curvature

Figure C.4: Average roughness, spatial and Gaussian parameters for DLE erosion light, medium and heavy.

Bibliography

[1] M.H. Keegan, D.H. Nash, and M.M. Stack. "On Erosion Issues Associated With the Leading Edge of Wind Turbine Blades". In: *Journal of Physics D: Applied Physics* 46.38 (2013), page 383001. DOI: 10.1088/0022-3727/46/38/383001.

[2] P. Fuglsang, C. Bak, M. Gaunaa, and I. Antoniou. "Design and Verification of the Risø-B1 Airfoil Family for Wind Turbines". In: *Journal of Solar Energy Engineering* 126.4 (2004), page 1002. DOI: 10.1115/1.1766024.

[3] R.J.O.M. van Rooij and W.A. Timmer. "Roughness Sensitivity Considerations for Thick Rotor Blade Airfoils". In: *Journal of Solar Energy Engineering* 125.4 (2003), page 468. DOI: 10.1115/1.1624614.

[4] K. Standish, P. Rimmington, J. Laursen, H. Paulsen, and D. Nielsen. "Computational Predictions of Airfoil Roughness Sensitivity". In: *48th AIAA Aerospace Sciences Meeting Including the New Horizons Forum and Aerospace Exposition*. American Institute of Aeronautics and Astronautics (AIAA), 2010. DOI: 10.2514/6.2010-460.

[5] N. Gaudern. "A Practical Study of the Aerodynamic Impact of Wind Turbine Blade Leading Edge Erosion". In: *Journal of Physics: Conference Series* 524 (2014), page 012031. DOI: 10.1088/1742-6596/524/1/012031.

[6] E.B. White, D. Kutz, J. Freels, J.P. Hidore, R. Grife, Y. Sun, and D. Chao. "Leading-edge Roughness Effects on 63_3-418 Airfoil Performance". In: *49th AIAA Aerospace Sciences Meeting including the New Horizons Forum and Aerospace Exposition*. American Institute of Aeronautics and Astronautics (AIAA), 2011. DOI: 10.2514/6.2011-352.

[7] D.C. Maniaci, E.B. White, B. Wilcox, C.M. Langel, C.P. van Dam, and J.A. Paquette. "Experimental Measurement and CFD Model Development of Thick Wind Turbine Airfoils With Leading Edge Erosion". In: *Journal of Physics: Conference Series* 753 (2016), page 022013. DOI: 10.1088/1742-6596/753/2/022013.

[8] C.M. Langel, R. Chow, O.F. Hurley, C.P. van Dam, R.S. Ehrmann, E.B. White, and D. Maniaci. "Analysis of the Impact of Leading Edge Surface Degradation on Wind Turbine Performance". In: *33rd Wind Energy Symposium*. American Institute of Aeronautics and Astronautics (AIAA), 2015. DOI: 10.2514/6.2015-0489.

[9] A. Sareen, C.A. Sapre, and M.S. Selig. "Effects of Leading Edge Erosion on Wind Turbine Blade Performance". In: *Wind Energy* 17.10 (2013), pages 1531–1542. DOI: 10.1002/we.1649.

[10] R.S. Ehrmann, E.B. White, D.C. Maniaci, R. Chow, C.M. Langel, and C.P. Van Dam. "Realistic Leading-edge Roughness Effects on Airfoil Performance". In: *31st AIAA Applied Aerodynamics Conference*. American Institute of Aeronautics and Astronautics (AIAA), 2013. DOI: 10.2514/6.2013-2800.

[11] F.R. Menter, T. Esch, and S. Kubacki. "Transition Modeling Based on Local Variables". In: *5th International Symposium on Turbulence Modeling and Measurements* (2002), pages 555–564. DOI: 10.1016/b978-008044114-6/50053-3.

[12] R.B. Langtry and F.R. Menter. "Correlation-based Transition Modeling for Unstructured Parallelized Computational Fluid Dynamics Codes". In: *AIAA Journal* 47.12 (2009), pages 2894–2906. DOI: 10.2514/1.42362.

[13] A.F.P. Ribeiro, D. Casalino, and E. Fares. "Direct Numerical Simulation of an Airfoil With Wand Grain Roughness on the Leading Edge". In: *NASA/TM-2016-219363* (2016).

[14] O. Ceyhan. "Towards 20MW Wind Turbine: High Reynolds Number Effects on Rotor Design". In: *50th AIAA Aerospace Sciences Meeting including the New Horizons Forum and Aerospace Exposition* (2012). DOI: 10.2514/6.2012-1157.

[15] C. Bak, M. Gaunaa, A. S. Olsen, and E. K. Kruse. "What Is the Critical Height of Leading Edge Roughness for Aerodynamics?" In: *Journal of Physics: Conference Series* 753 (September 2016), page 022023. DOI: 10.1088/1742-6596/753/2/022023.

[16] P. Fuglsang, I. Antoniou, N. Sørensen, and H. Aagaard Madsen. "Validation of a Wind Tunnel Testing Facility for Blade Surface Pressure Measurements". In: *Annual report* 981(EN) (1998).

[17] William Gracey, William Letko, and Walter R. Russell. *Wind-Tunnel Investigation of a Number of Total-Pressure Tubes at High Angles of Attack Subsonic Speeds*. Technical report. National Advisory Committee For Aeronautics, 1951.

[18] T.T. Bui, D.L. Oates, and J.C. Gonsalez. "Design and Evaluation of a New Boundary-layer Rake for Flight Testing". In: *38th Aerospace Sciences Meeting and Exhibit* (2000). DOI: 10.2514/6.2000-503.

[19] D.W.C. Baker, K. H. Jolliffe, and D. Pearson. "The Resistance of Materials to Impact Erosion Damage". In: *Philosophical Transactions of the Royal Society of London. Series A, Mathematical and Physical Sciences* 260.1110 (1966), pages 193–203.

[20] G.S. Springer, C.I. Yang, and P.S. Larsen. "Analysis of Rain Erosion of Coated Materials". In: *Journal of Composite Materials* 8.3 (1974), pages 229–252. DOI: 10.1177/002199837400800302.

[21] B. Bhushan. "Modern Tribology Handbook". In: CRC Press LCC, 2001. Chapter 2. Surface Roughness Analysis and Measurement Techniques. ISBN: 978-0-8493-7787-7. DOI: 10.1201/9780849377877.

[22] G. Fiore, G.E.C. Camarinha Fujiwara, and M.S. Selig. "A Damage Assessment for Wind Turbine Blades From Heavy Atmospheric Particles". In: *53rd AIAA Aerospace Sciences Meeting*. American Institute of Aeronautics and Astronautics (AIAA), 2015. DOI: 10.2514/6.2015-1495.

[23] M. Kazhdan and H. Hoppe. "Screened Poisson Surface Reconstruction". In: *ACM Transactions on Graphics (TOG)* 32.29 (2013), page 13. DOI: 10.1145/2487228.2487237.

Nomenclature

α	Airfoil angle of attack [°]
α_d	Design angle of attack [°]
β	Inflow angle defining coverage constant area [°]
$\boldsymbol{t}$	Unit vector aligned with the chord [m]
Δ	Average gradient 2D roughness curves [m/m]
γ	Inflow angle defining coverage smoothed area [°]
κ	Average curvature 2D roughness curves [m^{-1}]
μ	Mean height 2D roughness curves [m]
μ_d	Dynamic viscosity [Pa]
μ_Y	Average of 3D Gaussian in Y-direction [m]
μ_Z	Average of 3D Gaussian in Z-direction [m]
$\mu_{x_{n,\mu}}$	Average of valley depth for constant area [m]
μ_{z_μ}	Average of valley distance for constant area [m]
μ_{z_σ}	Average of valley width for constant area [m]
ρ	Density of air [kg/m^3]
ρ_R	Density of rain droplet (water) [kg/m^3]
$\rho_{Z,Y}$	Correlation between Z and Y coordinates [−]
σ	Standard deviation 2D roughness curves [m]
σ^2	Variance 2D roughness curves [m]
σ_Y	Standard deviation 3D Gaussian in Y-direction [m]
σ_Z	Standard deviation 3D Gaussian in Z-direction [m]
σ_v	Standard deviation of fit in individual valley [m]
$\sigma_{x_{n,\mu}}$	Standard deviation of valley depth for constant area [m]
σ_{z_μ}	Standard deviation of valley distance for constant area [m]
σ_{z_σ}	Standard deviation of valley width for constant area [m]
τ_ω	Wall shear stress [Pa]
θ_R	Impact angle of rain droplet to airfoil surface [°]

φ_{af}	Airfoil normal to surface direction [°]
φ_c	Clean DLE normal to surface direction [°]
ζ	Angle of zigzag tape [°]
a_G	Height parameter Gaussian function [m]
A_n	Area loss per millimetre 2D roughness curves [$^{\mathrm{mm}^2}/_{\mathrm{mm}}$]
b	Spanwise length [m]
b_G	Position parameter Gaussian function [m]
c	Chordwise length [m]
C_d	Section drag coefficient [−]
c_G	Standard deviation parameter Gaussian function [m]
C_l	Section lift coefficient [−]
C_n	Normal force coefficient [−]
C_p	Section pressure coefficient [−]
d_R	Diameter of rain droplet [m]
F	Impact force [N]
$FWHM_v$	Full width at half maximum of fit in individual valley [m]
K	Kurtosis 2D roughness curves [−]
k	Roughness height [m]
L	Sampling length 2D roughness curves [m]
L	Total lift force [N]
L_{zz}	Distance between peaks of zigzag tape [m]
m_R	Mass of rain droplet [kg]
$n_{v/mm}$	Valley density per millimetre 2D roughness curves [−]
p_∞	Freestream static pressure [Pa]
p_i	Local pressure tap static pressure [Pa]
$p_{t,w}$	Local wake rake tube total pressure [Pa]
p_w	Wake rake static pressure [Pa]
q	Dynamic pressure [Pa]
q_∞	Freestream dynamic pressure [Pa]
q_w	Local wake rake tube dynamic pressure [Pa]
Re_k	Roughness Reynolds number [−]
s	Location pressure tap in (x, y) [m]

Sk	Skewness 2D roughness curves [−]
U	Local velocity [m/s]
U_R	Impact velocity of rain droplet [m/s]
W	Width of zigzag tape [m]
X	Eroded DLE coordinates in x-direction [m]
x	Streamwise coordinate [m]
x_n	Normal to leading edge surface distance [m]
x_t	Streamwise coordinate of flow transition
$x_{n,5min-\mu}$	Average five deepest valleys to mean height 2D roughness curves [m]
$x_{n,\mu}$	Average valley depth 2D roughness curves [m]
$x_{n,max-min}$	Distance highest peak and lowest valley 2D roughness curves [m]
$x_{n,min-\mu}$	Average valley to mean height 2D roughness curves [m]
$x_{n,min}$	Lowest valley depth 2D roughness curves [m]
$x_{n,v}$	Normal to LE surface height of individual valley [m]
$x_{s.p.}$	Streamwise coordinate stagnation point [m]
x_t	Transition point location along the chord [%c]
x_{x_n}	x-component of erosion normal to surface depth [m]
x_{af}	Airfoil coordinates in x-direction [m]
X_c	Clean DLE coordinates in x-direction [m]
Y	Eroded DLE coordinates in y-direction [m]
y	Direction normal to chord and span [m]
y_s	Leading edge surface distance [m]
$y_{s,af}$	Airfoil surface length [m]
$y_{s,c}$	Clean DLE surface length [m]
$y_{s,p}$	Eroded pattern surface length [m]
y_{x_n}	y-component of erosion normal to surface depth [m]
y_{af}	Airfoil coordinates in y-direction [m]
Y_c	Clean DLE coordinates in y-direction [m]
Z	Eroded DLE coordinates in z-direction [m]
z_μ	Average valley distance 2D roughness curves [m]
z_v	Location of individual valley [m]
BEM	Blade element momentum

BLR	Boundary layer rake
CFD	Computational fluid dynamics
DLE	Detachable leading edge
DNS	Direct numerical simulation
DTU	Danmarks Tekniske Universitet
IR	Infrared
LMWP	LM Wind Power
LSWT	Low speed wind tunnel
PC	Personal computer
PDF	Probability density function
PS	Pressure side on airfoil profile
SP	Stagnation point on airfoil profile
SPL	Stanford polygon file
SS	Suction side on airfoil profile
STL	Stereolithography